


June 2022

Molecular Vibrations and Shape-Selectivity: A Computational Model of Biofuel Precursors in Zeolites

Babgen Manookian
University of Massachusetts Amherst

Follow this and additional works at: https://scholarworks.umass.edu/dissertations_2

 Part of the [Computational Chemistry Commons](#), [Materials Chemistry Commons](#), and the [Physical Chemistry Commons](#)

Recommended Citation

Manookian, Babgen, "Molecular Vibrations and Shape-Selectivity: A Computational Model of Biofuel Precursors in Zeolites" (2022). *Doctoral Dissertations*. 2551.
<https://doi.org/10.7275/28563594> https://scholarworks.umass.edu/dissertations_2/2551

This Open Access Dissertation is brought to you for free and open access by the Dissertations and Theses at ScholarWorks@UMass Amherst. It has been accepted for inclusion in Doctoral Dissertations by an authorized administrator of ScholarWorks@UMass Amherst. For more information, please contact scholarworks@library.umass.edu.

**MOLECULAR VIBRATIONS AND SHAPE-SELECTIVITY: A
COMPUTATIONAL MODEL OF BIOFUEL PRECURSORS IN ZEOLITES**

A Dissertation Presented

by

BABGEN MANOOKIAN

Submitted to the Graduate School of the
University of Massachusetts Amherst in partial fulfillment
of the requirements for the degree of

DOCTOR OF PHILOSOPHY

May 2022

Department of Chemistry

© Copyright by Babgen Manookian 2022

All Rights Reserved

**MOLECULAR VIBRATIONS AND SHAPE-SELECTIVITY: A
COMPUTATIONAL MODEL OF BIOFUEL PRECURSORS IN ZEOLITES**

A Dissertation Presented

by

BABGEN MANOOKIAN

Approved as to style and content by:

Scott M. Auerbach, Chair

Bret Jackson, Member

Kevin Kittilstved, Member

Friederike C. Jentoft, Member

Ricardo Metz, Department Head
Department of Chemistry

*“Do not go where the path may lead, go instead where there is no path and
leave a trail”*

Ralph Waldo Emerson

ACKNOWLEDGMENTS

I would like to thank Scott Auerbach for being an incredible Ph.D. advisor and mentor during my time at University of Massachusetts Amherst. Scott always had confidence in my abilities as a young researcher. He pushed me to be well-rounded scientist and to ask thoughtful and enticing chemistry questions. The time we have spent together will have a long-lasting, positive impact on my life, and I am forever grateful for it.

I would also like to thank my committee members Dr. Bret Jackson, Dr. Kevin Kittilstved, and Dr. Friederike Jentoft for their support and guidance. My learning experience in graduate school had many ups and downs, and I very much appreciated the insight provided from my committee members throughout those times.

I am also extremely grateful to those who mentored me during my time as an undergraduate at San Diego State University; the guidance I received then was essential for my success in graduate school. Dr. Andrew Cooksy and Dr. Thomas Cole helped me begin my research endeavors as my first mentors; their contribution to my learning experience was invaluable. I would also like to acknowledge Thelma Chavez and the MARC program for the support and guidance I received as a MARC scholar.

I would like to express my heartfelt gratitude and admiration for all those who collaborated with me over the last six years. Firstly, Dr. Eric Hernandez and Dr. Friederike Jentoft worked closely with me and Scott to understand complex scientific problems in zeolite science. They significantly contributed to my growth as a zeolite researcher through their deep understanding of the field. Also, I am very thankful for

having had the opportunity to work closely with Dr. Christopher Mundy and Marcel Baer from Pacific Northwest National Laboratory in the early years of my doctoral work.

I would like to thank the friends I have made during my time at UMass. I am truly lucky to have had such great, encouraging people to help me get through graduate school, research, and life.

Finally, I would like to express my unconditional gratitude for my family. Even though we were many miles apart, their love, support and guidance ensured I was never alone while I embarked on this challenging journey.

ABSTRACT

MOLECULAR VIBRATIONS AND SHAPE-SELECTIVITY: A COMPUTATIONAL MODEL OF BIOFUEL PRECURSORS IN ZEOLITES

MAY 2022

BABGEN MANOOKIAN

B.S., SAN DIEGO STATE UNIVERSITY

Ph.D., UNIVERSITY OF MASSACHUSETTS AMHERST

Directed by: Professor Scott M. Auerbach

We have used Density Functional Theory (DFT) to model acyclic and cyclic olefins in acidic zeolites. We have studied the impact of host-guest interactions between adsorbed molecules and zeolite frameworks through the lens of molecular vibrations and shape-selectivity. This work considered three zeolite frameworks with varying pore structures and environments: large pore zeolite HMOR and medium pore zeolites HZSM-5 and HZSM-22. A key finding is that for acyclic olefins in acidic zeolites there exists two regimes of host-guest interaction: a strong interaction leading to protonation and a weak interaction between charged guest and zeolite framework. We found that these interactions manifest in the IR spectra such that protonation leads to significant changes in band position for allylic vibrations, $\nu_{\text{am}}(\text{C}=\text{C}-\text{C}^+)$, and in contrast these band positions are left substantially unchanged due to the weaker Coulombic interaction. These results indicate that to model acyclic olefins in acidic zeolites one only need to consider the protonated state in the gas phase.

We worked in close collaboration with zeolite experimentalists E. Hernandez and F. Jentoft at the University of Massachusetts Amherst Chemical Engineering department to investigate the presence of shape-selectivity during the formation of

alkylcyclopentenyl cations from acyclic precursors in acidic zeolites. We incorporated DFT models and configurational sampling to establish band positions associated with allylic stretching $\nu_{\text{as}}(\text{C}=\text{C}-\text{C}^+)$ in cyclopentenyl cations. We found that the band position of this stretch was sensitive to the substitution pattern on the allylic system of the ring, such that a methyl substitution instead of a hydrogen at the center carbon (C-2) resulted in a $\sim 20 \text{ cm}^{-1}$ red-shift in the IR band. Our collaborative efforts also found that the formation of these alkylcyclopentenyl cations in zeolites is shape-selective; the C-2 methyl-substituted alkylcyclopentenyl cation forms in larger pore HMOR whereas in medium pore zeolites, HZSM-5 and HZSM-22, the C-2 hydrogen-substituted alkylcyclopentenyl appears to be the main product. We performed DFT-based thermodynamics calculations and found that the relative stability of the methyl-substituted alkylcyclopentenyl cation remained unchanged in all three zeolites. This suggests that the formation of these alkylcyclopentenyl cations is not under thermodynamic control.

We used DFT calculations to build a microkinetic model of the isomerization of alkylcyclopentenyl cations in HZSM-5 and HZSM-22 zeolites, using both finite-temperature dynamics and zero-Kelvin path methods to compute barriers. We found that the isomerization leading to experimentally relevant alkylcyclopentenyl cations with C-2 methyl (T-type) or hydrogen (K-type) substitutions occurs through a multi-pathway reaction network. We found that the pathways were similar in the two zeolites, but the populations at equilibrium differed such that one T-type product formed in HZSM-5 and two formed in HZSM-22 with evidence of kinetic control of product formation.

TABLE OF CONTENTS

	Page
AKNOWLEDGMENTS	v
ABSTRACT	vii
LIST OF TABLES	xii
LIST OF FIGURES	xiii
CHAPTER	
1. INTRODUCTION	1
1.2 References	13
2. EXPERIMENTAL AND DFT CALCULATED IR SPECTRA OF GUESTS IN ZEOLITES: ACYCLIC OLEFINS AND HOST-GUEST INTERACTIONS	16
2.1 Introduction	16
2.2 Methods	18
2.2.1 Experimental Methods	18
2.2.2 Computational Methods	18
2.2.2.1 Modeling the Zeolite	18
2.2.2.2 Electronic Structure Calculations	19
2.2.2.3 Dynamics	20
2.2.2.4 Conformational Analyses	22
2.3 Results and Discussion	23
2.3.1 Adsorption of of 2,4-Dimethyl-1,3-pentadiene on a Non- acidic Framework: Contributions of Rotational Conformers to IR Spectrum.	23
2.3.2 Adsorption of Neutral Acyclic Olefins on Acidic HMOR Zeolite: Strong Interactions Lead to Protonation	32
2.3.3 Adsorbed Protonated Olefins on HMOR: Nature of Electrostatic Interactions	36
2.4 Conclusions	39
2.5 Appendix – Supporting Information	41
2.5.1 Inclusion of zeolite framework for normal mode analysis	41
2.5.2 Thermodynamics of periodic DFT systems	42
2.5.3 Free energy profiles for rotational conformers of olefin I	42
2.5.4 Thermodynamics of protonation for olefins I and II	44
2.5.5 Conformational analysis for olefin II ⁺	45

2.5.6 Impact of thermal fluctuations through ensemble average technique	46
2.5.7 Intramolecular distances and angles between gas-phase and zeolite-adsorbed II^+	46
2.6 References	47
3. INVESTIGATING THE EXTENT OF SHAPE-SELECTIVITY IN MEDIUM AND LARGE PORE ZEOLITES DURING ALKYL CYCLOPENTENYL CATION FORMATION	50
3.1 Introduction	50
3.2 Methods	52
3.2.1 Experimental Methods	52
3.2.2 Computational Methods	53
3.2.2.1 Zeolite Models	53
3.2.2.2 Electronic Structure Calculations	54
3.2.2.3 Computed Infrared Spectra and Thermodynamics	54
3.3 Results	56
3.3.1 Cyclization of 2,6-Dimethyl-2,4,6-octatriene on H-Zeolites	56
3.3.2 Experimental data and findings	57
3.3.3 Results from Theory	62
3.3.3.1 DFT Computed IR Spectra of Alkenyl, Alkadienyl, and Alkylcyclopentenyl Cations.	62
3.3.3.2 DFT and MP2 Investigation of the Thermodynamics of Alkylcyclopentenyl-Zeolite Systems.	65
3.4 Conclusions	69
3.5 References	70
4. SHAPE-SELECTIVITY OF CYCLOPENTENYL CATION ISOMERIZATION: INVESTIGATING THE EXTENT OF KINETIC CONTROL	74
4.1 Introduction	74
4.2 Methods	79
4.2.1 Rule Input Network Generator Protocol	79
4.2.2 Modeling the Zeolite	81
4.2.3 Electronic Structure Calculations	81
4.2.4 Free Energy Calculations	82
4.2.5 Kinetic Model	84
4.3 Results	85
4.3.1 Alkyl-substituted cyclopentenyl cation isomerization reaction network	85
4.3.2 Eight-step reaction pathway with a T-type isomer as a product and a K-type isomer as an intermediate.	87

4.3.3 Alkyl-substituted cyclopentenyl cation isomerization reaction network in H-ZSM-5 and H-ZSM-22.....	90
4.4 Conclusions.....	94
4.5 References.....	96
5. CONCLUSIONS AND FUTURE WORK.....	99
5.1 Summaries of Conclusions	99
5.1.1 Molecular vibrations of acyclic olefins in zeolites and the magnitude of host-guest interactions	99
5.1.2 Shape-selectivity in medium pore zeolites during formation of cyclopentenyl cations	100
5.1.3 Extent of kinetic control of the isomerization of alkyl- substituted cyclopentenyl cations in H-ZSM-5 and H-ZSM- 22.....	102
5.2 Suggestions for Future Work	103
BIBLIOGRAPHY.....	109

LIST OF TABLES

Table	Page
Table 2.1 Summary of vibrational band assignments for gauche s-cis and s-trans conformers of molecule I. Frequency values from the DRIFT spectrum over deAl-BEA are shown. Each band is associated with either the gauche s-cis or s-trans conformer as determined by comparison with computed frequencies, as highlighted by the light blue boxes. Shaded boxes highlight conformer assignments.....	32
Table 2.2 Summary of computed frequencies (cm^{-1}) for protonated olefins I+ and II+ in the gas phase and inside HMOR zeolite. Experimental DRIFTS frequencies are shown for comparison for the olefins adsorbed on HMOR	39
Table 2.3 Computed free energy profiles for rotation between gauche s-cis and s-trans conformers of I. Higher accuracy model chemistries show similar trend of lower energy gauche s-cis conformer.	43
Table 2.4 Various protonation sites for molecules I and II along with corresponding Gibbs Free Energies at 293K. Energies reported relative to lowest energy site.	44
Table 2.5 Computed free energies for the 8 conformers of protonated olefin II+. Energies are shown relative to the low energy all trans conformer (TTTT).	45
Table 3.1 Summary of Computed Frequencies of Allylic Stretching Vibrations of Gas-Phase and Zeolite-Sorbed Alkenyl Cations. (Reproduced with permission from Hernandez, E. D.; Manookian, B.; Auerbach, S. M.; Jentoft, F. C. Shape-Selective Synthesis of Alkylcyclopentenyl Cations in Zeolites and Spectroscopic Distinction of Constitutional Isomers. <i>ACS Catal.</i> 2021, <i>11</i> (21), 12893–12914. Copyright 2021 American Chemical Society.)	64
Table 3.2 Computed free energies for cyclopentenyl cations in respective zeolites. (Reproduced with permission from Hernandez, E. D.; Manookian, B.; Auerbach, S. M.; Jentoft, F. C. Shape-Selective Synthesis of Alkylcyclopentenyl Cations in Zeolites and Spectroscopic Distinction of Constitutional Isomers. <i>ACS Catal.</i> 2021, <i>11</i> (21), 12893–12914. Copyright 2021 American Chemical Society.)	68
Table 4.1 Helmholtz energies of alkyl-substituted cyclopentenyl isomers relative to the reactant isomer where the isomerization reaction network begins. All energies reported in kcal/mol.	76

LIST OF FIGURES

Figure	Page
Figure 1.1 Schematic representation of coke formation in zeolites. The theoretical coke molecules are shown in the grey circle and are shown to clog the pores limiting diffusivity and rendering the catalyst inactive. Figure adapted from Ref. ¹	2
Figure 1.2 Summary of the reactions studied in this work and current understanding of the mechanisms by which they occur. Protonation of acyclic olefins (top) occurs readily in zeolites through interaction with Brønsted acid sites. Cyclization of acyclic cations to alkylcyclopentenyl cations (middle) reported in homogeneous acid media. ¹⁰ Isomerization of alkylcyclopentenyl cations (bottom) leads to more stable constitutional isomers. ^{11,12} This dissertation studies these reactions in the context of molecular vibrations and shape-selectivity.....	4
Figure 1.3 Range of zeolite pore sizes and comparison with molecular diameters of hydrocarbons. In this work we report results on MFI and MOR zeolites labeled above. Figure reproduced from Ref. ¹³	5
Figure 1.4 Host-Guest interaction in medium pore zeolite, H-ZSM-22. Confinement in the zeolite pore leads to shape-selectivity of products in the formation of alkylcyclopentenyl cations.....	6
Figure 1.5 Representative H-ZSM-5 unit cell used in periodic calculations via CP2K. Each unit cell consists of a single Al atom substitution corresponding to the active site of the catalyst.	9
Figure 2.1 Acyclic olefins and the respective conjugate bases used in this study.....	17
Figure 2.2 Illustration of the HMOR supercell used for periodic DFT calculations. Along the c-direction, an extra unit cell was included to create the 1×1×2 supercell that limits interaction of guest molecules in neighboring periodic images. The HMOR unit cell is highlighted by the dashed box.....	19
Figure 2.3 Highest occupied molecular orbitals (HOMOs) of rotational conformers for olefin I computed in the gas-phase, where the red/blue denotes the phase (sign) of the HOMO. Extended region of conjugated electron density involving neighboring methyl group, shown in blue, lowers energy for (a) gauche s-cis conformer relative to (b) s-trans conformer.	25
Figure 2.4 (a) Parity plot comparing experimental frequencies from DRIFTS of molecule I in deAl-BEA with DFT-computed frequencies of I over all-silica MOR. The parity line (x=y) is shown to highlight the different discrepancies in high- (blue) and low-frequency (red) regions of the IR spectrum. (b) Bar graph showing signs and	

magnitudes of discrepancies between computed and experimental frequencies (the latter shown on the left of Fig. 4b) along with their assignments.....	27
Figure 2.5 Comparison of computed and experimental spectra of molecule I. DRIFT spectrum (purple) was taken at 20 °C over DeAl-BEA. Computed spectra for molecules I in all-silica MOR (top) and in gas phase (middle). In each environment, the spectrum associated with s-trans (blue), gauche s-cis (red), and the Boltzmann sum (black) are shown. Wavenumber values apply to Boltzmann sum. Side panels focus on (left) high-frequency (C-H stretch) and (right) low-frequency (C=C stretch) regions.....	28
Figure 2.6 DRIFT spectra at 20 °C (black) for guest molecules (a) I and (b) II in HMOR zeolite. Shown for comparison are zeolite-adsorbed, computed spectra using full optimization of neutral (orange) and protonated (blue) forms of each molecule.	33
Figure 2.7 Illustration of I ⁺ adsorbed over HMOR zeolite. Fully optimized geometry is shown with equilibrium bond distances [Å]. White arrow designates the vibrational motion associated with the 1543 cm ⁻¹ peak in the computed spectrum.....	36
Figure 2.8 Comparison of computed gas-phase (red) and zeolite-adsorbed (blue) spectra for molecules (a) I ⁺ and (b) II ⁺	38
Figure 2.9 Systematic inclusion of zeolite framework atoms for normal mode analysis calculation and spectra generation (molecule II ⁺). No change seen in spectra in 1300-1700 cm ⁻¹ region even when all zeolite atoms are included in the calculation.	42
Figure 2.10 Helmholtz energy profile for rotation of olefin I between gauche s-cis and s-trans states. Energies computed using model described in Section 2.5.2. Molecules pictured are fully geometry optimized structures. Dihedral angles are reported in red.	43
Figure 2.11 Possible protonation sites shown for molecules I and II. All possible sites were protonated manually and a Gibbs free energy was calculated to determine the lowest energy site.....	44
Figure 2.12 Comparison of spectra obtained using ensemble averaging technique at 20, 130, and 200 °C to full optimization model (0 Kelvin). Experimental DRIFT spectrum at 20 °C is also shown for comparison. All spectra are for protonated octatriene in HMOR.....	46
Figure 2.13 Stick spectra of 30 images extracted from AIMD at 20 °C (left) and 200 °C(right).	46
Figure 2.14 Comparison of relevant intramolecular bond distances and dihedrals for II ⁺ in the gas phase (top) and over HMOR (bottom). The bond distances of the allylic system	

are nearly identical in the two environments while the dihedrals exhibit subtle deviations of up to 10°.	47
Figure 3.1 General structures of alkylcyclopentenyl cation isomers with ring numbering system as indicated. (Reproduced with permission from Hernandez, E. D.; Manookian, B.; Auerbach, S. M.; Jentoft, F. C. Shape-Selective Synthesis of Alkylcyclopentenyl Cations in Zeolites and Spectroscopic Distinction of Constitutional Isomers. <i>ACS Catal.</i> 2021, <i>11</i> (21), 12893–12914. Copyright 2021 American Chemical Society.)	52
Figure 3.2 Cyclization of 2,6-dimethyl-2,4,6-octatriene to ethyltrimethylcyclopentenyl cation isomers in the presence of a Brønsted Acid. Numbers identify carbon atoms according to IUPAC nomenclature and change after cyclization. The ring is closed at the C-2 and C-6 carbons of the acyclic cation, which become the C-5 and C-4 carbons, respectively, of the cyclic cation. (Reproduced with permission from Hernandez, E. D.; Manookian, B.; Auerbach, S. M.; Jentoft, F. C. Shape-Selective Synthesis of Alkylcyclopentenyl Cations in Zeolites and Spectroscopic Distinction of Constitutional Isomers. <i>ACS Catal.</i> 2021, <i>11</i> (21), 12893–12914. Copyright 2021 American Chemical Society.)	57
Figure 3.3 Difference DRIFT spectra during the in situ TPreact of 2,6-dimethyl-2,4,6-octatriene on (A) H-MOR (zeolite diluted to 20 wt.% in KBr) and (B) H-ZSM-5 (zeolite diluted to 33 wt.% in KBr) at (a) 20 °C, (b) 120 °C, (c) 200 °C, and (d) after cooling the zeolite back to 20 °C. Spectra are offset for clarity. (Reproduced with permission from Hernandez, E. D.; Manookian, B.; Auerbach, S. M.; Jentoft, F. C. Shape-Selective Synthesis of Alkylcyclopentenyl Cations in Zeolites and Spectroscopic Distinction of Constitutional Isomers. <i>ACS Catal.</i> 2021, <i>11</i> (21), 12893–12914. Copyright 2021 American Chemical Society.)	59
Figure 3.4 Difference DRIFT spectra during the in situ TPreact of 2,6-dimethyl-2,4,6-octatriene on H-ZSM-22 (zeolite diluted to 33 wt.% in KBr) at (a) 20 °C, (b) 150 °C, (c) 250 °C, and (d) 300 °C. Spectra between 1300 and 1800 cm ⁻¹ are offset for clarity. Inset: Magnification of the region of spectrum measured at 250 °C between 2600 and 3300 cm ⁻¹ . (Reproduced with permission from Hernandez, E. D.; Manookian, B.; Auerbach, S. M.; Jentoft, F. C. Shape-Selective Synthesis of Alkylcyclopentenyl Cations in Zeolites and Spectroscopic Distinction of Constitutional Isomers. <i>ACS Catal.</i> 2021, <i>11</i> (21), 12893–12914. Copyright 2021 American Chemical Society.)	60
Figure 3.5 Structures of enylic carbenium ions investigated using DFT and MP2 methods. (Reproduced with permission from Hernandez, E. D.; Manookian, B.; Auerbach, S. M.; Jentoft, F. C. Shape-Selective Synthesis of Alkylcyclopentenyl Cations in Zeolites and Spectroscopic Distinction of Constitutional Isomers. <i>ACS Catal.</i> 2021, <i>11</i> (21), 12893–12914. Copyright 2021 American Chemical Society.)	62

Figure 3.6 Computed IR spectra via Gaussian 09 of (A) acyclic monoenyl cations III and IV, (B) methyl-substituted cyclopentenyl cations Ia and IIa, and (C) and ethyltrimethylcyclopentenyl cations Ib and IIb in the gas phase. Spectra are computed using BLYP/6-311G(d); frequencies are fit to Lorentzian functions and scaled by 0.998.....	63
Figure 3.7 Comparison of computed Gibbs energies (at 200 °C) of ethyltrimethylcyclopentenyl cation isomers computed using varying DFT functionals (PBE, BLYP, B3LYP) and MP2.....	66
Figure 4.1 Scheme outlining the protocol used in the Rule Input Network Generator (RING) code. Input for the code included the reactant A, rules corresponding to methyl, ethyl, and hydride shifts, and constraints limiting high energy intermediates. The output was an isomerization reaction network made up of 15 pathways constituting 27 elementary reactions and resulting in two types of alkyl-substituted cyclopentenyl cations labeled T and K-type isomers.	80
Figure 4.2 Cyclopentenyl cation isomerization reaction network obtained from RING. The network is made up of 15 pathways and 24 unique isomers. The reaction includes two K-type isomers, K1 and K2, and three T-type isomers, T1, T2, and T3.	86
Figure 4.3 An example of an elementary step obtained from RING. An ethyl transfer which breaks the resonance and forms a local carbocation. In general, reactions in which resonance is broken are endothermic, whereas those which resonance is reestablished are exothermic.....	87
Figure 4.4 Transition state region geometry extracted from metadynamics simulation. The geometry was used to obtain initial input for CINEB calculations. Note: the structure pictured here is not geometry optimized.....	89
Figure 4.5 Helmholtz free energy surface for one of the 15 pathways obtained from RING in H-ZSM-5 at 200 °C. Pathway begins at reactant isomer A and terminates at the T2 isomer with K1 as an intermediate. The local minima are shown using solid bars while transition states are shown using dashed bars. Errors associated with averaging scheme outlined in the text are also shown. All energies are reported in kcal/mol.....	90
Figure 4.6 Concentration plots for T and K-type isomers obtained by constructing microkinetic model for cyclopentenyl isomerization in (a) H-ZSM-5 and (b) H-ZSM-22.....	91
Figure 4.7 Isomerization reaction network with highlighted branch point during the back reaction from T3 to T2. The forward E9 reaction, shown in red, was determined to be rate-limiting in H-ZSM-22. Also reported is the activation free energy for the reaction in H-ZSM-22 of 16.9 kcal/mol.	93

- Figure 5.1 Comparison of keto/enol tautomerization reaction mechanisms over acidic zeolite active site. The top shows the mechanism obtained using a zero-Kelvin approach which yields a concerted process. In the bottom panel the mechanism from finite temperature sampling is shown which is a stepwise process and includes an intermediate.....104
- Figure 5.2 Proposed reaction of dihedral configurational changes preceding cyclization and isomerization. The octatriene molecule on the left is in a trans/trans form and converts to a cis/cis form through rotation of the center dihedral angles shown in red. This process is studied using Climbing Image Nudged Elastic Band (CINEB) and Metadynamics (MTD) via a dihedral collective variable (CV).105
- Figure 5.3 Concerted conversion between T3 and T2 cyclopentenyl cation isomers. The hypothesized transition state is shown and has a simultaneous transfer of hydrogen and methyl group, highlighted in red.106
- Figure 5.4 Formation of coke molecules from alkylcyclopentenyl cations. The reaction network is determined using the Rule Input Network Generator (RING) code and reaction and transition state energies are incorporated in a microkinetic model over zeolite catalysts. Differences may be attributed to the different initial alkylcyclopentenyl cation.108

CHAPTER 1

INTRODUCTION

Zeolites are microporous solid acid catalysts that have been used in a wide range of applications over the last 60-70 years.^{1,2} Their applications extend across many fields including chemistry, chemical engineering, and materials science.³⁻⁵ One of the primary application of zeolites is as catalysts for the refining of oil and petroleum.¹ In a similar manner, zeolite catalysts have also been used for the conversion of methanol, a simple feedstock, to a variety of different value-added products including gasoline components and olefinic precursors.³ These methanol conversions occur through a complex process that in the early 1990's was coined the "hydrocarbon pool" mechanism.⁶ In this mechanism there are several coexisting cyclic and acyclic molecules that react intramolecularly or intermolecularly, with other molecules or the zeolite framework. Interestingly, in many instances the molecules in the hydrocarbon pool can exist as co-catalysts, ultimately participating in the formation of products.^{1,4} More recently, zeolites have been heavily studied for their ability to convert biomass feedstock to biofuels, a renewable energy.⁵ With that, a similarity between biofuel production and methanol conversion is the problem of forming unwanted byproducts, so-called "coke species," which clog pores and poison catalytic activity.^{7,8} A central problem in zeolite science is thus to understand organic transformations in zeolites, pinpoint processes that lead to coke, and turn those processes off.

Coke species form as byproducts during zeolite processes and are known to be the main cause of catalyst deactivation and decreased catalytic efficiency.¹ Due to their larger size, relative to other guest molecules, coke species render the catalyst inactive by

limiting diffusivity in the pores and access to active sites (Figure 1.1).⁸ Once a zeolite is fully deactivated by the formation of coke, energy must be expended to regenerate the catalyst for it to be useful again.^{1,8} Furthermore, carbon from the feedstock is wasted as it is converted to coke species instead of the desired products. These issues of energy expenditure and loss of carbon result in an overall decrease in the efficiency of zeolite catalysis and subsequent increase in the effective cost of biofuels, rendering them too expensive at present for broad adoption. Thus, increasing the efficiency of zeolites is required, and can be achieved through a deeper understanding of coke formation to limit its formation.

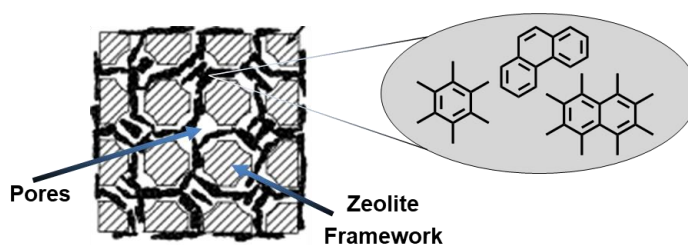


Figure 1.1 Schematic representation of coke formation in zeolites. The theoretical coke molecules are shown in the grey circle and are shown to clog the pores limiting diffusivity and rendering the catalyst inactive. Figure adapted from Ref.¹

The understanding of how coke species form during zeolite processes is still a developing field. Much of the work done to this end has found that coke species form as polynuclear aromatic carbons or highly methylated benzenes.^{1,7} What is left rather poorly known are the atomic-level mechanisms by which these coke species form in zeolite pores, and the role the zeolite framework plays in such reactions. Many experimental and theoretical contributions have investigated the role of cyclic species in the formation of coke.^{4,9} For instance, it is thought that five and six-membered cyclic species form during catalysis as active intermediates, but also act as precursors to deactivating coke species.^{4,9}

With rapid increases in computational power and collaborative efforts these findings are now being further studied to better understand coke formation in zeolites. To that end, the forefront of coke formation chemistry in zeolites includes the following general questions:

- What key mechanisms are involved in coke formation during zeolite catalysis?
- How do interactions between the zeolite framework and guest molecules impact chemical transformations occurring in the pores?
- Which techniques provide the best approaches for investigating coke formation in zeolites?

The present work will investigate protonation, cyclization, and isomerization reactions of cyclic and acyclic olefinic “proxies” for coke-related reactants inside the pores of zeolite catalysts to further the understanding of coke formation (Figure 1.2). We will focus on host-guest interactions between zeolite and adsorbed molecules through the lens of molecular vibrations and shape-selectivity. We will utilize high-level computational techniques in close collaboration with experimental research to provide insight on the significance of host-guest interactions for the aforementioned reactions. In particular, we report results below from studies in collaboration with Prof. Friederike Jentoft and Dr. Eric Hernandez from the UMass Amherst Department of Chemical Engineering. We are grateful for this collaboration and the opportunity to include their experimental data, for comparison to our calculations, in the present dissertation.

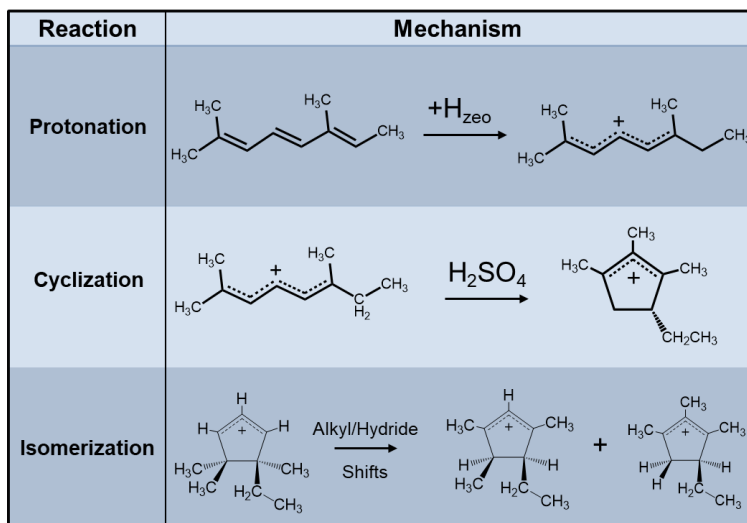


Figure 1.2 Summary of the reactions studied in this work and current understanding of the mechanisms by which they occur. Protonation of acyclic olefins (top) occurs readily in zeolites through interaction with Brønsted acid sites. Cyclization of acyclic cations to alkylcyclopentenyl cations (middle) reported in homogeneous acid media.¹⁰ Isomerization of alkylcyclopentenyl cations (bottom) leads to more stable constitutional isomers.^{11,12} This dissertation studies these reactions in the context of molecular vibrations and shape-selectivity.

Interaction between a given guest molecule and a host zeolite is due to the geometry and electronic structure of the guest, the chemistry of the zeolite, and the detailed structure of the zeolite's pores. Zeolites may have microporous channels, intersections and cages that are similar in size to small organic molecules¹³ (Figure 1.3), involved in the chemical process of interest.² Due to the kinetic diameters of guest molecules in relation to the diameters of a zeolite's pores and channels, the zeolite can exert selectivity in the chemical process. For instance, H-ZSM 5 is a commonly used zeolite for methanol conversion³ as well as biofuel synthesis.^{5,14} It has a combination of straight and “zig-zag” channels that join to form more spacious intersections that can accommodate a sphere with a diameter of 6.4 Å.¹⁵ The intricate pore structure of H-ZSM-5 has made it a well-known zeolite for its role in the selective formation of *p*-xylene, a valuable aromatic precursor, during the methanol-toluene alkylation reaction.¹⁶⁻¹⁸

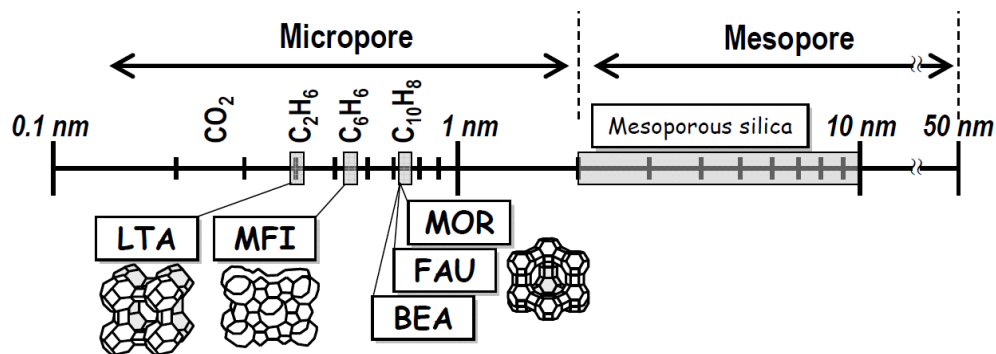


Figure 1.3 Range of zeolite pore sizes and comparison with molecular diameters of hydrocarbons. In this work we report results on MFI and MOR zeolites labeled above. Figure reproduced from Ref.¹³

Another zeolite we consider in this work, H-MOR, also exhibits straight channels; these channels are slightly larger than the H-ZSM-5 intersection, being able to accommodate a sphere of diameter 6.7 \AA .¹⁵ A third zeolite we consider is H-ZSM-22, with straight channels that could accommodate a diameter of only 5.7 \AA ;¹⁵ as such, there can be hindrance of the molecule. This is the essence of how a zeolite can select towards specific molecules. This concept is known as zeolite shape-selectivity (See Figure 1.4). As mentioned above for H-ZSM-5, the *p*-xylene case exemplifies this concept. In fact, for H-ZSM-22, a more confined zeolite relative to H-ZSM-5, the selectivity towards *p*-xylene is further enhanced such that it has been reported to be as high as 92%.¹⁶ This work aims to investigate the presence of shape-selectivity in coke-related reactions and the extent by which the zeolite pore structure plays a role.

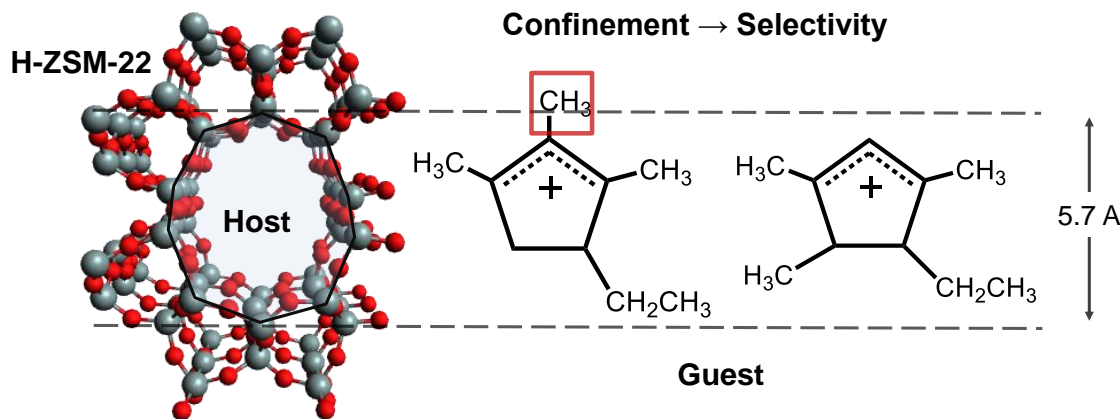


Figure 1.4 Host-Guest interaction in medium pore zeolite, H-ZSM-22. Confinement in the zeolite pore leads to shape-selectivity of products in the formation of alkylcyclopentenyl cations.

Experimental work has contributed a great deal of insight into the identification of molecules inside zeolites, as well as the way in which they react to give specific product distributions. The adsorbed state of guest molecules in zeolite pores can be monitored using experimental spectroscopy techniques.^{19,20} Vibrational and electronic absorption bands associated with guest species can be used as spectral fingerprints to determine the presence and role of acyclic and cyclic molecules in zeolites.^{4,20,21} Remarkably, these techniques can be conducted *in-situ* and gain information on the adsorbed molecules while they are reacting in real-time. Hernandez *et al.* were able to differentiate between acyclic alkenyl and cyclopentenyl cations forming inside zeolites using vibrational spectra.²¹ Experimentalists have also greatly contributed to the understanding of shape-selectivity in zeolites, as illustrated in the *p*-xylene example above. Other examples in this context include isomerization reactions of alkanes²² and polyaromatic species²³, two important groups of molecules in methanol conversion and coke formation. Expanding on these contributions raises the following questions: What are the spectroscopic fingerprints for specific molecules in a complex mixture occurring inside a zeolite? How does the presence of the zeolite impact the observed bands? What are key mechanistic steps that

give rise to the shape-selective behavior being observed in the experiment?

Computational chemistry attempts to aid in answering these questions through collaboration with experimental research. In the following chapters we outline examples of such cases where experimental work is coupled with computational techniques to elucidate spectra of complex mixtures and investigate the extent of shape-selectivity in zeolites.

Recent rapid increases in the availability of computational resources coupled with the strength of computational power have facilitated higher accuracy large scale calculations such as those required for zeolites.^{24,25} Two main facets of computational zeolite science are: (1) simulating the geometrical and electronic structures of a given zeolite and (2) computation of the mechanism(s) associated with a given reaction taking place in a zeolite. Regarding the zeolite model, zeolite unit cells can have upwards of hundreds of silicon and oxygen atoms, making electronic structure calculations very costly. In the past, techniques and protocols have been implemented to circumvent these high computational costs.⁵ For instance, A. Migués, Q. Sun, and S. Auerbach notably utilized cluster techniques to compute energetics of aldol condensations and other biofuel related reactions in H-ZSM-5.^{5,14} They were able to compute reaction energies and transition state barriers by building clusters, or cutouts of the zeolite unit cell, just big enough to achieve convergence of reaction barriers with respect to the cluster size. The cluster method ultimately avoided the use of the entire unit cell which is required for the more computationally extensive periodic calculations. However, cluster calculations using optimized cluster sizes for different reaction steps make it unwieldy to stitch

together reaction energies into a single, comprehensive micro-kinetic pathway. As such, other methods need to be considered.

Recent advances in computational resources coupled with high efficiency software have made periodic calculations of zeolites a more tractable technique.^{26,27} In these calculations, periodic boundary conditions are employed to simulate the quantum states of all valence electrons across the entire zeolite unit cell. As mentioned above, the presence of hundreds of silicon and oxygen atoms in the zeolite unit cell results in quite demanding computations.

Consider that the unit cell for H-ZSM-5 shown in Figure 1.5 has 96 SiO₂ tetrahedral units where each silicon and oxygen have four and six valence electrons, respectively, combining to give a total of 1,536 valence electrons. This means that each calculation using this unit cell in essence requires solving a 4,608-dimensional problem (1536 x 3, because of 3-D space). When also considering that we need to compute geometries and energies for multiple zeolite-guest systems, the demand for incorporating zeolite unit cells becomes even more greater. Below we implement periodic zeolite models via CP2K²⁸, an efficient computational modeling software used for solid state and quantum chemistry applications. What sets CP2K apart from many other electronic structure programs is its implementation of a plane wave auxiliary basis set to represent electron density in combination with a Gaussian orbital scheme for valence electrons.²⁹ In short, this dual-basis set approach allows for quicker Fourier transform calculations and ultimately aims to achieve linear-scaling of electronic structure algorithms. Due to the advances in algorithms, such as the dual-basis set in CP2K, we are able to conduct high-

level computations on zeolite-guest systems using periodic unit cells as we discuss in the following chapters.

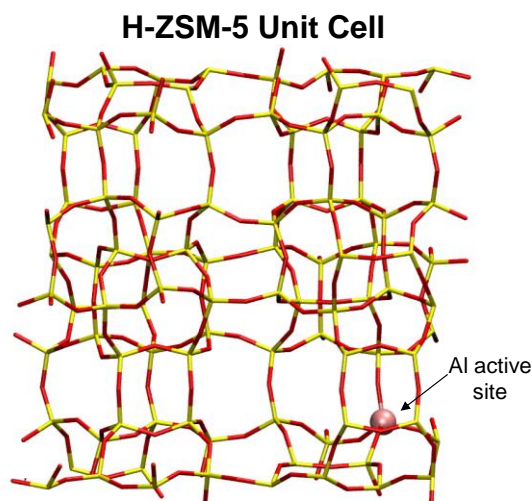


Figure 1.5 Representative H-ZSM-5 unit cell used in periodic calculations via CP2K. Each unit cell consists of a single Al atom substitution corresponding to the active site of the catalyst.

Once the model is established, the next step is computing the reaction mechanism in the zeolite. The standard approach for computing reaction mechanisms in heterogeneous catalysis in general, and in zeolite science in particular, is to compute minimum energy pathways, also known as zero-Kelvin pathways. Techniques that yield minimum energy pathways do not explicitly account for thermal fluctuations, temperature, or entropy – which can alter reaction mechanisms. Instead, they simply compute the electronic energy along the steepest descent pathway from reactant to transition state to product. Early in my doctoral studies we performed a head-to-head comparison of finite temperature and zero-Kelvin methods for studying the mechanism of aldol condensation in zeolites, focusing on the initial acid-catalyzed enol formation step.

Interestingly, we discovered different mechanisms coming from finite temperature and zero-Kelvin methods, which raised concern over the use of zero-Kelvin techniques to simulate reactions at finite temperatures. From that time until now, we have developed a more nuanced perspective on the interplay between zero-Kelvin and finite temperature methods. To this end, we first introduce standard computational approaches for pursuing zero-Kelvin and finite temperature mechanisms and barriers.

One of the most used techniques for zero-Kelvin pathways is the Climbing Image-Nudged Elastic Band (CINEB) method.³⁰ CINEB uses snapshots of the system throughout a given reaction, connecting them with conceptual springs, and determines the energies of the endpoints relative to one another as well as the transition state and corresponding system geometries. The consideration of thermal fluctuations and temperature can then be achieved post-calculation through models such as the harmonic oscillator approximation. These calculations can be relatively efficient even with a high level of electronic structure theory and can be rather accurate in the energetics and geometry predictions at zero Kelvin.

The alternative to the zero-Kelvin approach is the use of finite temperature calculations, which yield free-energy barriers for reaction steps at particular temperatures. Finite temperature calculations are relatively more computationally expensive due to the requirement of long dynamics calculations.^{26,31} For this reason, these calculations are less common but recently are starting to be applied to zeolites and the reactions therein. Ultimately, these sampling techniques capture the correct anharmonic statistical mechanics underlying reaction free energies and barriers.³² Initially, in the beginning of my doctoral work, we were interested in implementing finite temperature techniques

would result in different mechanisms for reactions that had been previously studied using zero-Kelvin techniques. As discussed above, we had already found an example where these methods yield different mechanisms. More recently, however, we have found a new perspective on finite temperature and its applicability as a computational tool. Our implementation of these new ideas is discussed in detail in Chapter 4. In brief, we will utilize CINEB to compute reaction barriers that involve the motion of relatively few degrees of freedom. These CINEB calculations can fail when many degrees of freedom are involved, that is, when the mechanism involves more collective motion. In such cases, we will apply finite temperature sampling to capture collective reactive events and use those as initial conditions for CINEB calculations. As we show in Chapter 4, this combination yields an effective computational strategy for simulating an array of complex reactions in zeolites.

The work described below involves the computation of IR spectra for direct comparison with experiment. Several computational methods are available for calculating IR spectra of condensed-phase systems, including normal mode analysis (NMA), and correlation-function analysis via ab initio molecular dynamics (AIMD), each with its advantages and disadvantages.³³ By invoking the harmonic oscillator approximation, NMA provides a direct model of IR spectra with band assignments provided by the normal mode coordinates, requiring the calculation and diagonalization of the force constant matrix of second derivatives at optimized geometries.³⁴ In contrast, one can obtain IR spectra at finite temperatures, and beyond the harmonic approximation, by Fourier transforming the dipole autocorrelation function computed by AIMD.³⁵ We note that the AIMD approach to IR spectra does not necessarily allow for facile assignment of

IR bands, and can be quite computationally demanding.³³ In the present work, we computed IR spectra of olefin/zeolite systems using NMA because of its computational efficiency, ease of making band assignments, and direct comparability with gas-phase NMA calculations. Within the NMA approach, we modeled finite temperature effects on IR spectra efficiently by averaging spectra for different snapshots from ab initio MD, as described in Chapter 2.

Here we briefly describe the results of this work. First, we used periodic DFT to model vibrational spectra of acyclic olefins in large pore zeolites and determine the nature of host-guest interactions. We found that there exist two regimes of interaction between zeolite and guest: (1) strong interaction that leads to significant changes in the spectrum attributed to protonation of the olefin; and (2) minimal interaction from Coulombic forces that result in little to no change in the IR bands associated with allylic stretches. Secondly, in close collaboration with experiment, we investigated the formation of alkylcyclopentenyl cations from acyclic olefinic precursors and the extent of shape-selectivity. We found that shape-selectivity is occurring, such that large pore zeolites yield C-2 methyl substituted cyclopentenyl cations, whereas the more confined nature of medium pore zeolites yield C-2 hydrogen substituted cyclopentenyl cations. Moreover, our DFT-predicted thermodynamics do not coincide with the product distributions seen in the experiment which suggests possible kinetic control over product formation. Finally, we studied the extent of kinetic control on the isomerization of alkylcyclopentenyl cations in medium pore zeolites. We found that isomerization leading to methyl and hydrogen C-2 substituted cyclopentenyls occurs through a multi-pathway reaction network. We built a microkinetic model for the isomerization in zeolites H-

ZSM-5 and H-ZSM-22 and found that product distributions were sensitive to the pore structure in which the isomerization occurred. Ultimately, we will highlight that the interactions between zeolite framework and guest can manifest in differences in molecular vibrations and product distributions.

1.2 References

- (1) Yarulina, I.; Chowdhury, A. D.; Meirer, F.; Weckhuysen, B. M.; Gascon, J. Recent Trends and Fundamental Insights in the Methanol-to-Hydrocarbons Process. *Nat. Catal.* **2018**, *1* (6), 398–411. <https://doi.org/10.1038/s41929-018-0078-5>.
- (2) Auerbach, S. M.; Carrado, K. A.; Dutta, P. K. *Handbook of Zeolite Science and Technology*; Marcel Dekker Inc.: New York, NY, 2003.
- (3) Unni, O.; Stian, S.; Morten, B.; Pablo, B.; W., J. T. V.; Finn, J.; Silvia, B.; Petter, L. K. Conversion of Methanol to Hydrocarbons: How Zeolite Cavity and Pore Size Controls Product Selectivity. *Angew. Chemie Int. Ed.* **2012**, *51* (24), 5810–5831. <https://doi.org/10.1002/anie.201103657>.
- (4) Wulfers, M. J.; Jentoft, F. C. The Role of Cyclopentadienium Ions in Methanol-to-Hydrocarbons Chemistry. *ACS Catal.* **2014**, *4* (10), 3521–3532. <https://doi.org/10.1021/cs500722m>.
- (5) Miguez, A. N.; Sun, Q.; Vaitheeswaran, S.; Sherman, W.; Auerbach, S. M. On the Rational Design of Zeolite Clusters for Converging Reaction Barriers: Quantum Study of Aldol Kinetics Confined in HZSM-5. *J. Phys. Chem. C* **2018**, *122* (40), 23230–23241. <https://doi.org/10.1021/acs.jpcc.8b08684>.
- (6) Dahl, I. M.; Kolboe, S. On the Reaction Mechanism for Propene Formation in the MTO Reaction over SAPO-34. *Catal. Letters* **1993**, *20* (3), 329–336. <https://doi.org/10.1007/BF00769305>.
- (7) Liu, B.; Slocombe, D.; AlKinany, M.; AlMegren, H.; Wang, J.; Arden, J.; Vai, A.; Gonzalez-Cortes, S.; Xiao, T.; Kuznetsov, V.; et al. Advances in the Study of Coke Formation over Zeolite Catalysts in the Methanol-to-Hydrocarbon Process. *Appl. Petrochemical Res.* **2016**, *1*–7. <https://doi.org/10.1007/s13203-016-0156-z>.
- (8) Daniel, D.; Konstantin, R.; Wladimir, R. Experimental and Computational Investigations of the Deactivation of H-ZSM-5 Zeolite by Coking in the Conversion of Ethanol into Hydrocarbons. *ChemCatChem* **2012**, *4* (6), 802–814. <https://doi.org/10.1002/cctc.201200015>.
- (9) Olsbye, U.; Svelle, S.; Lillerud, K. P.; Wei, Z. H.; Chen, Y. Y.; Li, J. F.; Wang, J. G.; Fan, W. B. The Formation and Degradation of Active Species during Methanol Conversion over Protonated Zeotype Catalysts. *Chem. Soc. Rev.* **2015**, *44* (20), 7155–7176. <https://doi.org/10.1039/C5CS00304K>.
- (10) Sorensen, T. S. The Synthesis and Reactions of Divinyl Carbonium Ions. *Can. J. Chem.* **1964**, *42* (12), 2768–2780. <https://doi.org/10.1139/v64-410>.
- (11) Zhang, W.; Zhang, M.; Xu, S.; Gao, S.; Wei, Y.; Liu, Z. Methylcyclopentenyl Cations Linking Initial Stage and Highly Efficient Stage in Methanol-to-Hydrocarbon Process. *ACS Catal.* **2020**, *10* (8), 4510–4516. <https://doi.org/10.1021/acscatal.0c00799>.
- (12) Sorensen, T. S. Directly Observable Carbonium Ion-Carbonium Ion Rearrangements. I. Kinetics and Equilibria in the Interconversion of Trialkylcyclopentenyl Cations. *J. Am. Chem. Soc.* **1967**, *89* (15), 3782–3794. <https://doi.org/10.1021/ja00991a019>.
- (13) Tago, T.; Masuda, T. *Zeolite Nanocrystals- Synthesis and Applications*; 2010.
- (14) Miguez, A. N.; Vaitheeswaran, S.; Auerbach, S. M. Density Functional Theory Study of Mixed Aldol Condensation Catalyzed by Acidic Zeolites HZSM-5 and HY. *J. Phys. Chem. C* **2014**, *118* (35), 20283–20290. <https://doi.org/10.1021/jp504131y>.
- (15) Baerlocher, C.; McCusker, L. B. *International Zeolite Association: Database of Zeolite Structures*.
- (16) Kumar, R.; Ratnasamy, P. Isomerization and Formation of Xylenes over ZSM-22 and ZSM-23 Zeolites. *J. Catal.* **1989**, *116* (2), 440–448. <https://doi.org/https://doi.org/10.1016/0021->

- 9517(89)90110-3.
- (17) Wang, C.; Zhang, L.; Huang, X.; Zhu, Y.; Li, G. (Kevin); Gu, Q.; Chen, J.; Ma, L.; Li, X.; He, Q.; et al. Maximizing Sinusoidal Channels of HZSM-5 for High Shape-Selectivity to p-Xylene. *Nat. Commun.* **2019**, *10* (1), 4348. <https://doi.org/10.1038/s41467-019-12285-4>.
 - (18) Cheng, Y.-T.; Wang, Z.; Gilbert, C. J.; Fan, W.; Huber, G. W. Production of P-Xylene from Biomass by Catalytic Fast Pyrolysis Using ZSM-5 Catalysts with Reduced Pore Openings. *Angew. Chemie Int. Ed.* **2012**, *51* (44), 11097–11100. <https://doi.org/10.1002/anie.201205230>.
 - (19) Marchese, L.; Frache, A.; Gianotti, E.; Martra, G.; Causà, M.; Coluccia, S. ALPO-34 and SAPO-34 Synthesized by Using Morpholine as Templating Agent. FTIR and FT-Raman Studies of the Host–Guest and Guest–Guest Interactions within the Zeolitic Framework. *Microporous Mesoporous Mater.* **1999**, *30* (1), 145–153. [https://doi.org/10.1016/S1387-1811\(99\)00023-2](https://doi.org/10.1016/S1387-1811(99)00023-2).
 - (20) Sacchetto, V.; Olivas Olivera, D. F.; Paul, G.; Gatti, G.; Braschi, I.; Marchese, L.; Bisio, C. On the Adsorption of Gaseous Mixtures of Hydrocarbons on High Silica Zeolites. *J. Phys. Chem. C* **2017**, *121* (11), 6081–6089. <https://doi.org/10.1021/acs.jpcc.6b11577>.
 - (21) Hernandez, E. D.; Jentoft, F. C. Spectroscopic Signatures Reveal Cyclopentenyl Cation Contributions in Methanol-to-Olefins Catalysis. *ACS Catal.* **2020**, *10* (10), 5764–5782. <https://doi.org/10.1021/acscatal.0c00721>.
 - (22) Poursaeidesfahani, A.; de Lange, M. F.; Khodadadian, F.; Dubbeldam, D.; Rigutto, M.; Nair, N.; Vlugt, T. J. H. Product Shape Selectivity of MFI-Type, MEL-Type, and BEA-Type Zeolites in the Catalytic Hydroconversion of Heptane. *J. Catal.* **2017**, *353*, 54–62. <https://doi.org/10.1016/j.jcat.2017.07.005>.
 - (23) Sugi, Y.; Vinu, A. Alkylation of Biphenyl over Zeolites: Shape-Selective Catalysis in Zeolite Channels. *Catal. Surv. from Asia* **2015**, *19* (3), 188–200. <https://doi.org/10.1007/s10563-015-9193-3>.
 - (24) Manookian, B.; Hernandez, E. D.; Baer, M. D.; Mundy, C. J.; Jentoft, F. C.; Auerbach, S. M. Experimental and DFT Calculated IR Spectra of Guests in Zeolites: Acyclic Olefins and Host–Guest Interactions. *J. Phys. Chem. C* **2020**, *124* (19), 10561–10572. <https://doi.org/10.1021/acs.jpcc.0c01225>.
 - (25) Lesthaeghe, D.; Speybroeck, V. Van; Marin, G. B.; Waroquier, M. The Rise and Fall of Direct Mechanisms in Methanol-to-Olefin Catalysis : An Overview of Theoretical Contributions. **2007**, 8832–8838. <https://doi.org/10.1021/ie0613974>.
 - (26) Alexopoulos, K.; Lee, M. S.; Liu, Y.; Zhi, Y.; Liu, Y.; Reyniers, M. F.; Marin, G. B.; Glezakou, V. A.; Rousseau, R.; Lercher, J. A. Anharmonicity and Confinement in Zeolites: Structure, Spectroscopy, and Adsorption Free Energy of Ethanol in H-ZSM-5. *J. Phys. Chem. C* **2016**, *120* (13), 7172–7182. <https://doi.org/10.1021/acs.jpcc.6b00923>.
 - (27) Alexopoulos, K.; John, M.; Van der Borght, K.; Galvita, V.; Reyniers, M.-F.; Marin, G. B. DFT-Based Microkinetic Modeling of Ethanol Dehydration in H-ZSM-5. *J. Catal.* **2016**, *339*, 173–185. <https://doi.org/10.1016/j.jcat.2016.04.020>.
 - (28) VandeVondele, J.; Krack, M.; Mohamed, F.; Parrinello, M.; Chassaing, T.; Hutter, J. QUICKSTEP: Fast and Accurate Density Functional Calculations Using a Mixed Gaussian and Plane Waves Approach. *Comput. Phys. Commun.* **2005**, *167* (2), 103–128.
 - (29) Kühne, T. D.; Iannuzzi, M.; Del Ben, M.; Rybkin, V. V.; Seewald, P.; Stein, F.; Laino, T.; Khaliullin, R. Z.; Schütt, O.; Schiffmann, F.; et al. CP2K: An Electronic Structure and Molecular Dynamics Software Package - Quickstep: Efficient and Accurate Electronic Structure Calculations. *J. Chem. Phys.* **2020**, *152* (19), 194103. <https://doi.org/10.1063/5.0007045>.
 - (30) Henkelman, G.; Uberuaga, B. P.; Jónsson, H. A Climbing Image Nudged Elastic Band Method for Finding Saddle Points and Minimum Energy Paths. *J. Chem. Phys.* **2000**, *113* (22), 9901–9904. <https://doi.org/10.1063/1.1329672>.
 - (31) S., C. C.; Alice, R.; Alessandra, C.; Andrés, S. Ab Initio Molecular Dynamics Study of the Keto–Enol Tautomerism of Acetone in Solution. *ChemPhysChem* **2006**, *7* (6), 1229–1234. <https://doi.org/10.1002/cphc.200600007>.
 - (32) Gervasio, A. L. and F. L. Metadynamics: A Method to Simulate Rare Events and Reconstruct the Free Energy in Biophysics, Chemistry and Material Science. *Reports Prog. Phys.* **2008**, *71* (12), 126601.
 - (33) Mathias, G.; Baer, M. D. Generalized Normal Coordinates for the Vibrational Analysis of

Molecular Dynamics Simulations. *J. Chem. Theory Comput.* **2011**, *7* (7), 2028–2039. <https://doi.org/10.1021/ct2001304>.

- (34) De Moor, B. A.; Ghysels, A.; Reyniers, M.-F.; Van Speybroeck, V.; Waroquier, M.; Marin, G. B. Normal Mode Analysis in Zeolites: Toward an Efficient Calculation of Adsorption Entropies. *J. Chem. Theory Comput.* **2011**, *7* (4), 1090–1101. <https://doi.org/10.1021/ct1005505>.
- (35) Agarwal, V.; Huber, G. W.; Conner, W. C.; Auerbach, S. M. Simulating Infrared Spectra and Hydrogen Bonding in Cellulose I β at Elevated Temperatures. *J. Chem. Phys.* **2011**, *135* (13), 134506. <https://doi.org/10.1063/1.3646306>.

CHAPTER 2

EXPERIMENTAL AND DFT CALCULATED IR SPECTRA OF GUESTS IN ZEOLITES: ACYCLIC OLEFINS AND HOST-GUEST INTERACTIONS

2.1 Introduction

The mechanisms by which hydrocarbons transform within acidic zeolites can be quite complex and may involve long-lived organic surface species, in some instances referred to as the “hydrocarbon pool.”¹ The various chemical species in hydrocarbon pools are thought to play active roles^{2,3} in some catalytic processes, but can also transform to coke – thereby deactivating a given catalyst.^{4,5} Identifying precursors in a hydrocarbon pool by characterization methods such as IR spectroscopy poses a challenge because of the complexity of coexisting molecules, possibly overlapping IR bands, and limited knowledge on the influence of zeolite-guest interactions on IR spectral shifts.⁶ One way to address this problem is to use hypothesized molecular proxies to pinpoint spectral features associated with a subset of chemical moieties, which in turn can be used to identify the makeup of a complex mixture such as the hydrocarbon pool. Acyclic dienes and trienes serve as useful model compounds, because they are the conjugated bases of species reported to exist in the hydrocarbon pool, and can interact with the acidic zeolite framework generating cyclic aromatic species that proceed to either desired products or coke.⁷ Below we report simulated IR spectra of olefins **I** and **II** (Fig. 2.1) in acidic HMOR zeolite and in non-acidic de-aluminated zeolite beta and compare to experimental data, to determine and assign unambiguous spectral fingerprints of these important species upon adsorption in zeolites.

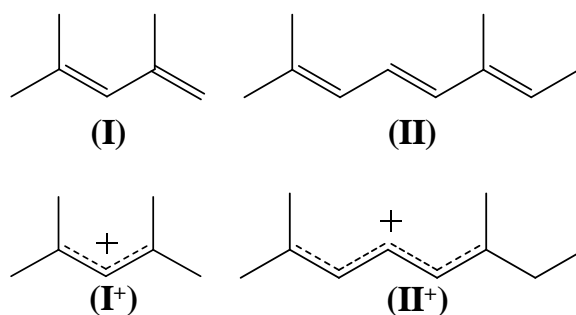


Figure 2.1 Acyclic olefins and the respective conjugate bases used in this study.

In this chapter, we report both measured and calculated IR spectra of species **I** and **II** in various zeolites. The findings detailed below were previously published in the *Journal of Physical Chemistry C*.⁸ All experiments discussed in this chapter were conducted by Dr. Eric Hernandez and Professor Friederike Jentoft in the chemical engineering department at University of Massachusetts Amherst, and are reported with their permission. The measured and computed IR spectra reported below demonstrate that adsorption of **I** on non-acidic zeolite beta leads to a conformational mixture that contains mostly the lower-energy gauche s-cis conformer. The data below support the notion that protonation readily occurs upon adsorption of neutral acyclic olefins **I** and **II** in HMOR zeolite at 20 °C. Remarkably, the experimental and computational results also suggest that for certain spectroscopic features, such as allylic stretching bands, understanding the vibrational spectra of alkenyl and alkadienyl cations in acidic zeolites requires only taking into account the relevant state of the gas-phase species.

2.2 Methods

2.2.1 Experimental Methods

For a detailed description of the experimental methods, we direct the reader to the article published in Journal of Physical Chemistry C.⁸

2.2.2 Computational Methods

2.2.2.1 Modeling the Zeolite.

The unit cell for calcined MOR was obtained from the Structure Commission of The International Zeolite Association,^{9,10} and the T4 crystallographic site was substituted with an Al atom resulting in a negative charge which was compensated by a proton. The T4 site is located along the 12-membered-ring straight channel of MOR and exhibits high activity and easy accessibility.^{11,12} Previously optimized¹³ unit cell parameters for HMOR [$a = 18.323 \text{ \AA}$, $b = 20.795 \text{ \AA}$, $c = 7.626 \text{ \AA}$, $\alpha = \beta = \gamma = 90^\circ$] were used and agree well with experimental data¹⁴($a = 18.094 \text{ \AA}$, $b = 20.516 \text{ \AA}$, $c = 7.542 \text{ \AA}$, $\alpha = \beta = \gamma = 90^\circ$). To avoid interaction between guest molecules in adjacent cells, we expanded the unit cell in the c-direction creating a 1x1x2 supercell (Fig. 2) with the formula $\text{H}_2\text{Al}_2\text{Si}_{94}\text{O}_{192}$ (Si/Al ratio of 47) to be used in all acidic zeolite calculations. A similar approach was used for the non-acidic case, where, in contrast, no Al atoms were incorporated in the super cell. ($\text{Si}_{96}\text{O}_{192}$).

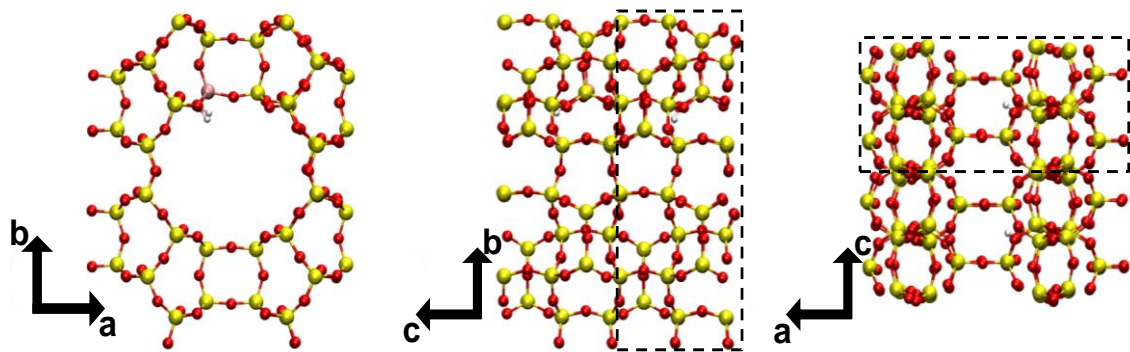


Figure 2.2 Illustration of the HMOR supercell used for periodic DFT calculations. Along the c-direction, an extra unit cell was included to create the $1 \times 1 \times 2$ supercell that limits interaction of guest molecules in neighboring periodic images. The HMOR unit cell is highlighted by the dashed box.

2.2.2.2 Electronic Structure Calculations

We used CP2K¹⁵ for periodic DFT of zeolite-guest and isolated neutral guest systems allowing geometry optimization, normal mode analysis (NMA) with convenient visualization of normal modes, and ab initio molecular dynamics to model IR spectra at finite temperatures. We used periodic DFT within the generalized gradient approximation with the BLYP exchange-correlation functional as implemented in CP2K.¹⁵ The commonly used hybrid functional, B3LYP, is not available within CP2K and therefore limited us to the BLYP functional. However, based on our results, as well as those previously reported in the literature,^{16,17} the BLYP functional provides adequate frequencies for qualitative, and in many cases, quantitative comparisons with experimental spectra. Corrections by Grimme et al. (DFT-D3) are used to take into account dispersion forces and obtain more accurate energetics.¹⁸ For core electrons, Goedecker-Teter-Hutter norm-conserving pseudopotentials optimized for the BLYP functional are used,¹⁹ while the valence electron wavefunctions are expanded in terms of a triple- ζ valence polarized basis set (TZVP) comparable to 6-311G(d).²⁰ Within the

CP2K scheme,¹⁵ the electron density is described using an auxiliary plane-wave basis set with a 400 Ry cutoff.

Gas-phase protonated species were modeled using the Gaussian 09 software package.²¹ Calculations were performed using the BLYP functional via DFT and a 6-311G(d) basis set to describe the core and valence electrons, thus allowing for appropriate comparisons between gas-phase and zeolite-adsorbed states via computational results from Gaussian and CP2K.

2.2.2.3 Dynamics

Computed IR spectra of guest molecules **I** and **II** in HMOR zeolite were obtained using two different models: full optimization or ensemble average. Both models are described below.

For the full optimization model, either guest was placed inside the pore of HMOR near the Brønsted acid site. A full geometry optimization (zeolite and guest) was then conducted followed by NMA. We ran test calculations where we included in NMA successively more zeolite atoms close to guest **II**⁺ [within a radius of $\delta(\text{Å})$], all the way up to including the full HMOR zeolite. Figure 2.9 in Appendix (Section 2.5) shows the resulting spectra in the IR region of interest (1300–1700 cm^{-1}), indicating that including zeolite atoms has no effect on the positions of the bands in this region; however there does appear to be a progressive increase in the overall intensity with inclusion of more framework atoms. As such, we included only the guest atoms in NMA for computing IR spectra. All frequencies were scaled using the vibrational scaling factor for BLYP/6-311G(d) of 0.989, reported in the NIST online database.²² The resulting frequencies and intensities from NMA were incorporated into Lorentzian functions with a full width at

half maximum (FWHM) of 15 cm^{-1} , as we have done in our previous spectroscopic simulations,^{23,24} to simulate IR spectra within the full optimization model.

For the ensemble average model, we performed ab initio molecular dynamics (AIMD) of each zeolite-guest system at experimentally relevant temperatures ($T = 20, 130, 200\text{ }^{\circ}\text{C}$) to test whether thermal fluctuations influence IR spectra of these zeolite-guest systems. Each system was initialized with a guest molecule in the supercell at the active site. AIMD was then performed for 8–9 ps using a 0.5 fs time step and a Nosé-Hoover chain thermostat with a frequency of 1000 cm^{-1} . Next, 30 snapshots of the system were extracted at random from the latter 6–7 ps of each AIMD simulation. For each image, we geometry-optimized the guest while keeping the zeolite framework fixed. Such an approach conserves the thermal fluctuations of the zeolite while keeping the resulting normal mode frequencies real – otherwise each snapshot can produce different numbers of vibrational modes. NMA was then performed on the guest, once again omitting the zeolite atoms, and the resulting (scaled) frequencies and intensities were incorporated into Lorentzian functions with a FWHM of 15 cm^{-1} to yield a simulated spectrum for each snapshot. Finally, all 30 spectra were averaged to provide the ensemble averaged spectrum for the guest at a desired experimental temperature.

To investigate the thermodynamics of guest and zeolite-guest systems within the periodic DFT scheme, we computed Helmholtz free energies in the NVT ensemble via NMA within a multidimensional harmonic oscillator model using the formula shown in the Appendix, Section 2.5.2. The harmonic frequencies were obtained from NMA after full optimization to compute the change in free energy between neutral and protonated

states of each acyclic olefin. We also used these free energies to analyze stabilities of various conformers of **I**, **II**, **I**⁺, and **II**⁺ as described in detail below.

Investigating the impact of zeolite-guest interactions on spectral features of protonated guests requires the calculation of IR spectra in the gas phase, for comparison. Periodic boundary conditions require a net charge of zero in a given cell. Thus, to model isolated, protonated guests, we employed Gaussian 09 software to obtain spectra of isolated **I**⁺ and **II**⁺. For each gas-phase species considered, we carried out a full geometry optimization followed by NMA to obtain vibrational frequencies and intensities. Gas-phase calculations were performed using the BLYP/6-311G(d) model chemistry as implemented in Gaussian 09,²¹ for consistency with the BLYP/TZVP treatment within CP2K for zeolite-guest systems. The resulting BLYP/6-311G(d) frequencies were scaled and incorporated into Lorentzian functions with a FWHM of 15 cm⁻¹ to obtain a computed IR spectrum.

2.2.2.4 Conformational Analyses

Each of the species **I**, **II**, and **II**⁺ exhibits a rich array of conformational states. (Species **I**⁺ exhibits only a single conformer.) We modeled this conformational space to investigate whether mixtures of conformers are present or whether a single conformer predominates. To address this issue, we computed relative free energies and IR spectra of all relevant conformers in gas-phase and zeolite-adsorbed states. We used these free energies to Boltzmann-weight the single-conformer IR spectra, to yield a conformationally-averaged IR spectrum for comparison with experimental IR data. We also utilized techniques to compute the barriers between relevant conformational states for olefin **I**. Within the CP2K scheme we employed the climbing image-nudged elastic

band method with seven replicas to obtain transition states and corresponding free energies of activation.

2.3 Results and Discussion

In this section we discuss our findings regarding the use of experimental and computational IR spectra to elucidate the nature of adsorbed acyclic olefins. First, we consider the conformational state of olefin **I** in non-acidic de-aluminated beta zeolite (deAl-BEA) using computed thermodynamics and comparison of computed spectra with experiment. Second, we investigate how adsorption of guests **I** and **II** in (acidic) HMOR affects the corresponding IR spectra. Finally, we analyze the nature of electrostatic interactions between a negatively charged framework MOR^- and adsorbed cations I^+ and II^+ , as probed through the corresponding IR spectra.

2.3.1 Adsorption of of 2,4-Dimethyl-1,3-pentadiene on a Non-acidic Framework: Contributions of Rotational Conformers to IR Spectrum.

We begin by using IR spectroscopy to determine the nature of molecule **I** adsorbed on non-acidic, large-pore zeolites. We are interested in adsorption in all-silica zeolites because it provides data on a baseline level of confinement without acid sites, to be used in comparison with results in Sec. 2.3.2 on HMOR zeolite, which contains acid sites. We will discuss findings from experimental IR measurements of **I** over deAl-BEA conducted by Dr. Hernandez and Prof. Jentoft. As discussed above in Sec. 2.2, we model the pore space of deAl-BEA by using DFT to compute properties of molecule **I** in all-silica MOR, which contains cavities very similar in size to those of BEA. Regarding guest species **I**, it has been reported that molecules of this nature exist in either s-cis or s-

trans conformations,^{25,26} prompting us to begin by investigating the equilibrium between the two conformers using computed Gibbs and Helmholtz energies, and the impact of these conformers on the IR spectra.

Dienes such as molecule **I** have a dihedral angle along the single bond in between the two C=C bonds, resulting in two stable conformations denoted as s-trans and s-cis, where the 's' indicates torsion around the single bond. Previous reports on substituted dienes suggest that the s-trans conformer can be lower in energy by upwards of 3 kcal/mol, thus exhibiting higher population at thermal equilibrium.^{25,26} We investigated the thermodynamic stabilities of conformers of **I** by computing free energy profiles for the s-cis and s-trans conformers in vacuum and over all-silica MOR (Table 2.3 in Appendix). Interestingly, we found that a gauche s-cis conformation of **I** has lower free energies than its s-trans counterpart at 20 °C. We found the gauche s-cis (with a dihedral angle of -44°) to be lower in Helmholtz free energy by 0.27 kcal/mol in all-silica MOR. In vacuum, we found a similar trend where the gauche s-cis is lower in Helmholtz free energy by 0.26 kcal/mol (Table 2.3 in Appendix). We found from visual inspection of the highest-occupied molecular orbitals (HOMOs in Fig. 2.3) that the surprising stability of the gauche s-cis conformation arises from electron delocalization between pi-bonds and nearby methyl groups, which is possible only in the gauche s-cis conformation. In particular, Fig. 2.3 shows the phase (i.e., sign) of the HOMO in red/blue. In the s-trans conformation, the HOMO of the conjugated diene exhibits a nodal plane between the two pi-bonded regions, represented by the change in color within the orbital. However, at a dihedral angle of -44° , the gauche s-cis conformation is stabilized by an extended region of conjugated electron density shown in blue, involving the pi-system and the

neighboring methyl group. Such extended conjugation appears impossible in the s-trans conformer.

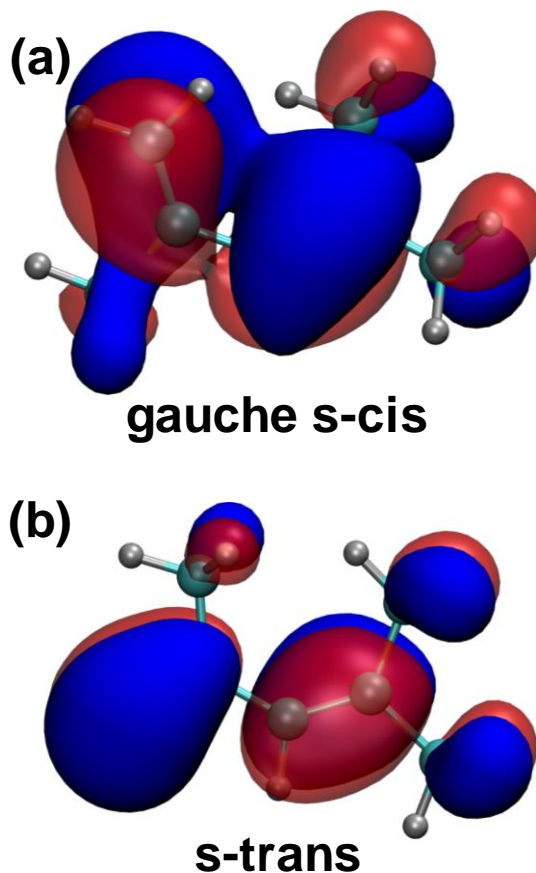


Figure 2.3 Highest occupied molecular orbitals (HOMOs) of rotational conformers for olefin I computed in the gas-phase, where the red/blue denotes the phase (sign) of the HOMO. Extended region of conjugated electron density involving neighboring methyl group, shown in blue, lowers energy for (a) gauche s-cis conformer relative to (b) s-trans conformer.

To determine whether IR spectra are expected to exhibit an equilibrium distribution of conformers of species **I**, we computed the rotational activation free energies for vacuum and zeolite-adsorbed (all-silica MOR) conformational transitions. Such barriers help to determine whether conformational transitions and equilibrium are likely under experimental conditions of temperature and observation time. We carried out these calculations by employing a climbing-image nudged elastic band technique with

seven images. Figure 2.10 in the Appendix shows the free energy profile for rotation of species **I** along its C-C single bond in all-silica MOR. We also computed rotational barriers for **I** in the gas phase with other, more accurate model chemistries and found qualitatively similar results to those in Fig. 2.10 (in Appendix - also see Table 2.3). Notably, the barrier for rotation in MOR of 3.85 kcal/mol is higher than the vacuum value of 1.46 kcal/mol, most likely due to steric hindrance inside the MOR pore. Barriers of these magnitudes at 20 °C suggest rotational timescales of no more than 100 ps, indicating sufficiently rapid conformational transitions to produce an equilibrium distribution in the zeolite. For this reason, we computed IR spectra for each stable conformer separately and averaged them with Boltzmann weighting for comparison with experimental DRIFT data, as we discuss below.

Our effort to interpret IR spectra and investigate the effects of a zeolite framework on spectral features requires direct comparisons between experiment and DFT. Computational vibrational spectroscopy can be a powerful tool for analyzing experiments, but one needs to be aware of the systematic errors that arise when using DFT. In light of this, we begin by mapping out all of the IR band locations for olefin **I** over a non-acidic zeolite (deAl-BEA in experiment; all-silica MOR in theory) to determine the nature of systematic error associated with our models. In particular, we created a parity plot (Fig. 2.4a) using DFT-computed and experimental IR frequencies; Fig. 2.4b highlights the signs and magnitudes of discrepancies in different regions of the IR spectrum. Figure 2.4 shows that in the lower-frequency region (1300–1700 cm^{-1}), associated with C–C stretches and methyl deformations, DFT provides systematically red-shifted frequencies. In contrast, in the higher-frequency region (2800–3200 cm^{-1})

associated with C-H stretches, the computed frequencies are blue-shifted from experiment. This pattern of systematic error, which has been observed by others,^{16,27} allows us to make more informed comparisons between computed and experimental spectral features for interpretation of spectra and determining the impact of zeolite-guest interactions. Now, we consider experimental and computed spectra of molecule **I** in non-acidic zeolites.

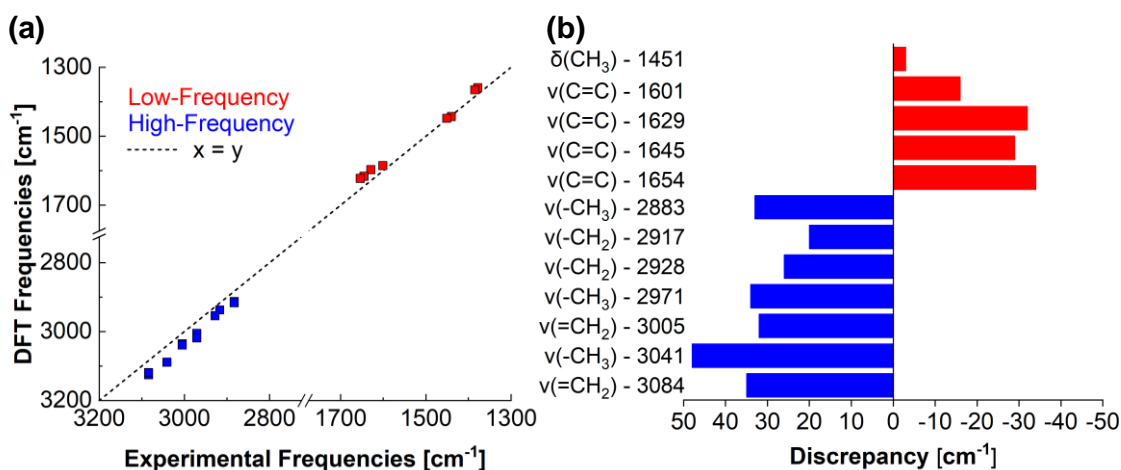


Figure 2.4 (a) Parity plot comparing experimental frequencies from DRIFTS of molecule **I** in deAl-BEA with DFT-computed frequencies of **I** over all-silica MOR. The parity line ($x=y$) is shown to highlight the different discrepancies in high- (blue) and low-frequency (red) regions of the IR spectrum. (b) Bar graph showing signs and magnitudes of discrepancies between computed and experimental frequencies (the latter shown on the left of Fig. 4b) along with their assignments.

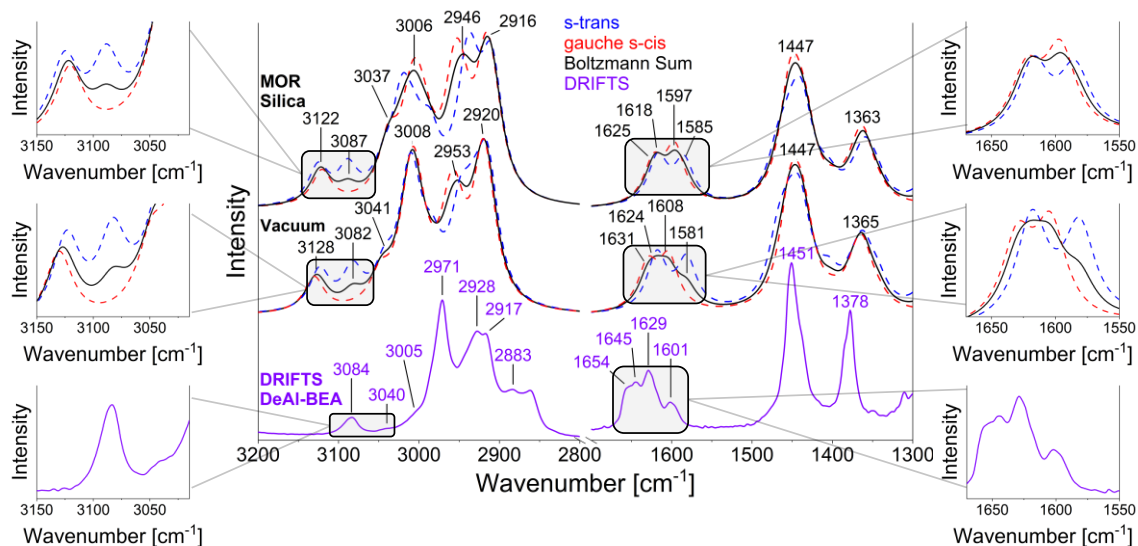


Figure 2.5 Comparison of computed and experimental spectra of molecule I. DRIFT spectrum (purple) was taken at 20 °C over DeAl-BEA. Computed spectra for molecules I in all-silica MOR (top) and in gas phase (middle). In each environment, the spectrum associated with *s-trans* (blue), *gauche s-cis* (red), and the Boltzmann sum (black) are shown. Wavenumber values apply to Boltzmann sum. Side panels focus on (left) high-frequency (C-H stretch) and (right) low-frequency (C=C stretch) regions.

We begin our interpretation of the IR spectra of olefin **I** by considering the DRIFTS over deAl-BEA. Figure 2.5 (bottom) shows the DRIFT spectrum (purple) of molecule **I** adsorbed over deAl-BEA at 20 °C, revealing several bands in both the low- and high-frequency regions of the spectrum. For the purpose of distinguishing between the two conformers, we focus on the C=C stretching region (1600–1700 cm^{-1}) and the C-H stretching region (2800–3100 cm^{-1}). Several overlapping bands are observed between 1600–1700 cm^{-1} with observable maxima at 1601, 1629, 1645 cm^{-1} and a distinct shoulder at 1654 cm^{-1} . The conjugated diene should exhibit two distinct bands in this region, associated with the symmetric and antisymmetric C=C stretches. Thus, the appearance of four bands suggests the existence of two stable conformers. In the C-H stretching region, we observe a single weak band at 3084 cm^{-1} as well as a very weak intensity band at 3040 cm^{-1} . Also, we note a strong band at 2971 cm^{-1} with a weak

shoulder at 3005 cm^{-1} . Now we detail the corresponding computed IR spectra and compare with experiment to investigate the nature of zeolite-guest interactions and conformational populations of species **I**.

Turning to the computed spectra in Fig. 2.5, the gauche s-cis and s-trans conformers exhibit distinct spectral features. Figure 2.5 shows computed IR spectra for gauche s-cis (red) and s-trans (blue) in vacuum (middle) and in all-silica MOR (top). We begin by discussing the C=C stretching bands in the lower-frequency region of the MOR spectrum (on the right of Fig. 2.5). Within this region there are a total of four bands, of which the 1597 and 1625 cm^{-1} bands are associated with the gauche s-cis conformer, and the 1585 and 1618 cm^{-1} bands are attributed to the s-trans conformer. The upper side panels on the right-hand side of Fig. 2.5 highlight this region and show that the gauche s-cis bands are slightly blue-shifted from the s-trans bands. We also find that for the gauche s-cis conformer, the symmetric C=C stretch (1597 cm^{-1}) is at a lower frequency than the antisymmetric C=C stretch (1620 cm^{-1}). Interestingly, this pattern is opposite for the s-trans where the symmetric C=C stretch (1616 cm^{-1}) is higher in frequency than the antisymmetric band (1585 cm^{-1}). The combination of these bands allows us to directly compare to the DRIFTS in the same region. We applied Boltzmann averaging of these conformer-specific spectra to produce an overall spectrum for comparison with experiment. In particular, based on the DFT-computed free energy difference stated above, the averaged spectrum in MOR has an s-trans:s-cis equilibrium ratio of 39:61 at $20\text{ }^{\circ}\text{C}$. Figure 2.5 shows the conformationally-averaged spectra (black) for **I** in vacuum (middle) and all-silica MOR (top), both showing good qualitative agreement with DRIFTS of **I** in deAl-BEA. The positions of the DFT-computed C=C stretches are

systematically red shifted from the experimental vibrations (as shown in Fig. 2.4), which allows us to assign the experimental bands to the respective conformers (see Table 2.1 for these assignments). For instance, the broad C=C stretching feature in the summed MOR spectrum exhibits some s-trans character giving rise to a small shoulder at 1585 cm^{-1} , which we assign to the low-intensity band at 1601 cm^{-1} in the DRIFTS. As such, within the C=C stretching region there are a total of four bands associated with two distinct conformers of olefin **I**, which we have distinguished by comparison of the DRIFTS with the Boltzmann-averaged computed spectrum. Our analysis shows that the overall shape of the DRIFTS in the low-frequency regions clearly indicates the presence of both s-trans and gauche s-cis conformers in appreciable populations, with slight preference for the gauche s-cis conformer.

Distinguishing the two conformers of **I** is further carried out by considering the bands in the C-H stretching region. The left-side panels of Fig. 2.5 focus on this region of the spectrum, around 3100 cm^{-1} . The DFT-computed MOR spectrum (Fig. 2.5; top) of the s-trans conformer (blue) exhibits two bands at 3125 and 3087 cm^{-1} of nearly equal intensity, while the spectrum of the gauche s-cis conformer (red) has only a single band at 3119 cm^{-1} . The overlapping bands at around 3122 cm^{-1} are associated with an antisymmetric =CH₂ stretch, which is present in both conformers. In contrast, the band at 3087 cm^{-1} is only present in the s-trans conformer, and through visualization of its normal mode, we find is associated with an asymmetric CH₃ stretch. While a frequency value of 3087 cm^{-1} for an asymmetric CH₃ is on the high end of the expected range, such high frequencies have been reported in previous studies that also considered this region of the spectrum.^{28,29} Both conformers also exhibit strong bands near 3006 cm^{-1} with a shoulder

at 3037 cm^{-1} attributed to an asymmetric CH_3 stretch and a symmetric $=\text{CH}_2$ stretch, respectively. Analyzing the Boltzmann-summed MOR spectrum of the two conformers (Fig. 2.5 top; black), we find that incorporating the s-trans species gives rise to a low intensity band at 3087 cm^{-1} in addition to a higher intensity band at 3122 cm^{-1} – the latter being associated with both conformers. Mapping these features to experiment is facilitated by recalling that the positions of the DFT-computed C-H stretches are systematically blue shifted from the experimental vibrations (as shown in Fig. 2.4). The 3087 cm^{-1} computed band of the s-trans species is attributed to the low-intensity experimental feature at 3040 cm^{-1} , while the 3122 cm^{-1} computed band maps on to the 3084 cm^{-1} DRIFTS band. The relative intensities of the computed bands at 3122 and 3087 cm^{-1} in the Boltzmann sum spectrum closely resemble those of the experimentally observed bands at 3084 and 3040 cm^{-1} , respectively. Despite the discrepancies between theory and experiment, the systematic pattern of error enables unambiguous assignments of peaks in the DRIFTS to the gauche s-cis and s-trans conformers of olefin **I** by comparison with computed spectra.

Overall, we demonstrate that our DFT-computed models allow for the interpretation of experimental IR spectra of conformers of olefin **I** in deAl-BEA. Complete assignments of observed experimental and DFT computed bands are summarized in Table 2.1. By computing IR spectra of gauche s-cis and s-trans conformers along with their relative free energies, we have constructed a useful representation of the experimental DRIFT spectrum, corroborating the presence of both conformers and the surprising abundance of the gauche s-cis conformer. Additionally, comparing vacuum and zeolite-adsorbed computed band positions in Table 2.1 reveals

very small differences, on the order of $\pm 5 \text{ cm}^{-1}$, thus suggesting very weak zeolite-guest interactions for **I** in all-silica MOR as seen through the lens of IR spectroscopy. We now turn to the study of olefins **I** and **II** in the acidic zeolite HMOR to determine the strength of zeolite-guest interactions in that system.

Table 2.1 Summary of vibrational band assignments for gauche s-cis and s-trans conformers of molecule I. Frequency values from the DRIFT spectrum over deAl-BEA are shown. Each band is associated with either the gauche s-cis or s-trans conformer as determined by comparison with computed frequencies, as highlighted by the light blue boxes. Shaded boxes highlight conformer assignments

Molecular Vibration	DRIFTS	Theory – CP2K			
	DeAl-BEA	MOR Silica		Vacuum	
		g s-cis	s-trans	g s-cis	s-trans
$\delta_{\text{sym}}(-\text{CH}_3)$	1378	1365	1359	1365	1363
$\delta_{\text{asym}}(-\text{CH}_3)$	1451	1448	1443	1447	1445
$\nu_{\text{asym}}(\text{C}=\text{C})$	1601	-	1585	-	1582
$\nu_{\text{sym}}(\text{C}=\text{C})$	1629	1597	-	1603	-
$\nu_{\text{sym}}(\text{C}=\text{C})$	1645	-	1616	-	1618
$\nu_{\text{asym}}(\text{C}=\text{C})$	1654	1620	-	1628	-
$\nu_{\text{sym}}(-\text{CH}_3)$	2883	2916	2913	2920	2918
$\nu_{\text{asym}}(-\text{CH}_2)$	2917	-	2937	-	2944
$\nu_{\text{asym}}(-\text{CH}_2)$	2928	2954	-	2958	-
$\nu_{\text{asym}}(-\text{CH}_3)$	2971	3005	3018	3007	3010
$\nu_{\text{sym}}(=\text{CH}_2)$	3005	3035	3039	3042	3038
$\nu_{\text{asym}}(-\text{CH}_3)$	3040	-	3087	-	3082
$\nu_{\text{asym}}(=\text{CH}_2)$	3084	3119	3125	3131	3124

2.3.2 Adsorption of Neutral Acyclic Olefins on Acidic HMOR Zeolite: Strong Interactions Lead to Protonation

We next studied the adsorption of polyenes **I** and **II** on the acidic zeolite HMOR via IR spectroscopy. Previous studies have found that certain olefins have high proton

affinities, suggesting that their protonation in acidic zeolites is thermodynamically favored.³⁰ As a result, we may expect strong interactions between olefins **I/II** and the HMOR Brønsted acid site. The question remains how such strong interactions manifest in the IR spectra of these zeolite-guest systems. In this section, we will discuss data from experimental IR measurements of **I** and **II** over HMOR conducted by Dr. E. Hernandez and Prof. F. Jentoft.

Figure 2.6 shows DRIFT spectra (in black) in the 1300-1700 cm^{-1} region for species **I** (Fig. 2.6a) and **II** (Fig. 2.6b) in HMOR at 20 °C. There are two main spectral features for both zeolite-guest systems: (1) a strong singlet in the 1500–1600 cm^{-1} region, and (2) a broad doublet in the 1300–1400 cm^{-1} region. Bands at 1372 cm^{-1} (**I**) and 1383 cm^{-1} (**II**) are assigned to methyl deformations.³¹ The strong singlets observed at 1548 cm^{-1} (**I**) and 1568 cm^{-1} (**II**) are characteristic of allylic cations $\nu(\text{C}=\text{C}-\text{C}^+)$,^{32,33} suggesting that protonation has taken place for both guests in HMOR.

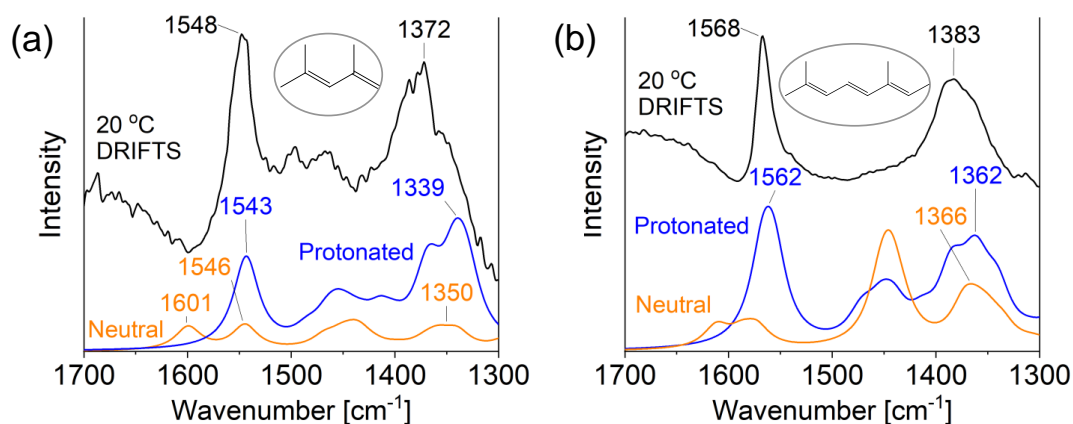


Figure 2.6 DRIFT spectra at 20 °C (black) for guest molecules (a) **I** and (b) **II** in HMOR zeolite. Shown for comparison are zeolite-adsorbed, computed spectra using full optimization of neutral (orange) and protonated (blue) forms of each molecule.

To determine the atomic-level nature of the adsorbed states of olefins **I** and **II** in HMOR, we show in Figs. 2.6a and 2.6b, respectively, the computed IR spectra from

periodic DFT using the full optimization method. For each zeolite-guest system, we show IR spectra computed from a neutral olefin hydrogen-bonded to the Brønsted acid site (in orange), and from a protonated olefin ($\mathbf{I}^+/\mathbf{II}^+$) interacting electrostatically with the zeolite conjugate base (in blue). The protonated forms \mathbf{I}^+ and \mathbf{II}^+ were obtained by manually protonating the neutral counterparts at the lowest energy protonation site determined by gas-phase electronic structure calculations (see Fig. 2.11 and Table 2.4 in Appendix). The calculated Gibbs energies of the various protonated forms indicate that protonation is preferred at the carbon that produces a conjugated allylic cation system that is fully alkyl substituted at the terminal carbons. As with Sec. 2.3.1, we considered the various conformations for molecule \mathbf{II}^+ . (Note that molecule \mathbf{I}^+ exhibits only a single conformation because of the symmetry conferred by protonation.) For molecule \mathbf{II}^+ , however, we considered a total of eight possible conformers (see Table 2.5 in Appendix) and found that the all-trans conformer is strongly energetically favored. Thus, in this case, considering the spectrum for only the all-trans conformer is sufficient. Qualitatively comparing the experimental and computed spectra in Fig. 2.6a strongly suggests that olefin **I** is protonated in HMOR; the same conclusion can be drawn for olefin **II** from the data in Fig. 2.6b. In particular, both computed IR spectra for the protonated olefins in Figs. 2.6a and 2.6b show the strong band in the 1500–1600 cm^{-1} region and the broader band in the 1300–1400 cm^{-1} region. In contrast, the computed IR spectra for the neutral olefins in HMOR retain the bands around 1600 cm^{-1} , corresponding to C=C stretching vibrations, which were also seen in the spectra in Sec. 2.3.1 (Fig. 2.5). Also, in contrast to the IR spectrum of **I** in all-silica MOR, the bands in HMOR are red-shifted (and double

bonds lengthened by about 0.05 Å compared to gas-phase values) because of hydrogen bonding with the Brønsted acid site.

Quantitative comparisons between theory and experiment in Figs. 2.6a and 2.6b also support the notion of protonated olefins in HMOR. The strong singlet bands from computed spectra in Figs. 2.6a and 2.6b are seen at 1543 cm⁻¹ (**I**⁺) and 1562 cm⁻¹ (**II**⁺), respectively, which compare well with experimental values of 1548 cm⁻¹ and 1568 cm⁻¹, indicating that our fully-optimized periodic DFT approach has captured the blue shift in the IR spectrum from **I**⁺ to **II**⁺. Visual inspection³⁴ of normal modes for these vibrations do indeed indicate motions of allylic cations (C=C-C⁺),^{32,33} as shown in Fig. 2.7 for species **I**⁺. We were curious whether the small, systematic error of 5–6 cm⁻¹ could be attributed to finite temperature effects. To address this, we employed the ensemble averaging model and found that thermal fluctuations of the zeolite at experimental temperatures of 20, 130, and 200 °C do not significantly impact the spectrum in the key spectral region of 1300–1700 cm⁻¹ (see Fig. 2.12 in Appendix). Furthermore, we found that the spread of spectra in the ensembles at 20 and 200 °C were nearly identical (Fig. 2.13 in Appendix). Finally, we note that our computed bands for methyl deformations at 1339 and 1362 cm⁻¹ for molecule **I**⁺ and **II**⁺, respectively, show very good qualitative agreement in band shapes with experimental DRIFTS data, though the computed band locations are red-shifted compared to experiment. Thus, the spectra in Figs. 2.6a and 2.6b suggest that fully-optimized periodic DFT within the harmonic approximation captures the key features of the IR spectra at 20 °C, and that both olefins in HMOR exhibit spectral bands consistent with protonated states.

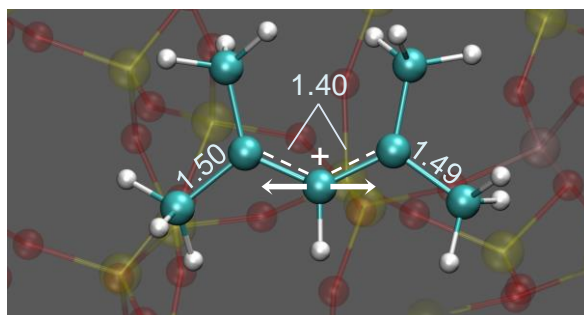


Figure 2.7 Illustration of I⁺ adsorbed over HMOR zeolite. Fully optimized geometry is shown with equilibrium bond distances [Å]. White arrow designates the vibrational motion associated with the 1543 cm⁻¹ peak in the computed spectrum.

As a final test of this idea, we evaluated the Helmholtz free energies of protonation for **I** and **II** in HMOR within the multidimensional harmonic oscillator model using the formula shown in Section 2.5.2 in the Appendix. We found Helmholtz free energies of protonation of -18.0 and -27.3 kcal/mol for **I** and **II**, respectively, further supporting the IR spectroscopy findings of protonation in HMOR 20 °C. The definitive computational test would be to find relatively low protonation barriers, allowing facile protonation at 20 °C. We leave this for future work. We nonetheless conclude from the thermodynamics and spectroscopy findings described herein that olefins **I** and **II** become protonated in HMOR at 20 °C, representing an example of strong zeolite-guest interaction.

2.3.3 Adsorbed Protonated Olefins on HMOR: Nature of Electrostatic Interactions

We found above that the adsorption of acyclic olefins **I** and **II** on HMOR results in significant changes to the IR spectra in the 1300–1700 cm⁻¹ region, attributed to protonation from Brønsted acid sites in HMOR. Such protonation leaves behind an ion-

pair interaction between the protonated olefin and the conjugate base of the acidic zeolite. It is interesting to determine how this ion-pair electrostatic interaction may influence the IR spectra of the zeolite-guest systems.

Figure 2.8 addresses this question by comparing the computed spectra of protonated molecules **I**⁺ (Fig. 2.8a) and **II**⁺ (Fig. 2.8b) in the gas phase (red) and in MOR⁻ (blue). We applied the same level of theory (BLYP) and basis set (triple- ζ valence polarized) in gas-phase and zeolite-adsorbed calculations to produce appropriate comparisons. We found the remarkable and perhaps surprising result for cation **I**⁺ in Fig. 2.8a that the zeolite-adsorbed cation and gas-phase cation exhibit essentially the same IR spectra in the key 1300–1700 cm⁻¹ region, with only tiny shifts within the margin of error of the DFT method and largely minor variations in the intensity distribution. Figure 2.8b shows the same surprising result for cation **II**⁺. In the case of **I**⁺, a singlet is seen at 1541 cm⁻¹ in the gas-phase spectrum, which is within a few wavenumbers from the zeolite-adsorbed band. Similarly, the gas-phase singlet for **II**⁺ at 1570 cm⁻¹ is only 8 cm⁻¹ from the zeolite-adsorbed band. Furthermore, inspection of the relevant normal modes for **I**⁺ and **II**⁺ revealed that the vibration corresponding to these singlets is identical in the gas phase and the zeolite, namely, the allylic stretching mentioned in the previous section (see Fig. 2.7). A structural analysis demonstrates that the intramolecular configurations of **I**⁺ and **II**⁺ are essentially unchanged upon adsorption, as highlighted in Fig. 2.14 in the Appendix for molecule **II**⁺. Thus, despite the presence of an electrostatic ion-pair interaction between the protonated olefins and the negatively-charged zeolite conjugate base, the structures and IR spectra of these olefins appear unaffected by the zeolite. In other words, our results suggest the finding that, in order to model the spectral

fingerprints in the 1300–1700 cm^{-1} region of acyclic olefins over acidic zeolites with a margin of error of 10 cm^{-1} , one only needs to consider the protonated species in the gas phase.

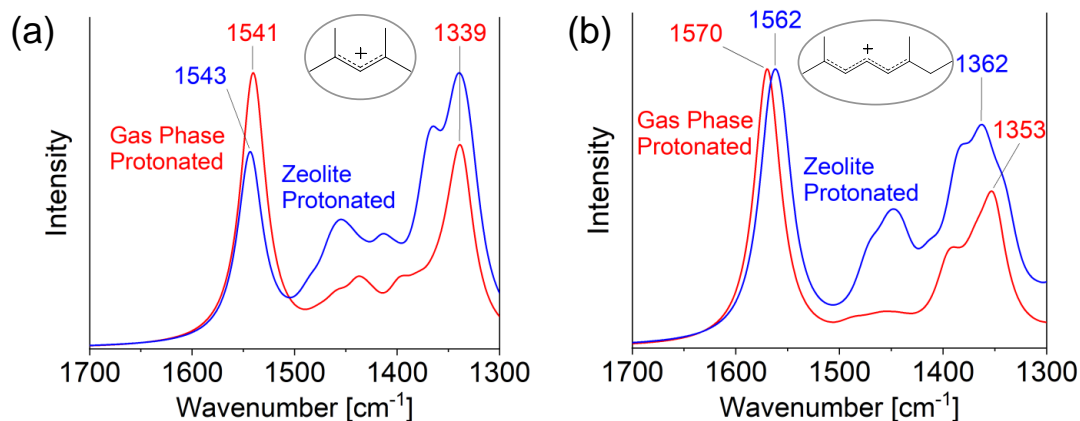
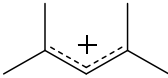
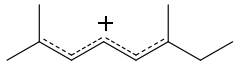


Figure 2.8 Comparison of computed gas-phase (red) and zeolite-adsorbed (blue) spectra for molecules (a) I^+ and (b) II^+ .

Table 2.2 presents a summary of the aforementioned computed frequencies of protonated olefins I^+ and II^+ alongside experimental values for comparison. We note two important findings from these comparisons. The first finding pertains to the systematic red-shifting of computational bands relative to experimental ones, consistent with results in Fig. 2.4 and Table 2.1. Combining data in Tables 2.1 and 2.2 reveals the second and more remarkable finding – that including the zeolite framework when computing the IR spectrum may not significantly increase the agreement between theory and experiment. We examined this by computing absolute differences between experiment and each of the models in both Tables 2.1 and 2.2, and then constructing root-mean-square (RMS) differences considering all vibrations in the Tables. This yields RMS differences of 25.8, 27.4, and 31.1 cm^{-1} for CP2K Vacuum, CP2K MOR adsorbed, and Gaussian gas phase, respectively. We conclude then, that for these acyclic olefins adsorbed on acidic and non-

acidic zeolites, modeling the regions of the IR spectrum studied in our work can be accomplished by simply treating the molecule in the gas phase.

Table 2.2 Summary of computed frequencies (cm^{-1}) for protonated olefins **I**+ and **II**+ in the gas phase and inside HMOR zeolite. Experimental DRIFTS frequencies are shown for comparison for the olefins adsorbed on HMOR

Molecule	Molecular Vibration	DRIFTS	CP2K	Gaussian
			HMOR	Gas
	$\nu(\text{C}-\text{C}=\text{C}^+)$ $\delta_{\text{sym}}(\text{CH}_3)$	1548 1372	1543 1339	1541 1339
	$\nu(\text{C}-\text{C}=\text{C}^+)$ $\delta_{\text{sym}}(\text{CH}_3)$	1568 1383	1562 1362	1570 1353

2.4 Conclusions

We have performed periodic DFT calculations on acyclic olefins in acidic HMOR zeolite and non-acidic porous silica to investigate the nature of adsorbed species and the influence of host-guest interaction on the IR spectra. In this regard, we made direct comparisons with experimental IR measurements conducted by Dr. Eric Hernandez and Prof. Friederike Jentoft. In particular, we have studied the acyclic olefins 2,4-dimethyl-1,3-pentadiene (**I**) and 2,6-dimethyl-2,4,6-octatriene (**II**) because of their importance in the field of methanol conversion, as precursors to cyclic intermediates that (i) are active in the catalytic cycle and (ii) can lead to deactivating species known as “coke.” We found that a 1x1x2 super cell of HMOR was necessary to avoid spurious interactions between guests in neighboring periodic images. A BLYP functional with a triple- ζ valence polarized basis set was used within the CP2K software. For the computation of zeolite-adsorbed IR spectra we employed two techniques within the harmonic approximation: (1) full optimization followed by normal mode analysis (NMA); and (2) an ensemble

averaging scheme that takes into account thermal fluctuations of the zeolite. We used these models to compare with diffuse reflectance Fourier transform (DRIFT) spectra to investigate the impact on IR spectra of host-guest interactions and the state of the adsorbed acyclic olefin.

We employed DFT-based thermodynamics calculations and found the surprising result that, for olefin **I** adsorbed over all-silica, large-pore zeolites, a gauche s-cis conformer is slightly preferred over its s-trans counterpart. We found that this slight preference towards the gauche s-cis conformer was reflected in the experimental IR spectrum, which was accurately represented by using a Boltzmann weighted sum of the computed spectra of each conformer. Next, we found that introducing olefins **I** and **II** into the acidic zeolite HMOR produced substantial changes to the IR spectra, showing the signature of protonated species such as a strong singlet in the 1500–1600 cm^{-1} region typically assigned to stretching of allylic cations, $\nu(\text{C}=\text{C}-\text{C}^+)$. Periodic DFT using the full optimization model on protonated guests (**I**⁺ and **II**⁺) was found to accurately represent the DRIFT spectra in HMOR at 20 °C. The computed IR spectra were essentially unchanged from including zeolite atoms in the NMA, and from including thermal fluctuations of the zeolite, suggesting that system optimization and guest NMA are sufficient to capture IR spectra of acyclic olefins in acidic zeolites. Thermodynamics calculations based on the periodic DFT results are consistent with the stability of protonation of olefins **I** and **II** in zeolite HMOR.

To determine the influence of electrostatic interactions between cationic guests (**I**⁺ and **II**⁺) and negatively-charged zeolites, we compared IR spectra computed for zeolite-adsorbed and gas-phase cations, finding virtually no difference in the spectra in the 1300–

1700 cm^{-1} region. Structural analyses of bond lengths and dihedral angles of zeolite-adsorbed and gas-phase alkenyl and alkadienyl cations support the notion that ion-pair electrostatic interactions have negligible effect on these cations in zeolites. An analysis of the discrepancies between experimental IR frequencies for various vibrational modes and those from our models suggests the surprising finding that gas-phase models of zeolite adsorption are both the most efficient and in certain instances, such as for allylic stretching modes, just as accurate as zeolite-adsorbed models as long as the relevant state of the guest is taken into account.

2.5 Appendix – Supporting Information

2.5.1 Inclusion of zeolite framework for normal mode analysis

All computed zeolite-adsorbed spectra involved a normal mode analysis (NMA) performed on a zeolite+guest system. For these calculations, we only included the guest atoms in the NMA and left out all zeolite atoms. To test the impact of leaving out atoms we ran test calculations where we included zeolite atoms within a radius $\delta[\text{\AA}]$ from the guest atom up until inclusion of the entire zeolite. Figure 2.9 shows the findings from these calculations in which we showed that in the region of interest 1300–1700 cm^{-1} there was no impact on the spectra from leaving zeolite atoms out.

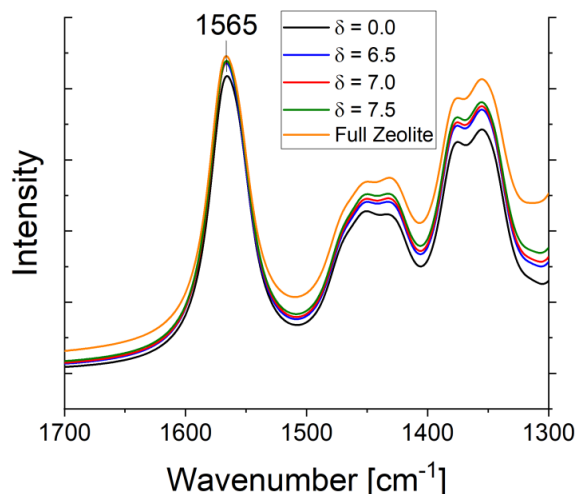


Figure 2.9 Systematic inclusion of zeolite framework atoms for normal mode analysis calculation and spectra generation (molecule II⁺). No change seen in spectra in 1300-1700 cm⁻¹ region even when all zeolite atoms are included in the calculation.

2.5.2 Thermodynamics of periodic DFT systems

The free energies of the zeolite-guest systems and isolated neutral guest were studied by employing a multidimensional harmonic oscillator model (Equation below).

$$\text{Helmholtz Free Energy} = U + \sum_{N=1}^{\# \text{ of modes}} \frac{\hbar\omega_N}{2} + \sum_{N=1}^{\# \text{ of modes}} \ln \left(1 - e^{-\frac{\hbar\omega_N}{k_B T}} \right)$$

2.5.3 Free energy profiles for rotational conformers of olefin I

Olefin I can exist in two rotational conformers; gauche s-cis and s-trans. We computed free energy profiles of rotation over non-acidic MOR and in vacuum. The free energies of rotation as well as the corresponding activation free energies are reported in Table 2.3. We also utilized the Gaussian 09 software to obtain the Gibbs free energy profiles using more accurate model chemistries to ensure the trend we found using CP2K

and the BLYP/TZVP model chemistry was valid. We show the higher accuracy energies alongside the CP2K values in Table 2.3.

Table 2.3 Computed free energy profiles for rotation between gauche s-cis and s-trans conformers of I. Higher accuracy model chemistries show similar trend of lower energy gauche s-cis conformer.

	Gas Phase (Gaussian)			CP2K	
	BLYP	B3LYP	MP2	Isolated (Vacuum)	MOR-ads
s-cis	0.0	0.0	0.0	0.0	0.0
TS	2.63	2.58	2.94	1.46	3.85
s-trans	0.19	0.43	1.69	0.26	0.27

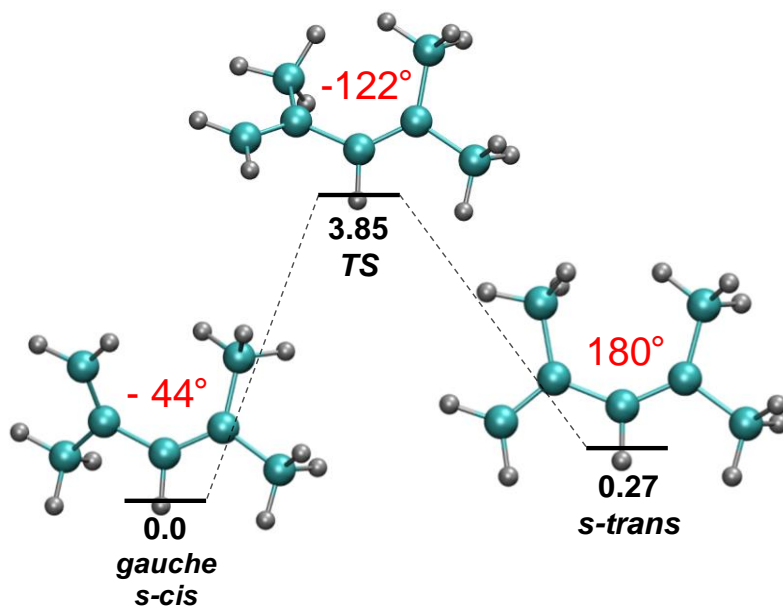


Figure 2.10 Helmholtz energy profile for rotation of olefin I between gauche s-cis and s-trans states. Energies computed using model described in Section 2.5.2. Molecules pictured are fully geometry optimized structures. Dihedral angles are reported in red.

2.5.4 Thermodynamics of protonation for olefins I and II

For isolated protonated molecules, we employed electronic structure calculations, namely geometry optimizations and NMA, to obtain Gibbs free energies using the Gaussian 09²¹ software. In order to consider protonation of molecules **I** and **II** we manually protonated the molecules at the available protonation sites (Figure 2.11) and determined the lowest energy site to be used to produce the protonated molecules **I**⁺ and **II**⁺. The relative energies for protonation sites are reported in Table 2.4.

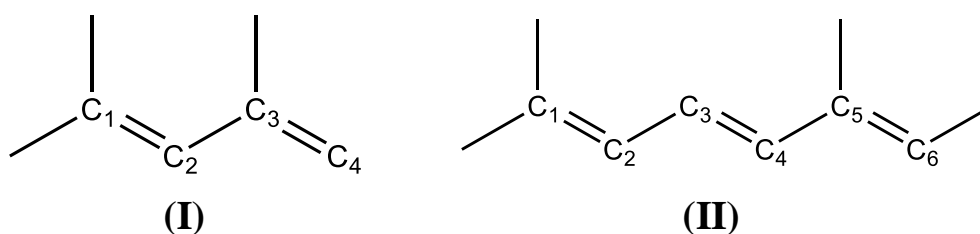


Figure 2.11 Possible protonation sites shown for molecules I and II. All possible sites were protonated manually and a Gibbs free energy was calculated to determine the lowest energy site.

Table 2.4 Various protonation sites for molecules I and II along with corresponding Gibbs Free Energies at 293K. Energies reported relative to lowest energy site.

Molecule	Protonation Site	Gibbs Free Energy [kcal/mol]*
I	C1	24.1
	C2	22.6
	C3	-
	C4	0.0
II	C1	9.09
	C2	31.1
	C3	19.5
	C4	17.1
	C5	16.6
	C6	0.0

*Non-reported values are due to structures not being stable enough to optimize

2.5.5 Conformational analysis for olefin II⁺

We also conducted a conformation analysis on the protonated form of olefin **II**. We found that in this case the all trans molecule was significantly lower in free energy than any other conformer. The molecule **II**⁺ has 4 bonds in the allylic system which can be rotated along. Rotation along the first bond does not result in a new conformer which leaves 3 bonds, giving rise to 8 different conformers. The relative energies between all 8 conformers are reported in Table 2.5. The labeling of the conformers using “T” to describe a trans orientation along the bond while the “C” denotes cis.

Table 2.5 Computed free energies for the 8 conformers of protonated olefin **II**⁺. Energies are shown relative to the low energy all trans conformer (TTTT).

Conformation	Free Energy [kcal/mol]
TTTT	0
TCTT	13.5
TTCT	9.16
TTTC	4.46
TCCT	15.5
TTCC	6.54
TCTC	9.92
TCCC	16.6

2.5.6 Impact of thermal fluctuations through ensemble average technique

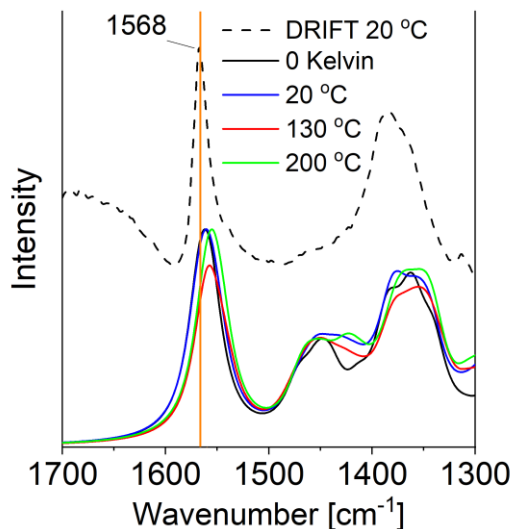


Figure 2.12 Comparison of spectra obtained using ensemble averaging technique at 20, 130, and 200 °C to full optimization model (0 Kelvin). Experimental DRIFT spectrum at 20 °C is also shown for comparison. All spectra are for protonated octatriene in HMOR.

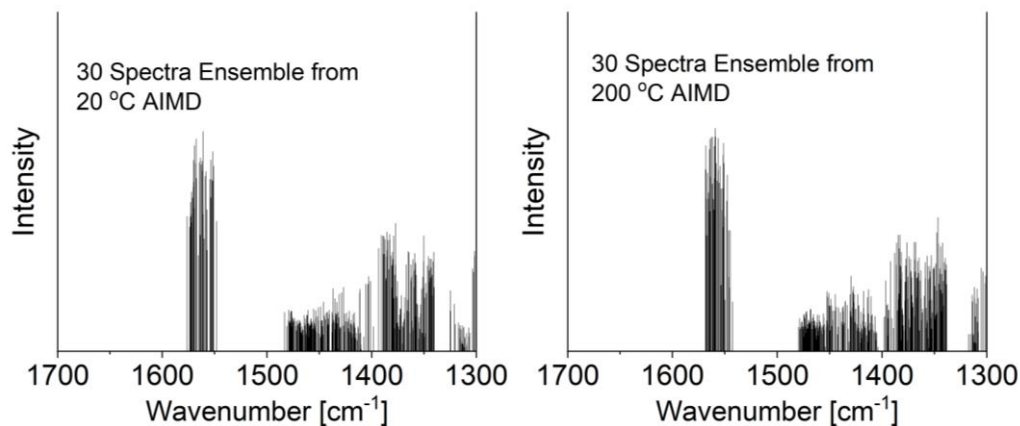


Figure 2.13 Stick spectra of 30 images extracted from AIMD at 20 °C (left) and 200 °C (right).

2.5.7 Intramolecular distances and angles between gas-phase and zeolite-adsorbed II^+

We studied the interaction between a positively charged guest molecule and a negatively charged zeolite framework by considering the impact on the molecular geometry. Figure 2.14 shows a comparison of intramolecular bond distances and torsional angles for molecule II^+ in the gas phase and adsorbed over MOR. We found that

the interaction was very minimal leading to nearly identical molecular geometries in both environments.

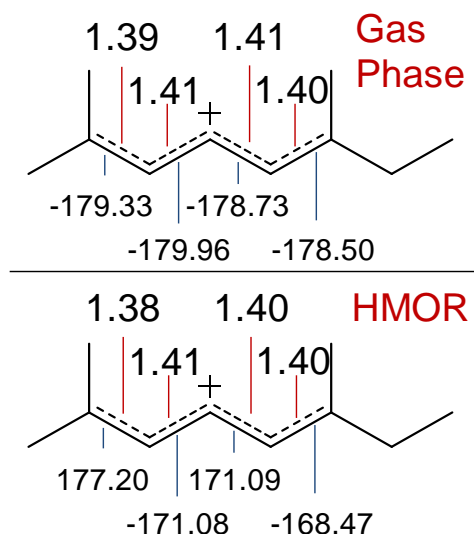


Figure 2.14 Comparison of relevant intramolecular bond distances and dihedrals for II^+ in the gas phase (top) and over HMOR (bottom). The bond distances of the allylic system are nearly identical in the two environments while the dihedrals exhibit subtle deviations of up to 10° .

2.6 References

- (1) Dahl, I. M.; Kolboe, S. On the Reaction Mechanism for Propene Formation in the MTO Reaction over SAPO-34. *Catal. Letters* **1993**, *20* (3), 329–336. <https://doi.org/10.1007/BF00769305>.
- (2) Yarulina, I.; Chowdhury, A. D.; Meirer, F.; Weckhuysen, B. M.; Gascon, J. Recent Trends and Fundamental Insights in the Methanol-to-Hydrocarbons Process. *Nat. Catal.* **2018**, *1* (6), 398–411. <https://doi.org/10.1038/s41929-018-0078-5>.
- (3) Wulfers, M. J.; Jentoft, F. C. The Role of Cyclopentadienium Ions in Methanol-to-Hydrocarbons Chemistry. *ACS Catal.* **2014**, *4* (10), 3521–3532. <https://doi.org/10.1021/cs500722m>.
- (4) Goetze, J.; Weckhuysen, B. M. Spatiotemporal Coke Formation over Zeolite ZSM-5 during the Methanol-to-Olefins Process as Studied with Operando UV-Vis Spectroscopy: A Comparison between H-ZSM-5 and Mg-ZSM-5. *Catal. Sci. Technol.* **2018**, *8* (6), 1632–1644. <https://doi.org/10.1039/C7CY02459B>.
- (5) Borodina, E.; Sharbini Harun Kamaluddin, H.; Meirer, F.; Mokhtar, M.; Asiri, A. M.; Al-Thabaiti, S. A.; Basahel, S. N.; Ruiz-Martinez, J.; Weckhuysen, B. M. Influence of the Reaction Temperature on the Nature of the Active and Deactivating Species During Methanol-to-Olefins Conversion over H-SAPO-34. *ACS Catal.* **2017**, *7* (8), 5268–5281. <https://doi.org/10.1021/acscatal.7b01497>.
- (6) Osuga, R.; Yokoi, T.; Kondo, J. N. IR Observation of Activated Ether Species on Acidic OH Groups on H-ZSM-5 Zeolites. *Mol. Catal.* **2019**, *477*, 110535. <https://doi.org/10.1016/j.mcat.2019.110535>.

- (7) Joshi, Y. V.; Thomson, K. T. Embedded Cluster (QM/MM) Investigation of C6 Diene Cyclization in HZSM-5. *J. Catal.* **2005**, *230* (2), 440–463. <https://doi.org/https://doi.org/10.1016/j.jcat.2004.12.016>.
- (8) Manookian, B.; Hernandez, E. D.; Baer, M. D.; Mundy, C. J.; Jentoft, F. C.; Auerbach, S. M. Experimental and DFT Calculated IR Spectra of Guests in Zeolites: Acyclic Olefins and Host–Guest Interactions. *J. Phys. Chem. C* **2020**, *124* (19), 10561–10572. <https://doi.org/10.1021/acs.jpcc.0c01225>.
- (9) Baerlocher, C.; McCusker, L. B. International Zeolite Association: Database of Zeolite Structures.
- (10) Meier, W. M. The Crystal Structure of Mordenite (Ptilolite)*. *Zeitschrift für Krist.* **1961**, *115* (5–6), 439–450. <https://doi.org/10.1524/zkri.1961.115.5-6.439>.
- (11) Demuth, T.; Hafner, J.; Benco, L.; Toulhoat, H. Structural and Acidic Properties of Mordenite. An Ab Initio Density-Functional Study. *J. Phys. Chem. B* **2000**, *104* (19), 4593–4607. <https://doi.org/10.1021/jp993843p>.
- (12) Guo, H.; Ren, J.; Feng, G.; Li, C.; Peng, X.; Cao, D. Distribution of Al and Adsorption of NH₃ in Mordenite: A Computational Study. *J. Fuel Chem. Technol.* **2014**, *42* (5), 582–590. [https://doi.org/https://doi.org/10.1016/S1872-5813\(14\)60028-1](https://doi.org/https://doi.org/10.1016/S1872-5813(14)60028-1).
- (13) Rasmussen, D. B.; Christensen, J. M.; Temel, B.; Studt, F.; Moses, P. G.; Rossmeisl, J.; Riisager, A.; Jensen, A. D. Reaction Mechanism of Dimethyl Ether Carbonylation to Methyl Acetate over Mordenite – a Combined DFT/Experimental Study. *Catal. Sci. Technol.* **2017**, *7* (5), 1141–1152. <https://doi.org/10.1039/C6CY01904H>.
- (14) Alberti, A.; Davoli, P.; Vezzalini, G. The Crystal Structure Refinement of a Natural Mordenite. *Zeitschrift für Krist.* **1986**, *175*, 249–256.
- (15) VandeVondele, J.; Krack, M.; Mohamed, F.; Parrinello, M.; Chassaing, T.; Hutter, J. QUICKSTEP: Fast and Accurate Density Functional Calculations Using a Mixed Gaussian and Plane Waves Approach. *Comput. Phys. Commun.* **2005**, *167* (2), 103–128.
- (16) Mathias, G.; Baer, M. D. Generalized Normal Coordinates for the Vibrational Analysis of Molecular Dynamics Simulations. *J. Chem. Theory Comput.* **2011**, *7* (7), 2028–2039. <https://doi.org/10.1021/ct2001304>.
- (17) Buczek, A.; Kupka, T.; Broda, M. A.; Żyła, A. Predicting the Structure and Vibrational Frequencies of Ethylene Using Harmonic and Anharmonic Approaches at the Kohn-Sham Complete Basis Set Limit. *J. Mol. Model.* **2016**, *22* (1), 42. <https://doi.org/10.1007/s00894-015-2902-z>.
- (18) Grimme, S.; Antony, J.; Ehrlich, S.; Krieg, H. A Consistent and Accurate Ab Initio Parametrization of Density Functional Dispersion Correction (DFT-D) for the 94 Elements H–Pu. *J. Chem. Phys.* **2010**, *132* (15), 154104. <https://doi.org/10.1063/1.3382344>.
- (19) Goedecker, S.; Teter, M.; Hutter, J. Separable Dual-Space Gaussian Pseudopotentials. *Phys. Rev. B* **1996**, *54* (3), 1703–1710. <https://doi.org/10.1103/PhysRevB.54.1703>.
- (20) VandeVondele, J.; Hutter, J. Gaussian Basis Sets for Accurate Calculations on Molecular Systems in Gas and Condensed Phases. *J. Chem. Phys.* **2007**, *127* (11), 114105. <https://doi.org/10.1063/1.2770708>.
- (21) Frisch, M. J.; Trucks, G. W.; Schlegel, H. B.; Scuseria, G. E.; Robb, M. A.; Cheeseman, J. R.; Scalmani, G.; Barone, V.; Mennucci, B.; Petersson, G. A.; et al. Gaussian 09, Revision B.01; Gaussian Inc.: Wallingford, CT, 2009.
- (22) *NIST Computational Chemistry Comparison and Benchmark Database*, Release 20.; Johnson III, R. D., Ed.; 2019.
- (23) Agarwal, V.; Huber, G. W.; Conner, W. C.; Auerbach, S. M. Simulating Infrared Spectra and Hydrogen Bonding in Cellulose I β at Elevated Temperatures. *J. Chem. Phys.* **2011**, *135* (13), 134506. <https://doi.org/10.1063/1.3646306>.
- (24) Wang, T.; Luo, S.; Tompsett, G. A.; Timko, M. T.; Fan, W.; Auerbach, S. M. Critical Role of Tricyclic Bridges Including Neighboring Rings for Understanding Raman Spectra of Zeolites. *J. Am. Chem. Soc.* **2019**, *141* (51), 20318–20324. <https://doi.org/10.1021/jacs.9b10346>.
- (25) Squillacote, M. E.; Liang, F. Conformational Thermodynamic and Kinetic Parameters of Methyl-Substituted 1,3-Butadienes. *J. Org. Chem.* **2005**, *70* (17), 6564–6573. <https://doi.org/10.1021/jo0500277>.
- (26) Sun, Y.; Zhou, C.-W.; Somers, K. P.; Curran, H. J. Ab Initio/Transition-State Theory Study of the Reactions of C₅H₉ Species of Relevance to 1,3-Pentadiene, Part I: Potential Energy Surfaces,

- Thermochemistry, and High-Pressure Limiting Rate Constants. *J. Phys. Chem. A* **2019**, *123* (42), 9019–9052. <https://doi.org/10.1021/acs.jpca.9b06628>.
- (27) Rauhut, G.; Pulay, P. Transferable Scaling Factors for Density Functional Derived Vibrational Force Fields. *J. Phys. Chem.* **1995**, *99* (10), 3093–3100. <https://doi.org/10.1021/j100010a019>.
- (28) Tyrode, E.; Rutland, M. W.; Bain, C. D. Adsorption of CTAB on Hydrophilic Silica Studied by Linear and Nonlinear Optical Spectroscopy. *J. Am. Chem. Soc.* **2008**, *130* (51), 17434–17445. <https://doi.org/10.1021/ja805169z>.
- (29) Premadasa, U. I.; Moradighadi, N.; Kotturi, K.; Nonkumwong, J.; Khan, M. R.; Singer, M.; Masson, E.; Cimatu, K. L. A. Solvent Isotopic Effects on a Surfactant Headgroup at the Air–Liquid Interface. *J. Phys. Chem. C* **2018**, *122* (28), 16079–16085. <https://doi.org/10.1021/acs.jpcc.8b03680>.
- (30) Fang, H.; Zheng, A.; Xu, J.; Li, S.; Chu, Y.; Chen, L.; Deng, F. Theoretical Investigation of the Effects of the Zeolite Framework on the Stability of Carbenium Ions. *J. Phys. Chem. C* **2011**, *115* (15), 7429–7439. <https://doi.org/10.1021/jp1097316>.
- (31) Lin-Vien, D.; Colthup, N. B.; Fateley, W. G.; Grasselli, J. G. The Handbook of Infrared and Raman Characteristic Frequencies of Organic Molecules: Chapter 2 - Alkanes; Lin-Vien, D., Colthup, N. B., Fateley, W. G., Grasselli, J. G. B. T.-T. H. of I. and R. C. F. of O. M., Eds.; Academic Press: San Diego, 1991; pp 9–28. <https://doi.org/https://doi.org/10.1016/B978-0-08-057116-4.50008-0>.
- (32) Adam, W.; Casades, I.; Fornés, V.; García, H.; Weichold, O. UV–vis and IR Spectral Characterization of Persistent Carbenium Ions, Generated upon Incorporation of Cinnamyl Alcohols in the Acid Zeolites HZSM-5 and HMor. *J. Org. Chem.* **2000**, *65* (13), 3947–3951. <https://doi.org/10.1021/jo991801r>.
- (33) Cano, M. L.; Fornés, V.; García, H.; Miranda, M. A.; Pérez-Prieto, J. Characterization of Persistent α,ω -Diphenyl Substituted Allyl Cations within Monodirectional Acid Zeolites. *J. Chem. Soc. Chem. Commun.* **1995**, No. 24, 2477–2478. <https://doi.org/10.1039/C39950002477>.
- (34) Humphrey, W.; Dalke, A.; Schulten, K. VMD: Visual Molecular Dynamics. *J. Mol. Graph.* **1996**, *14* (1), 33–38. [https://doi.org/https://doi.org/10.1016/0263-7855\(96\)00018-5](https://doi.org/https://doi.org/10.1016/0263-7855(96)00018-5).

CHAPTER 3

INVESTIGATING THE EXTENT OF SHAPE-SELECTIVITY IN MEDIUM AND LARGE PORE ZEOLITES DURING ALKYL CYCLOPENTENYL CATION FORMATION

3.1 Introduction

In Chapter 2 we conducted a spectroscopic benchmarking study with two goals in mind: (1) to benchmark our computational spectroscopy techniques in collaboration with experimental work and (2) to determine the nature of zeolite-guest interaction and its manifestation in IR spectra. We found, somewhat surprisingly, that Coulombic interaction between acyclic olefins and zeolite framework had minimal impact on allylic stretching bands. This finding allows us to utilize gas-phase computed IR spectra as a baseline for elucidating experimental spectra associated with similar cationic species. In this chapter, we extend the study to cyclic species, namely alkyl-substituted cyclopentenyl cations formed from acyclic precursors. Specifically, we aim to determine the nature of host-guest interaction between large and medium pore zeolites and cyclopentenyl cations, by performing DFT calculations for comparison with corresponding experimental IR spectra. The results and conclusions in this chapter stem from collaborative work. The design and execution of the experiments, data collection and analysis, and interpretation in context with the literature in this chapter are credited to Dr. Eric Hernandez of Prof. Friederike Jentoft's research group of in the Department of Chemical Engineering at University of Massachusetts Amherst. Figures are included with permission. We show that experimental and computational evidence corroborates significant host-guest interaction leading to shape-selectivity in the formation of alkyl-

substituted cyclopentenyl cations, with specific focus on allylic substitution patterns. Moreover, we find that thermodynamic favorability of these cyclopentenyl cations is independent of zeolite framework.

Zeolite-catalyzed methanol-to-olefin (MTO) reactions yield alkyl-substituted cyclopentenyl cations during the generation of value-added olefinic products. These cyclopentenyl cations can act as active co-catalysts, but also precede reactions that lead to larger polycyclic species that can ultimately deactivate the catalyst¹⁻³. Previous work has highlighted the presence of these cyclopentenyl cations in zeolites, their formation from acyclic precursors, and the influence of zeolite pore structure on substitution patterns using various spectroscopic techniques.³⁻⁶ With that, the understanding of the characteristic $\nu_{as}(\text{C}=\text{C}-\text{C}^+)$ vibration associated with these cations is rather limited in the literature. Moreover, although computational methods have been used to simulate IR⁷ and UV-vis spectra⁸ of similar cationic species in zeolites, cyclopentenyl cations have only been considered in the gas phase.⁹ We aim to conduct a collaborative investigation using experimental and computational techniques of cyclopentenyl cation substitution patterns to provide key insight into shape-selective control of formation as well as corresponding IR signatures.

The substitution pattern on the allylic system of these polyalkylated cations remains a poorly understood aspect of their constitution within zeolitic frameworks. In the work outlined below, we focus on two major types of polyalkylated cations which differ by substitution of the central C-2 carbon (Figure 3.1), with either a hydrogen (cation **I**) or a methyl group (cation **II**). While these two types of alkyl-substituted cyclopentenyl cations have been experimentally distinguished in liquid acid by ¹H NMR,

^{13}C NMR, and UV–vis spectroscopy,^{10–12} in many reports the substitution of the C-2 ring carbon is not explicitly defined. Interestingly, zeolite structure may dictate whether cation type **I** or cation type **II** is present.

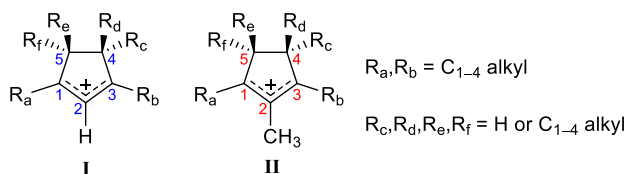


Figure 3.1 General structures of alkylcyclopentenyl cation isomers with ring numbering system as indicated. (Reproduced with permission from Hernandez, E. D.; Manookian, B.; Auerbach, S. M.; Jentoft, F. C. Shape-Selective Synthesis of Alkylcyclopentenyl Cations in Zeolites and Spectroscopic Distinction of Constitutional Isomers. *ACS Catal.* 2021, *11* (21), 12893–12914. Copyright 2021 American Chemical Society.)

In the following study we employ periodic DFT calculations and compare with experimental data obtained by Dr. Hernandez and Prof. Jentoft to investigate the nature of shape-selectivity in the formation of cyclopentenyl cations and the thermodynamics associated with these types of molecular transformations. We highlight the formation of specifically substituted cyclopentenyl cations in varying zeolite frameworks and the sensitivity of thermodynamic favorability on zeolite pore confinement. The material below has been previously published in *ACS Catalysis*.¹³

3.2 Methods

3.2.1 Experimental Methods

For a detailed description of the experimental methods, we refer the reader to our article in *ACS Catalysis*.¹³

3.2.2 Computational Methods

3.2.2.1 Zeolite Models

Zeolite unit cells were obtained from the Structure Commission of the International Zeolite Association.^{14,15} Previously optimized unit cell parameters for H-MOR,¹⁶ H-ZSM-5,¹⁷ and H-ZSM-22¹⁸ were used for all periodic DFT calculations. To avoid interaction of guest molecules in adjacent cells, the unit cells of MOR and ZSM-22 were expanded in the *c*-direction, creating $1 \times 1 \times 2$ and $1 \times 1 \times 3$ supercells, respectively. One acid site was introduced into each of the zeolite unit cells by substituting one Al atom into a framework tetrahedral site, which was balanced by a proton. For H-MOR, a single Al was substituted in at T4 (in accord with prior literature^{19–21}), creating a supercell composition of $\text{HAlSi}_9\text{O}_{192}$. The specific framework tetrahedral sites that Al occupies in H-ZSM-5 are unknown; however, the distribution of Al sites in H-ZSM-5 is considered to be nonrandom and kinetically controlled by synthesis conditions.²² An Al atom was substituted into the H-ZSM-5 framework at T12 (at the sinusoidal and straight channel intersection) based on previous studies that indicate high accessibility to bulky hydrocarbons.^{17,20,21,23} Also, we incorporated an Al substitution at the T6 site in the H-ZSM-5 to study confinement in the straight channel. The H-ZSM-5 unit cell composition was $\text{HAlSi}_9\text{O}_{192}$. For H-ZSM-22, a single Al atom was substituted into the super cell at T1, creating a super cell composition of $\text{HAlSi}_7\text{O}_{144}$. The T1 site was chosen because it is accessible, while the literature^{24–28} is inconclusive regarding placement of aluminum in TON.

3.2.2.2 Electronic Structure Calculations

CP2K software was used for periodic DFT calculations of zeolite–guest systems, allowing ab initio molecular dynamics, geometry optimizations, and normal mode analyses (NMA) with convenient visualization. Periodic DFT was used within the generalized gradient approximation with the PBE exchange–correlation functional as implemented in CP2K.²⁹ We applied PBE in CP2K to balance computational accuracy and efficiency, as determined by a gas-phase benchmarking exercise comparing BLYP, B3LYP, PBE, and MP2 levels of theory. In particular we computed ideal-gas Gibbs energies of acyclic and cyclic organic cations using the 6-311G(d) basis set within Gaussian 09.³⁰ These benchmark calculations demonstrate that the PBE functional principally reproduces the exergonicity (i.e., negative free-energy change) of cyclization as determined by the more reliable MP2, as well as the relative stabilities of the alkylcyclopentenyl cations considered.

Zeolite–guest systems studied with periodic DFT applied corrections by Grimme et al. (DFT-D3) to account for dispersion interactions between zeolite and guest species.³¹ For core electrons, Goedecker-Teter-Hutter norm-conserving pseudopotentials optimized for the PBE functional were used,³² while the valence electron wavefunctions are expanded in terms of a triple- ζ valence polarized basis set (TZVP).³³ Within the CP2K scheme, the electron density is described using an auxiliary plane-wave basis set with a 400 Ry cutoff.²⁹

3.2.2.3 Computed Infrared Spectra and Thermodynamics

To produce vibrational spectra of cations in the gas phase, a full geometry optimization for each cation was performed followed by NMA to obtain frequencies and

intensities. Likewise, spectra of cations in each zeolite were generated by conducting full geometry optimizations of the zeolite and guests followed by NMA.⁴ The resulting frequencies were scaled and incorporated into Lorentzian functions with a full width at half maximum (FWHM) of 15 cm⁻¹ to simulate IR spectra.^{4,34,35} Gas-phase spectra were calculated using BLYP/6-311G(d) and frequencies were scaled by 0.998,³⁶ whereas zeolite spectra were obtained using PBE/TZVP and frequencies were scaled by 0.990.³⁶ We used BLYP in the gas phase to maintain consistency with our previous work.⁴ To investigate the thermodynamic stabilities of various alkyl-substitution patterns on cyclopentenyl cations, relative Gibbs and Helmholtz energies were computed within the harmonic-oscillator approximation for gas-phase and zeolite-adsorbed systems, respectively. In all cases, we computed the free energy change upon cyclization, starting from the relevant acyclic conjugated cation as detailed further in Section 3.3.

The energetics of different rotational orientations of the cations in each zeolite and the resulting impact on computed spectra were studied by conducting a Boltzmann average. Starting from a local-minimum geometry, each alkylcyclopentenyl cation was rotated several times successively by 90° – first about the zeolite a-axis, then about the zeolite b-axis, and finally about the c-axis – to yield $i = 1, \dots, 10$ rather distinct initial conditions for local optimizations. NMA was performed for each local minimum, allowing the local Helmholtz energy $\{A_i\}$ and IR spectrum $\{I_i(\nu)\}$ to be computed. The total Helmholtz energy $\{A\}$ and IR spectrum $\{I(\nu)\}$ for each zeolite-guest system were determined by Boltzmann-averaging results from all orientational minima according to:

$$e^{-\beta A} = Q = \sum_{i=1}^{10} \Omega_i e^{-\beta E_i} = \sum_{i=1}^{10} e^{S_i/k_B} e^{-\beta E_i} = \sum_{i=1}^{10} e^{-\beta A_i} \quad \text{Eq. (3.1)}$$

$$I(v) = \sum_{i=1}^{10} e^{-\beta A_i} I_i(v)/Q \quad \text{Eq. (3.2)}$$

Here Q is the canonical partition function for a given zeolite-guest system; E_i and $S_i = k_B \ln(\Omega_i)$ are the thermal energy and entropy, respectively, for the i^{th} rotational minimum; k_B is Boltzmann's constant; and $\beta = 1/k_B T$ where T is absolute temperature. In most cases, the sums in Eqs. (3.1) and (3.2) are dominated by one or two terms, and in many cases, the dominant term(s) is not the initial local minimum considered.

3.3 Results

3.3.1 Cyclization of 2,6-Dimethyl-2,4,6-octatriene on H-Zeolites.

Our investigation of shape-selectivity in large and medium pore zeolites requires the use of alkatrienes as precursor molecules. Molecules of this type have been observed with ^1H NMR and UV-vis spectroscopy³⁷ to protonate and undergo subsequent cyclization to form alkyl-substituted cyclopentenyl cations in acidic media. Two types of alkyl-substituted cyclopentenyl cations (type **I** and type **II**) are formed via cyclization in strong liquid acid media.³⁷ The relative stabilities of these two types of cations have been reported such that type **II** cyclopentenyl cations are more stable than the type **I** counterpart, and at higher temperatures type **I** cations can isomerize to type **II**.³⁷ Figure 3.2 provides a hypothesized reaction route. We will investigate this reaction in medium and large pore zeolites and determine the presence of shape-selectivity during the formation of alkyl-substituted cyclopentenyl cation isomers. We explore this chemistry with collaboration of theoretical and experimental techniques as discussed in the sections

below. Experiments began by adsorption of a conjugated acyclic alkatriene into the zeolite pores at 20 °C, followed by increasing temperature to promote cyclization.

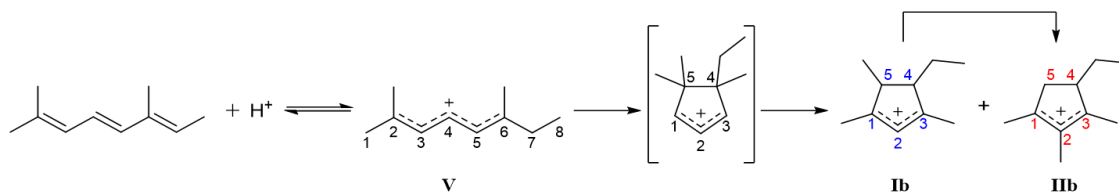


Figure 3.2 Cyclization of 2,6-dimethyl-2,4,6-octatriene to ethyltrimethylcyclopentenyl cation isomers in the presence of a Brønsted Acid. Numbers identify carbon atoms according to IUPAC nomenclature and change after cyclization. The ring is closed at the C-2 and C-6 carbons of the acyclic cation, which become the C-5 and C-4 carbons, respectively, of the cyclic cation. (Reproduced with permission from Hernandez, E. D.; Manookian, B.; Auerbach, S. M.; Jentoft, F. C. Shape-Selective Synthesis of Alkylcyclopentenyl Cations in Zeolites and Spectroscopic Distinction of Constitutional Isomers. *ACS Catal.* 2021, *11* (21), 12893–12914. Copyright 2021 American Chemical Society.)

3.3.2 Experimental data and findings

We begin the results section of this chapter with a discussion of the experimental results previously reported in *ACS Catalysis*.¹³ For a more detailed discussion of the experimental data, we refer the reader to the aforementioned journal article.

UV–vis spectra were measured during the adsorption and subsequent temperature increase of 2,6-dimethyl-2,4,6-octatriene on H-MOR, H-ZSM-5, and H-ZSM-22. For a detailed description and analysis of the UV-visible data, we refer the reader to our published journal article in *ACS Catalysis*.¹³ Upon adsorption in all three zeolites, a strong band forms at around 400 nm. This absorption band has been previously assigned to the conjugated system of a protonated triene molecule on H-ZSM-5.³ Similar dienyl cations such as dimethylheptadienyl and dimethyloctadienyl cations absorb at 396 and 400 nm, respectively as shown in previous reports.^{3,37}

It is important to take note of the findings here from the UV-Visible data. Raising the temperature of the system results in a depletion of the band near 400 nm. Notably, in

the case of HZSM-22 a higher temperature is required to begin reduction of the 400 nm band suggesting a longer-lived species. Comparing the high temperature bands in all three zeolites we find a possible difference in the products that are formed. More interestingly, the band that forms at higher temperatures in HZSM-5 shows character of multiple products being formed. This may be due to the more open pore structure of the HZSM-5 intersections as compared to the confined environment of the straight channels in HZSM-22.

The DRIFT spectra measured after adsorption of 2,6-dimethyl-2,4,6-octatriene, and subsequent temperature increase, on H-MOR, HZSM-5, and HZSM-22 show a similar trend of product formation as what was seen in the UV-Visible data. Figure 3.3A shows the adsorption of the alkatriene at 20 °C on H-MOR. Upon adsorption there appears a strong signature at 1567 cm^{-1} , which we attribute to the $\nu_{\text{as}}(\text{C}=\text{C}-\text{C}^+)$ stretch of the 2,6-dimethyloctadienyl protonated molecule as reported in Chapter 2. Next, as the system is heated to 120 °C, the 1567 cm^{-1} band is diminished and a strong band and shoulder appear at 1492 and 1462 cm^{-1} , respectively, providing evidence that new species have formed from the acyclic molecule.

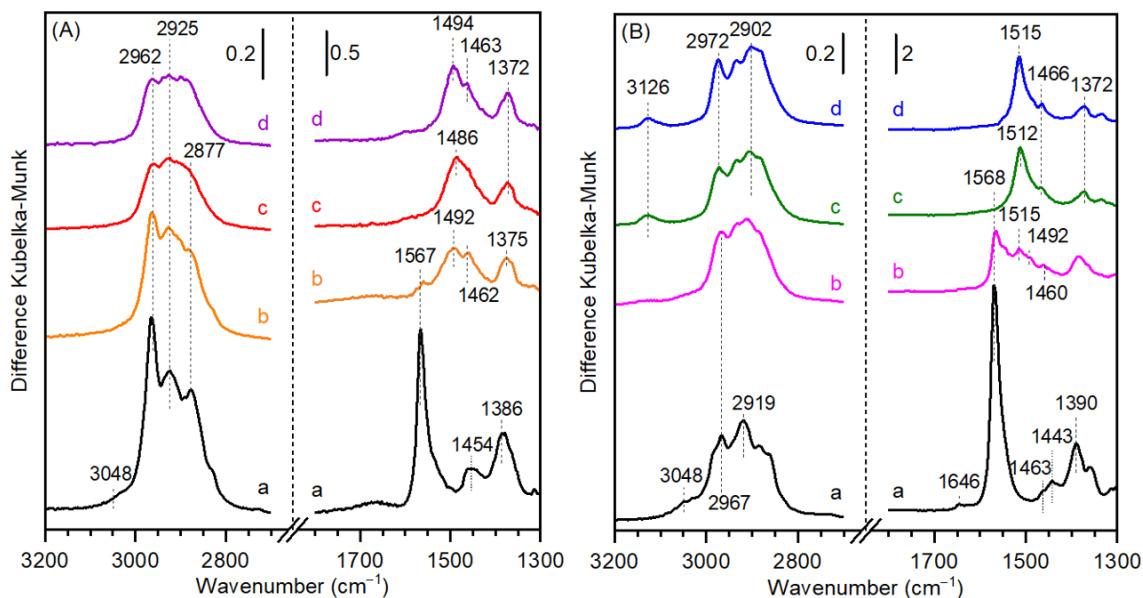


Figure 3.3 Difference DRIFT spectra during the in situ TPReact of 2,6-dimethyl-2,4,6-octatriene on (A) H-MOR (zeolite diluted to 20 wt.% in KBr) and (B) H-ZSM-5 (zeolite diluted to 33 wt.% in KBr) at (a) 20 °C, (b) 120 °C, (c) 200 °C, and (d) after cooling the zeolite back to 20 °C. Spectra are offset for clarity. (Reproduced with permission from Hernandez, E. D.; Manookian, B.; Auerbach, S. M.; Jentoft, F. C. Shape-Selective Synthesis of Alkylcyclopentenyl Cations in Zeolites and Spectroscopic Distinction of Constitutional Isomers. *ACS Catal.* 2021, 11 (21), 12893–12914. Copyright 2021 American Chemical Society.)

Figure 3.3B shows the adsorption of 2,6-dimethyloctatriene on HZSM-5. Upon adsorption, a strong IR band is seen at about 1567 cm^{-1} , once again associated with the $\nu_{\text{as}}(\text{C}=\text{C}-\text{C}^+)$ of the alkadienyl cation thought to be formed from protonation. Upon heating the sample to 120 °C (Figure 3.3B – pink spectrum), it appears that the alkadienyl species transforms as the sharp band at 1567 cm^{-1} depletes. Further elevation of the temperature to 200 °C results in complete depletion of the band at 1567 cm^{-1} and the emergence of a strong absorption band at 1515 cm^{-1} . We note that this high temperature band in HZSM-5 is blue-shifted from that which was seen in HMOR by about 26 cm^{-1} . Similar to what we saw in the UV-Visible data, this suggests the possibility of a different product forming in HZSM-5 versus HMOR.

Finally, we consider the DRIFTS associated with adsorption of the alkatriene on HZSM-22, shown in Figure 3.4. Similar to HMOR and HZSM-5, adsorption at 20 °C gives rise to a band at 1567 cm^{-1} attributed to the protonated alkatriene and the $\nu_{\text{as}}(\text{C}=\text{C}-\text{C}^+)$ allylic vibration. The band that initially forms is relatively weak as compared to the two other zeolites and only reaches its full intensity when the temperature is raised to 150 °C. We also note here that this slow process of protonation follows what we observed when monitoring with UV-Visible spectroscopy.

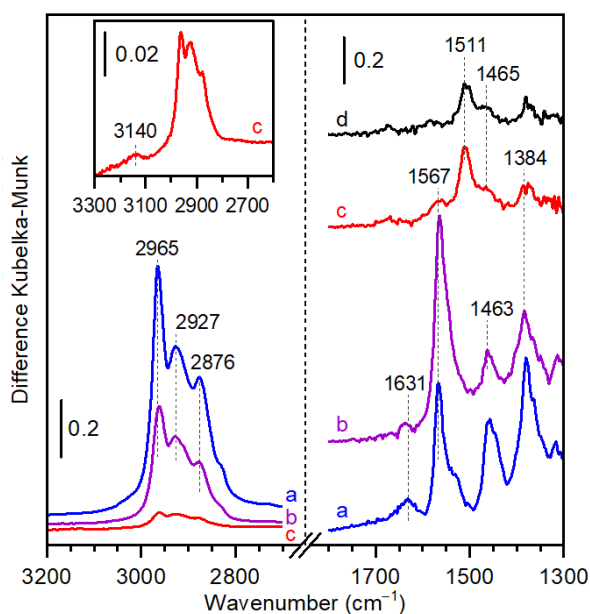


Figure 3.4 Difference DRIFT spectra during the in situ TPreact of 2,6-dimethyl-2,4,6-octatriene on H-ZSM-22 (zeolite diluted to 33 wt.% in KBr) at (a) 20 °C, (b) 150 °C, (c) 250 °C, and (d) 300 °C. Spectra between 1300 and 1800 cm^{-1} are offset for clarity. Inset: Magnification of the region of spectrum measured at 250 °C between 2600 and 3300 cm^{-1} . (Reproduced with permission from Hernandez, E. D.; Manookian, B.; Auerbach, S. M.; Jentoft, F. C. Shape-Selective Synthesis of Alkylcyclopentenyl Cations in Zeolites and Spectroscopic Distinction of Constitutional Isomers. *ACS Catal.* 2021, *11* (21), 12893–12914. Copyright 2021 American Chemical Society.)

One explanation of this occurrence is the possibility of protonation of the acyclic molecule at the pore mouths of the zeolite during partial adsorption into the zeolite pores. As the temperature is increased, the acyclic trienes diffuse farther into the pores of

HZSM-22 and access more Brønsted acid sites inside the pores, resulting in an increase in the intensity of the protonated alkatriene band.

The DRIFT spectra in Figures 3.3 and 3.4 in the three respective zeolites have significant similarities and differences. In all three zeolites, adsorption of the alkatriene molecule at 20 °C results in a strong adsorption band around 1567 cm^{-1} which we attribute to protonation of the alkatriene at the Brønsted acid sites. Our previous work confirmed this band to be associated with the allylic stretch $\nu_{\text{as}}(\text{C}=\text{C}-\text{C}^+)$ of the acyclic cation.⁴ A minor difference is the case of HZSM-22 where slightly elevated temperatures are required to reach maximum intensity of the allylic stretch band, but overall the picture is qualitatively the same. At elevated temperatures, however, the IR spectra in the three zeolites begin to show notable changes. Specifically, at 200 °C the spectrum of HMOR shows a broad band with maximum intensity at 1486 cm^{-1} , whereas in the case of HZSM-5 and HZSM-22, the band forms with a maximum intensity at a blue-shifted wavenumber value of 1512 and 1511 cm^{-1} , respectively.

The differences in the experimental IR spectra for adsorption of the alkatriene in the three zeolites are of particular importance. Namely, there is a strong possibility that the products that are forming at elevated temperatures differ in the three zeolites, similar to what was concluded from the UV-Visible data. This, however, raises the question of what the nature of these differences in the products might be. We anticipate the formation of alkyl-substituted cyclopentenyl cations at elevated temperatures in accordance with our previous findings as well as from previous reports.^{2,3,37} However, the exact nature of the cyclopentenyl cations – namely the alkyl substitution patterns of the allylic system –

remain unclear. Next, we utilize our computational techniques to ascertain the possible molecular differences that lead to the different IR spectra at the higher temperature.

3.3.3 Results from Theory

3.3.3.1 DFT Computed IR Spectra of Alkenyl, Alkadienyl, and Alkylcyclopentenyl Cations.

We next investigated the differences observed in the experimental IR spectra using our computational techniques. As highlighted in Chapter 2, we benchmarked DFT-computed IR spectra against experiment and found that for acyclic cations in the gas phase and zeolite, the calculated band positions were in good agreement (within a few wavenumbers) with the experimental values.⁴ Figure 3.5 shows the structures of cations that were investigated using our computational models for this work. We chose these cations to conduct a systematic investigation of impact of allylic substitution on the IR spectrum.

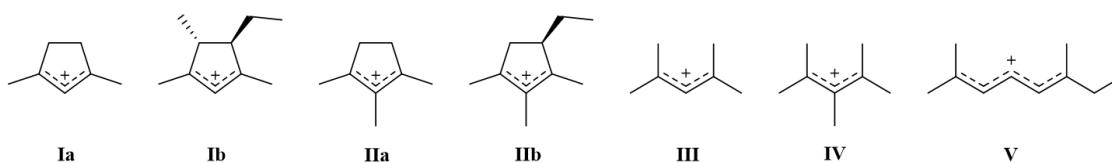


Figure 3.5 Structures of enylic carbenium ions investigated using DFT and MP2 methods. (Reproduced with permission from Hernandez, E. D.; Manookian, B.; Auerbach, S. M.; Jentoft, F. C. Shape-Selective Synthesis of Alkylcyclopentenyl Cations in Zeolites and Spectroscopic Distinction of Constitutional Isomers. *ACS Catal.* 2021, *11* (21), 12893–12914. Copyright 2021 American Chemical Society.)

We employed the Gaussian 09 software to compute IR spectra of gas phase cations using a BLYP functional and 6-311G(d) basis set via DFT (Figure 3.6) and visualized the normal modes to assist with assignment of bands. Figure 3.6A displays the computed spectra of two acyclic cations, the 2,4-dimethylpentenyl cation (**III**) and the

2,3,4-trimethylpentenyl cation (**IV**). We distinguish between these two cations by the substitution at the center allylic carbon which is either a hydrogen (**III**) or methyl group (**IV**). Figure 3.6A shows the spectrum of cation **III**. In the spectrum there is a band at 1540 cm^{-1} assigned to the $\nu_{\text{as}}(\text{C}=\text{C}-\text{C}^+)$, as reported in previous studies.^{3,4} Cation **IV** gives a notably different computed spectrum where the band associated with the same allylic stretch is red-shifted by -28 cm^{-1} to 1512 cm^{-1} . Figure 3.6B shows the DFT-computed IR spectra of the 1,3-dimethylcyclopentenyl cation (**Ia**) and the 1,2,3-trimethylcyclopentenyl cation (**IIa**) where the $\nu_{\text{as}}(\text{C}=\text{C}-\text{C}^+)$ stretch bands are located at 1508 cm^{-1} and 1486 cm^{-1} for **Ia** and **IIa**, respectively. Similar to the acyclic cations in Figure 3.6A, we note a significant red-shift in band position due to the presence of a methyl group on the center carbon of the allylic system. In all cases, the allylic cation with a methyl group at the center carbon has a band that is red-shifted from that of the hydrogen-substituted counterpart.

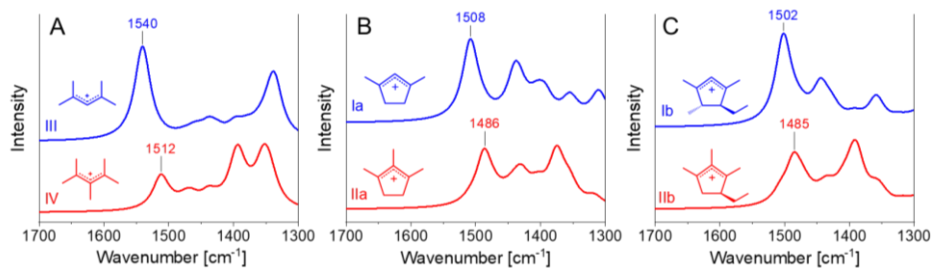


Figure 3.6 Computed IR spectra via Gaussian 09 of (A) acyclic monoenyl cations **III** and **IV**, (B) methyl-substituted cyclopentenyl cations **Ia** and **IIa**, and (C) ethyltrimethylcyclopentenyl cations **Ib** and **IIb** in the gas phase. Spectra are computed using BLYP/6-311G(d); frequencies are fit to Lorentzian functions and scaled by 0.998.

We further explored this shift by computing IR spectra for mass-balanced alkyl substituted cyclopentenyl cations **Ib** and **IIb**, relative to the alkatriene molecule (**V**). Figure 3.6C shows the gas-phase computed spectra of 1,3,5-trimethyl-4-ethylcyclopentenyl cation (**Ib**) and the 1,2,3-trimethyl-4-ethylcyclopentenyl cation (**IIb**).

Cation **Ib** exhibits a band at 1502 cm^{-1} attributed to the allylic stretch. In contrast, the spectrum for cation **IIb** shows a band at 1485 cm^{-1} which is also assigned to the allylic stretch but red-shifted. We also surmise that the methyl or ethyl substitution at non-allylic carbons in the ring (C-4 & C-5) does not have a significant impact on the location of the band. These spectra further showcase that the presence of a methyl group at the center carbon is indicative of a red-shift in the allylic stretching band.

Next, we moved to determine if the IR shift due to allylic substitution persisted in the zeolite. We used periodic DFT to compute IR spectra within CP2K using PBE/TZVP for cations **V**, **Ib**, and **IIb** within the zeolite pores of HMOR, HZSM-5, and HZSM-22. We computed spectra for different rotational configurations of each of the cations within the zeolite. Based on the relative Helmholtz energies, a Boltzmann-weighted sum spectrum was produced. The frequencies of the $\nu_{\text{as}}(\text{C}=\text{C}-\text{C}^+)$ of these cations computed in the gas phase and adsorbed on zeolites are summarized in Table 3.1.

Table 3.1 Summary of Computed Frequencies of Allylic Stretching Vibrations of Gas-Phase and Zeolite-Sorbed Alkenyl Cations. (Reproduced with permission from Hernandez, E. D.; Manookian, B.; Auerbach, S. M.; Jentoft, F. C. Shape-Selective Synthesis of Alkylcyclopentenyl Cations in Zeolites and Spectroscopic Distinction of Constitutional Isomers. *ACS Catal.* 2021, *11* (21), 12893–12914. Copyright 2021 American Chemical Society.)

Cation	$\nu_{\text{as}}(\text{C}=\text{C}-\text{C}^+) / \text{cm}^{-1}$			
	Gas-Phase ^a	MOR ^b	ZSM-5 ^b	ZSM-22 ^b
Ib	1502	1491	1492	1504
IIb	1486	1484	1476	1475
V	1570 ^c	1560	1553	1553
IIb – Ib	-16	-7	-16	-29
$\mathbf{V}_{\text{zeolite-sorbed}}$	--	-10	-17	-17
$-\mathbf{V}_{\text{gas-phase}}$				

^a Gaussian 09, gas-phase, BLYP/6-311G(d), frequencies scaled 0.998

^b CP2K, zeolite-sorbed, PBE/TZVP, Boltzmann-weighted sum, frequencies scaled 0.990

^c Manookian et al. Ref. ⁴

We used the $\nu_{\text{as}}(\text{C}=\text{C}-\text{C}^+)$ of cation **V** as a benchmark for the interpretation of the computed spectra of cations in the three zeolites. It has been previously reported that the $\nu_{\text{as}}(\text{C}=\text{C}-\text{C}^+)$ of cation **V** is observed at around 1568 cm^{-1} in 96% sulfuric acid³ and $1566\text{--}1568\text{ cm}^{-1}$ on H-form zeolites.^{3,4} We also previously computed the band for the gas-phase cation at 1570 cm^{-1} , using BLYP/6-311G(d).⁴ For cation **V**, bands associated with $\nu_{\text{as}}(\text{C}=\text{C}-\text{C}^+)$ are observed at 1560 , 1553 , and 1553 cm^{-1} in the computed IR spectra of this species adsorbed in HMOR, HZSM-5, and HZSM-22, respectively. We found that the computed IR spectra in the zeolite (CP2K–PBE/TZVP) yields $\nu_{\text{as}}(\text{C}=\text{C}-\text{C}^+)$ bands which are in general red shifted from both experimental and gas-phase calculated spectra. In line with this, cations **Ib** and **Iib** adsorbed in the zeolite exhibit $\nu_{\text{as}}(\text{C}=\text{C}-\text{C}^+)$ band frequencies that are red-shifted from the predicted gas-phase values (Gaussian–BLYP/6-311G(d)), as shown in Table 3.1 above. The computed shift of this band, attributed to methyl substitution at the center allylic carbon, from cation **Ib** to cation **Iib** ($\Delta\nu$) is -7 cm^{-1} , -16 cm^{-1} , -29 cm^{-1} for HMOR, HZSM-5, and HZSM-22, respectively. We conclude based on our models, keeping in mind the differences between gas-phase and zeolite computed spectra, that the red-shift associated with methyl substitution at the center carbon of the allylic system is persistent in the zeolite.

3.3.2.2 DFT and MP2 Investigation of the Thermodynamics of Alkylcyclopentenyl-Zeolite Systems.

The thermodynamics of type **I** and type **II** alkyl cyclopentenyl cations were studied in the gas phase and in zeolites, using both MP2 and DFT methods. Our goal here was to determine the relative stabilities of the types of cations that were possibly forming in the experiment. Following the work above, we explicitly explored the impact of the

center substitution of the allylic system, either a methyl or hydrogen group. We also explored the sensitivity of the relative stability on the location of the bulkier ethyl group, either at a terminal allylic carbon or at a non-allylic carbon. Gibbs energies (ΔG) were computed at 200 °C, shown in Figure 3.7, for gas-phase ethyltrimethylcyclopentenyl cation isomers. Comparison of the ΔG values was achieved by considering their stabilities relative to the acyclic precursor **V**.⁴ The DFT functionals BLYP, B3LYP, and PBE as well as MP2 were used to evaluate (1) the relative thermodynamic stabilities across multiple computational models, and (2) the relative thermodynamic stabilities of the alkylcyclopentenyl cation isomers in the gas phase.

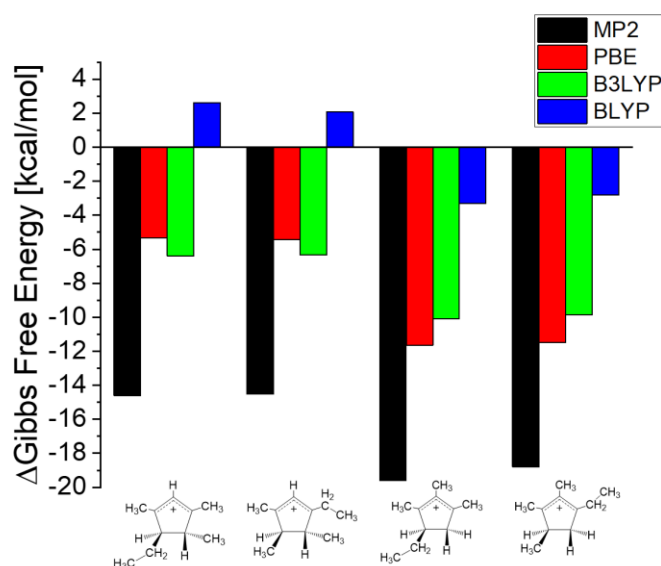


Figure 3.7 Comparison of computed Gibbs energies (at 200 °C) of ethyltrimethylcyclopentenyl cation isomers computed using varying DFT functionals (PBE, BLYP, B3LYP) and MP2.

Figure 3.7 shows that MP2, and B3LYP and PBE density functionals predict a decrease in gas-phase free energy upon cyclization of cation **V** to cations of type **I** and **II**. The BLYP functional, however, predicts an endothermic reaction upon cyclization to the

hydrogen substituted **Ib** and **Ic** and misses the exothermicity of cyclization to the **IIb** and **IIc** as is seen for the other models. We do note, however, that the methyl-substituted cations are more stable across all levels of theory, consistent with findings in prior work in strong liquid acids.³⁸ We also note consistency in ΔG values between type **I** and type **II** cations (i.e., $\Delta\Delta G$ values) despite some discrepancies across the DFT and MP2 methods. The differences in computed ΔG values between isomer **Ib** and **IIb** are -5.0 , -6.3 , -3.7 , and -5.9 kcal mol⁻¹ for MP2, PBE, B3LYP, and BLYP, respectively. Notably, the relative differences in stabilities in the gas phase between cations **I** and **II** are captured in all models. In regard to the ethyl substituent, our models predict that terminal allylic substitution and non-allylic substitution of the ethyl group does not result in a significant change in relative stabilities of the cation. Specifically, moving the ethyl group from the non-allylic C4 carbon in **Ib** to the terminal allylic C3 carbon in **Ic** results in a change in relative stability of $+0.1$ kcal/mol (MP2). This follows previous reports by Sorensen that the change in free energy associated with this type of substitution change ranged from -0.3 to -1.76 kcal/mol.³⁷

We computed adsorption Helmholtz energies ($\Delta A_{\text{overall}}$) to investigate if the thermodynamic stability was consistent with the appearance of the cations in the zeolites. Because the PBE density functional was found to underestimate the Gibbs energy change in comparison to MP2 results for cyclization in the gas phase (see Figure 3.7), we sought to approach MP2-level accuracy for the zeolite-guest energetics without having to pay the exorbitant computational price of using MP2 within CP2K for calculations on these large unit cells. To accomplish this goal, we note very consistent negative shifts in ΔG values from PBE to MP2 in Figure 3.7, namely, -8.4 ± 1.1 kcal/mol. As this energetic correction

represents an intrinsic molecular property, it should apply to zeolite–guest systems as well. As such, we applied this PBE-to-MP2 energy correction to computed Helmholtz free energies for the zeolite–guest systems shown in Table 3.2 (denoted with superscript a). For comparison we also report in Table 3.2 the non-corrected Helmholtz energies for all zeolite–guest systems. Although this approach does not capture PBE-to-MP2 corrections to host–guest energies, we expect such corrections to be relatively small because of the use of dispersion-corrected PBE.

Table 3.2 Computed free energies for cyclopentenyl cations in respective zeolites. (Reproduced with permission from Hernandez, E. D.; Manookian, B.; Auerbach, S. M.; Jentoft, F. C. Shape-Selective Synthesis of Alkylcyclopentenyl Cations in Zeolites and Spectroscopic Distinction of Constitutional Isomers. *ACS Catal.* 2021, *11* (21), 12893–12914. Copyright 2021 American Chemical Society.)

Reaction		ΔA (kcal mol ⁻¹)							
		H-MOR		H-ZSM-5(i)		H-ZSM-5(s)		H-ZSM-22	
ΔA_1^b	Ads. Of Neutral	-33.7		-18.6		-17.2		-27.2	
ΔA_2	Protonation	-6.21		-19.5		-16.6		-9.79	
Cyclopentenyl Cation		Ib	IIb	Ib	IIb	Ib	IIb	Ib	IIb
ΔA_3	Cyclization	-7.70	-15.9	3.10	-7.20	12.8	12.8	-1.50	-5.10
ΔA_3^a		-16.9	-23.5	-6.10	-14.8	3.60	5.20	-10.7	-12.7
ΔA	TOTAL	-47.6	-55.8	-34.9	-45.2	-21.0	-21.0	-38.5	-42.1
ΔA^a		-56.8	-63.4	-44.1	-52.8	-30.2	-28.6	-47.7	-49.7

^a Helmholtz energies (computed using CP2K–PBE/TZVP) with an estimated correction from gas-phase Gibbs energy calculations using Gaussian–MP2/6-311G(d).

^b Gas-phase neutral Gibbs energy estimated using Gibbs correction computed in Gaussian with comparable level of theory–PBE/6-311G(d)

Table 3.2 showcases the computed change in adsorption Helmholtz energies of cations **Ib** and **IIb** in the zeolite frameworks. Isomer **IIb** is more stable than **Ib** in three of the four zeolite-adsorbed systems studied, similar to what we found in the gas phase. Notably, isomer **Ib** and **IIb** have the same adsorption Helmholtz energy in the H-ZSM-5 straight channel, pointing to the possibility that the favorability towards **IIb** becomes null due to sterics in the more confined space of the straight channel. For the more stable cation **IIb**, the Helmholtz energy for cyclization is found to be the most strongly negative in the large-pore zeolite H-MOR, and the least strongly negative in the 1D medium-pore

zeolite HZSM-22, while it assumes an intermediate value in the intersections of HZSM-5. Overall, these computational results predict that, if thermodynamics controlled alkyl substitution patterns in these cyclopentenyl cations, we would expect methyl substitution at the C2 carbon in all zeolites studied except for those forming in the straight channels of HZSM-5.

3.4 Conclusions

The work outlined in Chapter 3 explored the formation of alkyl-substituted cyclopentenyl cations on zeolites MOR, MFI, and TON with varying channel diameters and geometries via a coupled experimental and computational spectroscopy approach. We specifically looked at the difference in the center substituent of the allylic system in the cyclopentenyl cations. Experimental UV–vis spectra, collected by Dr. E. Hernandez and Prof. F. Jentoft, showcased that there may be different products forming in the three zeolites due to differences in the UV-visible bands appearing at elevated temperatures. We explored this phenomenon further by considering data obtained by DRIFT spectroscopy experiments. We found that in all zeolites a band at 1567 cm^{-1} was associated with the protonation of the acyclic olefin which began to deteriorate as the temperature was raised. At elevated temperatures of around $200\text{ }^{\circ}\text{C}$, new bands emerged in all zeolites in the lower wavenumber region between 1400 and 1600 cm^{-1} . Specifically, we found that in HMOR a band appeared at 1465 cm^{-1} whereas in HZSM-5 and HZSM-22 bands appeared at 1511 and 1510 cm^{-1} , respectively. We attributed this difference to the formation of differently substituted alkyl cyclopentenyl cations. Namely, we hypothesized the difference was associated with the center substitution being either a methyl or a hydrogen. We investigated this by incorporating our computational models

for gas-phase and zeolite-adsorbed IR spectroscopy as well as thermodynamic calculations.

We computed DFT IR spectra of gas phase and zeolite adsorbed species and found a sensitivity to the center substitution of the allylic system. Specifically, a methyl substitution resulted in a red-shift of about 25 cm^{-1} in the gas phase as well as all three zeolites. We explored the thermodynamics of this process by computing relative free energies of the alkyl-substituted cations relative to a hypothetical protonated acyclic triene. We found that the methyl-substituted cyclopentenyl cation was more stable in the gas phase (by about 5.01 kcal/mol) as well as in the large pore zeolite HMOR (6.6 kcal/mol). When considering the medium pore zeolites, we found surprisingly that the relative stability of the methyl-substituted cyclopentenyl persisted in the HZSM-5 intersection (8.70 kcal/mol) and HZSM-22 (2.00 kcal/mol), however the favorability is not apparent in the straight channels of HZSM-5. This finding suggests that the process by which these substituted cyclopentenyl cations form is not under thermodynamic control and may be kinetically controlled.

In the next chapter, we move to investigate the extent of kinetic control on the formation of type **I** and **II** alkyl-substituted cyclopentenyl cations. We will incorporate zero-Kelvin and finite temperature computational techniques in tandem to compute free energy barriers associated with isomerization of the cyclopentenyl cation. With those in hand, we will build a kinetic model to determine the extent of differences in the rates of formation of the two types of cations.

3.5 References

- (1) Yarulina, I.; Chowdhury, A. D.; Meirer, F.; Weckhuysen, B. M.; Gascon, J. Recent Trends and

- Fundamental Insights in the Methanol-to-Hydrocarbons Process. *Nat. Catal.* **2018**, *1* (6), 398–411. <https://doi.org/10.1038/s41929-018-0078-5>.
- (2) Wulfers, M. J.; Jentoft, F. C. The Role of Cyclopentadienium Ions in Methanol-to-Hydrocarbons Chemistry. *ACS Catal.* **2014**, *4* (10), 3521–3532. <https://doi.org/10.1021/cs500722m>.
 - (3) Hernandez, E. D.; Jentoft, F. C. Spectroscopic Signatures Reveal Cyclopentenyl Cation Contributions in Methanol-to-Olefins Catalysis. *ACS Catal.* **2020**, *10* (10), 5764–5782. <https://doi.org/10.1021/acscatal.0c00721>.
 - (4) Manookian, B.; Hernandez, E. D.; Baer, M. D.; Mundy, C. J.; Jentoft, F. C.; Auerbach, S. M. Experimental and DFT Calculated IR Spectra of Guests in Zeolites: Acyclic Olefins and Host–Guest Interactions. *J. Phys. Chem. C* **2020**, *124* (19), 10561–10572. <https://doi.org/10.1021/acs.jpcc.0c01225>.
 - (5) Zhang, W.; Chen, J.; Xu, S.; Chu, Y.; Wei, Y.; Zhi, Y.; Huang, J.; Zheng, A.; Wu, X.; Meng, X.; et al. Methanol to Olefins Reaction over Cavity-Type Zeolite: Cavity Controls the Critical Intermediates and Product Selectivity. *ACS Catal.* **2018**, *8* (12), 10950–10963. <https://doi.org/10.1021/acscatal.8b02164>.
 - (6) Zhang, M.; Xu, S.; Wei, Y.; Li, J.; Chen, J.; Wang, J.; Zhang, W.; Gao, S.; Li, X.; Wang, C.; et al. Methanol Conversion on ZSM-22, ZSM-35 and ZSM-5 Zeolites: Effects of 10-Membered Ring Zeolite Structures on Methylcyclopentenyl Cations and Dual Cycle Mechanism. *RSC Adv.* **2016**, *6* (98), 95855–95864. <https://doi.org/10.1039/C6RA08884H>.
 - (7) Hemelsoet, K.; Ghysels, A.; Mores, D.; De Wispelaere, K.; Van Speybroeck, V.; Weckhuysen, B. M.; Waroquier, M. Experimental and Theoretical IR Study of Methanol and Ethanol Conversion over H-SAPO-34. *Catal. Today* **2011**, *177* (1), 12–24. <https://doi.org/https://doi.org/10.1016/j.cattod.2011.05.040>.
 - (8) Hemelsoet, K.; Qian, Q.; De Meyer, T.; De Wispelaere, K.; De Sterck, B.; Weckhuysen, B. M.; Waroquier, M.; Van Speybroeck, V. Identification of Intermediates in Zeolite-Catalyzed Reactions by In Situ UV/Vis Microspectroscopy and a Complementary Set of Molecular Simulations. *Chem. – A Eur. J.* **2013**, *19* (49), 16595–16606. <https://doi.org/https://doi.org/10.1002/chem.201301965>.
 - (9) Mosley, J. D.; Young, J. W.; Agarwal, J.; Schaefer III, H. F.; Schleyer, P. v. R.; Duncan, M. A. Structural Isomerization of the Gas-Phase 2-Norbornyl Cation Revealed with Infrared Spectroscopy and Computational Chemistry. *Angew. Chemie Int. Ed.* **2014**, *53* (23), 5888–5891. <https://doi.org/https://doi.org/10.1002/anie.201311326>.
 - (10) Deno, N. C.; Richey, H. G.; Friedman, N.; Hodge, J. D.; Houser, J. J.; Pittman, C. U. Carbonium Ions. XI. Nuclear Magnetic Resonance Spectra of the Aliphatic Alkenyl Cations. *J. Am. Chem. Soc.* **1963**, *85* (19), 2991–2995.
 - (11) Olah, G. A.; Clifford, P. R.; Halpern, Y.; Johanson, R. G. Stable Carbocations. CXIX. Carbon-13 Nuclear Magnetic Resonance Spectroscopy Study of the Structure of Allyl Cations. *J. Am. Chem. Soc.* **1971**, *93* (17), 4219–4222. <https://doi.org/10.1021/ja00746a022>.
 - (12) Olah, G. A.; Pittman, C. U.; Symons, M. C. R. Electronic Spectra. In *Carbonium Ions*; Olah, G. A., Schleyer, P. von R., Eds.; Interscience Publishers: New York, 1968; Vol. 1, pp 153–222.
 - (13) Hernandez, E. D.; Manookian, B.; Auerbach, S. M.; Jentoft, F. C. Shape-Selective Synthesis of Alkylcyclopentenyl Cations in Zeolites and Spectroscopic Distinction of Constitutional Isomers. *ACS Catal.* **2021**, *11* (21), 12893–12914. <https://doi.org/10.1021/acscatal.1c03039>.
 - (14) Baerlocher, C.; McCusker, L. B.; Olson, D. H. *Atlas of Zeolite Framework Types*, Sixth Edit.; Elsevier Science B.V.: Amsterdam, 2007.
 - (15) Baerlocher, C.; McCusker, L. B. International Zeolite Association: Database of Zeolite Structures.
 - (16) Rasmussen, D. B.; Christensen, J. M.; Temel, B.; Studt, F.; Moses, P. G.; Rossmeis, J.; Riisager, A.; Jensen, A. D. Reaction Mechanism of Dimethyl Ether Carbonylation to Methyl Acetate over Mordenite – a Combined DFT/Experimental Study. *Catal. Sci. Technol.* **2017**, *7* (5), 1141–1152. <https://doi.org/10.1039/C6CY01904H>.
 - (17) Alexopoulos, K.; Lee, M. S.; Liu, Y.; Zhi, Y.; Liu, Y.; Reyniers, M. F.; Marin, G. B.; Glezakou, V. A.; Rousseau, R.; Lercher, J. A. Anharmonicity and Confinement in Zeolites: Structure, Spectroscopy, and Adsorption Free Energy of Ethanol in H-ZSM-5. *J. Phys. Chem. C* **2016**, *120* (13), 7172–7182. <https://doi.org/10.1021/acs.jpcc.6b00923>.
 - (18) Moses, P. G.; Nørskov, J. K. Methanol to Dimethyl Ether over ZSM-22: A Periodic Density Functional Theory Study. *ACS Catal.* **2013**, *3* (4), 735–745. <https://doi.org/10.1021/cs300722w>.
 - (19) De Moor, B. A.; Ghysels, A.; Reyniers, M.-F.; Van Speybroeck, V.; Waroquier, M.; Marin, G. B.

- Normal Mode Analysis in Zeolites: Toward an Efficient Calculation of Adsorption Entropies. *J. Chem. Theory Comput.* **2011**, *7* (4), 1090–1101. <https://doi.org/10.1021/ct1005505>.
- (20) Brändle, M.; Sauer, J. Acidity Differences between Inorganic Solids Induced by Their Framework Structure. A Combined Quantum Mechanics/Molecular Mechanics Ab Initio Study on Zeolites. *J. Am. Chem. Soc.* **1998**, *120* (7), 1556–1570. <https://doi.org/10.1021/ja9729037>.
- (21) De Moor, B. A.; Reyniers, M.-F.; Gobin, O. C.; Lercher, J. A.; Marin, G. B. Adsorption of C2–C8 N-Alkanes in Zeolites. *J. Phys. Chem. C* **2011**, *115* (4), 1204–1219. <https://doi.org/10.1021/jp106536m>.
- (22) Sklenak, S.; Dědeček, J.; Li, C.; Wichterlová, B.; Gábová, V.; Sierka, M.; Sauer, J. Aluminium Siting in the ZSM-5 Framework by Combination of High Resolution 27Al NMR and DFT/MM Calculations. *Phys. Chem. Chem. Phys.* **2009**, *11* (8), 1237–1247. <https://doi.org/10.1039/b807755j>.
- (23) Nguyen, C. M.; Reyniers, M. F.; Marin, G. B. Theoretical Study of the Adsorption of the Butanol Isomers in H-ZSM-5. *J. Phys. Chem. C* **2011**, *115* (17), 8658–8669. <https://doi.org/10.1021/jp111698b>.
- (24) Sklenak, S.; Dědeček, J.; Li, C.; Gao, F.; Jansang, B.; Boekfa, B.; Wichterlova, B.; Sauer, J. Aluminum Siting in the ZSM-22 and Theta-1 Zeolites Revisited: A QM/MM Study. *Collect. Czechoslov. Chem. Commun.* **2008**, *73* (6–7), 909–920. <https://doi.org/10.1135/cccc20080909>.
- (25) Chen, Z.; Liu, S.; Wang, H.; Ning, Q.; Zhang, H.; Yun, Y.; Ren, J.; Li, Y. W. Synthesis and Characterization of Bundle-Shaped ZSM-22 Zeolite via the Oriented Fusion of Nanorods and Its Enhanced Isomerization Performance. *J. Catal.* **2018**, *361*, 177–185. <https://doi.org/10.1016/j.jcat.2018.02.019>.
- (26) Derewinski, M.; Sarv, P.; Mifsud, A. Thermal Stability and Siting of Aluminum in Isostructural ZSM-22 and Theta-1 Zeolites. *Catal. Today* **2006**, *114* (2–3), 197–204. <https://doi.org/10.1016/j.cattod.2006.01.008>.
- (27) Nguyen, C. M.; Reyniers, M.-F.; Marin, G. B. Adsorption Thermodynamics of C1–C4 Alcohols in H-FAU, H-MOR, H-ZSM-5, and H-ZSM-22. *J. Catal.* **2015**, *322*, 91–103. <https://doi.org/https://doi.org/10.1016/j.jcat.2014.11.013>.
- (28) Dědeček, J.; Sobalík, Z.; Wichterlová, B. Siting and Distribution of Framework Aluminium Atoms in Silicon-Rich Zeolites and Impact on Catalysis. *Catal. Rev. - Sci. Eng.* **2012**, *54* (2), 135–223. <https://doi.org/10.1080/01614940.2012.632662>.
- (29) Vandevonede, J.; Krack, M.; Mohamed, F.; Parrinello, M.; Chassaing, T.; Hutter, J. Quickstep: Fast and Accurate Density Functional Calculations Using a Mixed Gaussian and Plane Waves Approach. *Comput. Phys. Commun.* **2005**, *167* (2), 103–128. <https://doi.org/10.1016/j.cpc.2004.12.014>.
- (30) Frisch, M. J.; Trucks, G. W.; Schlegel, H. B.; Scuseria, G. E.; Robb, M. A.; Cheeseman, J. R.; Scalmani, G.; Barone, V.; Mennucci, B.; Petersson, G. A.; et al. Gaussian 09, Revision B.01; Gaussian Inc.: Wallingford, CT, 2009.
- (31) Grimme, S.; Antony, J.; Ehrlich, S.; Krieg, H. A Consistent and Accurate Ab Initio Parametrization of Density Functional Dispersion Correction (DFT-D) for the 94 Elements H-Pu. *J. Chem. Phys.* **2010**, *132* (15), 154104. <https://doi.org/10.1063/1.3382344>.
- (32) Goedecker, S.; Teter, M.; Hutter, J. Separable Dual-Space Gaussian Pseudopotentials. *Phys. Rev. B* **1996**, *54* (3), 1703–1710. <https://doi.org/10.1103/PhysRevB.54.1703>.
- (33) VandeVondele, J.; Hutter, J. Gaussian Basis Sets for Accurate Calculations on Molecular Systems in Gas and Condensed Phases. *J. Chem. Phys.* **2007**, *127* (11), 114105. <https://doi.org/10.1063/1.2770708>.
- (34) Agarwal, V.; Huber, G. W.; Conner, W. C.; Auerbach, S. M. Simulating Infrared Spectra and Hydrogen Bonding in Cellulose I β at Elevated Temperatures. *J. Chem. Phys.* **2011**, *135* (13), 134506. <https://doi.org/10.1063/1.3646306>.
- (35) Wang, T.; Luo, S.; Tompsett, G. A.; Timko, M. T.; Fan, W.; Auerbach, S. M. Critical Role of Tricyclic Bridges Including Neighboring Rings for Understanding Raman Spectra of Zeolites. *J. Am. Chem. Soc.* **2019**, *141* (51), 20318–20324. <https://doi.org/10.1021/jacs.9b10346>.
- (36) NIST Computational Chemistry Comparison and Benchmark Database, NIST Standard Reference Database Number 101.
- (37) Sorensen, T. S. The Synthesis and Reactions of Divinyl Carbonium Ions. *Can. J. Chem.* **1964**, *42* (12), 2768–2780. <https://doi.org/10.1139/v64-410>.
- (38) Deno, N. C.; Friedman, N.; Hodge, J. D.; Houser, J. J. Carbonium Ions. XII. The Direct

Observation of Rearrangement and Hydrogen-Deuterium Exchange in Cycloalkenyl Cations. *J. Am. Chem. Soc.* **1963**, 85 (19), 2995–2997.

CHAPTER 4

SHAPE-SELECTIVITY OF CYCLOPENTENYL CATION ISOMERIZATION: INVESTIGATING THE EXTENT OF KINETIC CONTROL

4.1 Introduction

Alkyl-substituted cyclopentenyl cations have gained interest in the recent years as examples of cyclic hydrocarbons that play an active role in methanol conversion over acidic zeolite catalysts.¹⁻³ Cyclopentenyl cations can act as co-catalysts, but also may transform to larger species that deactivate the catalyst.^{3,4} More recent research has been focused on elucidating the mechanistic role cyclopentenyl cations play during acidic zeolite catalysis as well as their specific structures and formation processes.^{5,6} To that end, researchers have found that intramolecular and intermolecular transformations of cyclopentenyl cations via isomerization, methylation, protonation and deprotonation and other reactions contribute to their role in catalytic cycles.^{2,5,6} Gaining further insights into these types of processes can help to better understand the role of cyclopentenyl cations during methanol conversion in zeolites.


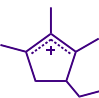
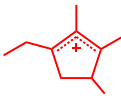
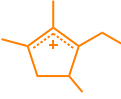
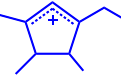
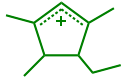
Intramolecular transformation of alkyl-substituted cyclopentenyl cations has been thoroughly studied in homogeneous acid media.⁷⁻¹⁰ Sorenson *et al.* investigated the formation of these cyclopentenyl cations from acyclic triene precursors in sulfuric acid.⁷ It was surmised that following cyclization, isomerization of the cyclopentenyl cation would occur to give rise to more thermodynamically stable cations.⁷ It is interesting to wonder if these molecular transformations occur differently inside the pores of zeolites and what impact a given zeolite's framework might have on the reaction mechanism and product distribution of such cyclopentenyl species.

Microporous acid zeolites H-ZSM-5 and H-ZSM-22 have pores and channels with sizes on par with the kinetic diameter of alkyl-substituted cyclopentenyl cations. Specifically, H-ZSM-5 is a medium pore zeolite with channel intersections that can accommodate a sphere with a diameter of up to 6.4 Å.^{11,12} H-ZSM-22 is also a medium pore zeolite, but in contrast it is strictly a straight channel framework (no intersections) which results in a more confined space that can accommodate spheres with diameters of up to only 5.7 Å.^{11,12} These zeolites in particular have been reported to exhibit shape-selectivity during methanol conversion processes.^{13,14} In fact, in the previous chapter we established that the alkyl-substituted cyclopentenyl cations that formed in medium pore zeolites are different from those forming in larger pore zeolites, further evidence of shape-selectivity. Interestingly, the DFT-predicted thermodynamics of cyclopentenyl formation from acyclic precursors did not correspond to what was being observed in the experiments. (The details of these results can be found in the ACS Catalysis article we published with our experimental collaborators, Hernandez *et al.*¹⁵) This leads us to the main question addressed in this chapter: *To what extent does confinement in medium pore zeolites H-ZSM-5 and H-ZSM-22 impact – promote or inhibit – the isomerization of alkyl-substituted cyclopentenyl cations to the thermodynamically favored isomers?*

Table 4.1 shows the relative thermodynamic stabilities of alkyl-substituted cyclopentenyl isomers described in this chapter. All the energies are reported in kcal/mol and are relative to the reactant molecule where the isomerization reaction initiates. We will report the differences between these isomers and the isomerization network in detail in the following sections. In brief, we will discuss two types of isomers, **T**-type and **K**-type, where **T**-type isomers have a methyl at the C-2 allylic carbon on the ring and **K**-

type isomers have a hydrogen at the C-2 allylic carbon. (See Table 4.1 for structures) We note here the differences in thermodynamic stabilities in the two zeolites. Namely, in H-ZSM-5, the **T2** isomer is the most stable isomer whereas in H-ZSM-22, **T3** is the most stable, but very close in energy to **T2**. Keeping these thermodynamics in mind, we will report the results from the kinetic analysis (Section 4.3.3) and comment on the extent of kinetic control for isomerization.

Table 4.1 Helmholtz energies of alkyl-substituted cyclopentenyl isomers relative to the reactant isomer where the isomerization reaction network begins. All energies reported in kcal/mol.

Helmholtz Energy Relative to Reactant		
Isomer	H-ZSM-5	H-ZSM-22
 Reactant	0.0	0.0
 T1	-34.8	-42.6
 T2	-40.5	-51.3
 T3	-27.8	-52.2
 K1	-29.2	-46.5
 K2	-24.8	-44.0

Understanding shape-selectivity in zeolites leads to the question of kinetic versus thermodynamic control of product formation. Under kinetic control the product which

forms at a higher rate (lower activation energy) is favored, whereas under thermodynamic control the more stable product (lower free energy) is favored. Generally, the reaction conditions, such as temperature, determine if the process is under kinetic or thermodynamic control. In the case of shape-selectivity in zeolites, however, the shape and size of zeolite pores become the determining factor of kinetic or thermodynamic control. This has been studied experimentally such as in the case of *p*-xylene formation during toluene methylation in medium pore zeolites.¹⁶ Although thermodynamics would predict only 20% *p*-xylene formation, the confined H-ZSM-22 zeolite pore structure exhibits shape-selectivity towards the *p*-xylene isomer (56% product formation).¹⁶ This is an example of diffusion mediated kinetic control where due to the ability of *p*-xylene to diffuse out of the pores because of its better fitting, it does not further react giving rise to other isomers. In a similar manner, zeolite pore structure can also result in transition state mediated kinetic control where formation of products is hindered due to bulkiness of intermediates or transition states.^{17,18} Sugi *et al.* showed this to be the case for the alkylation of biphenyl molecules in straight channel zeolites.¹⁷ Computationally, the rather simple approach of comparing free energy surfaces has shown a lot of promise in determining thermodynamic versus kinetic control of product formation.¹⁹ For instance, Chen *et al.* compared reaction and transition state free energies to determine thermodynamic and kinetic favorability between competing benzene methylation reactions in H-ZSM-5 and H-ZSM-22 zeolites.²⁰ Although these techniques prove useful in this manner, there remains room for a more reaction kinetics computational approach for studying the interplay between thermodynamic and kinetic control. In this work we begin with computed reaction and transition state energies and then incorporate a

microkinetic model as a method to investigate the extent of kinetic or thermodynamic control due to the different pore structures of H-ZSM-5 and H-ZSM-22.

Microkinetic models are uniquely fit to investigate the kinetics of surface reactions such as those inside zeolite pores.²¹ The results from these models can provide quantitative and qualitative understanding of the catalyzed reactions as well as help describe the influence of reaction conditions on elementary reaction rates.^{21,22} In a report on ethanol dehydration over H-ZSM-5, Alexopoulos *et al.* constructed a microkinetic model to investigate the corresponding reaction network and impact of reaction temperature.²² Using periodic DFT, the thermodynamic and kinetic parameters were computed for all elementary steps which were then used to construct the model. They found ethene production at temperatures above 500 K occurred via a different pathway than at lower temperatures.²² In the work outlined in this chapter, we will use periodic DFT to build a microkinetic model for the isomerization of alkyl-substituted cyclopentenyl cations in H-ZSM-5 and H-ZSM-22 zeolites. We will make qualitative and quantitative comparisons and highlight significant differences in activation energy and rates of formation in the two zeolites.

Several techniques have been used to determine complex reaction mechanisms occurring in zeolite pores. Determining which technique to use depends on the amount of information that is available beforehand. For instance, iterative approaches can provide detailed reaction mechanisms with an expansive set of elementary reaction but require a large set of energetic and mechanistic data *a priori*.²³ In cases such as the isomerization of alkyl-substituted cyclopentenyls, the data available is rather minimal and a reaction generation code is more fitting. To this end, reaction network generation, via codes such

as the Rule Input Network Generator (RING), has been employed in the study of olefin cracking mechanisms over H-ZSM-5 zeolites.²⁴ In this work, we utilized RING to determine the possible mechanisms by which alkyl-substituted cyclopentenyl cations isomerize to give the more thermodynamically stable isomers. Specifically, we implemented constraints and rules corresponding to the system of interest and obtained an array of elementary steps and pathways which make up a larger reaction network associated with isomerization. The resulting pathways and reaction networks were used to investigate the thermodynamics and kinetics of cyclopentenyl isomerization in medium pore zeolites in an effort to determine the impact of the zeolite framework.

4.2 Methods

4.2.1 Rule Input Network Generator Protocol

Rule Input Network Generator (RING) was employed to determine the possible reaction pathways connecting the initial reactant isomer **A** to experimentally relevant alkyl-substituted cyclopentenyl cations (**T1**, **T2**, **T3**, **K1**, and **K2**), as shown in Figure 4.1. The RING code is composed of three components: (1) a molecular representation system that is used for all molecules (reactants, products, and intermediates); (2) a scheme for describing reaction rules unambiguously; and (3) a network generator that manages the construction of the reaction network based on the reaction rules. The code requires a set of initial reactants, a subset of elementary reaction steps as reaction rules, and a set of user-defined constraints as input. Three rules were defined which represented a hydride shift, alkyl shift, and double bond shift. The double bond shift is a way to describe the switching between resonance structures through movement of the double

bond.

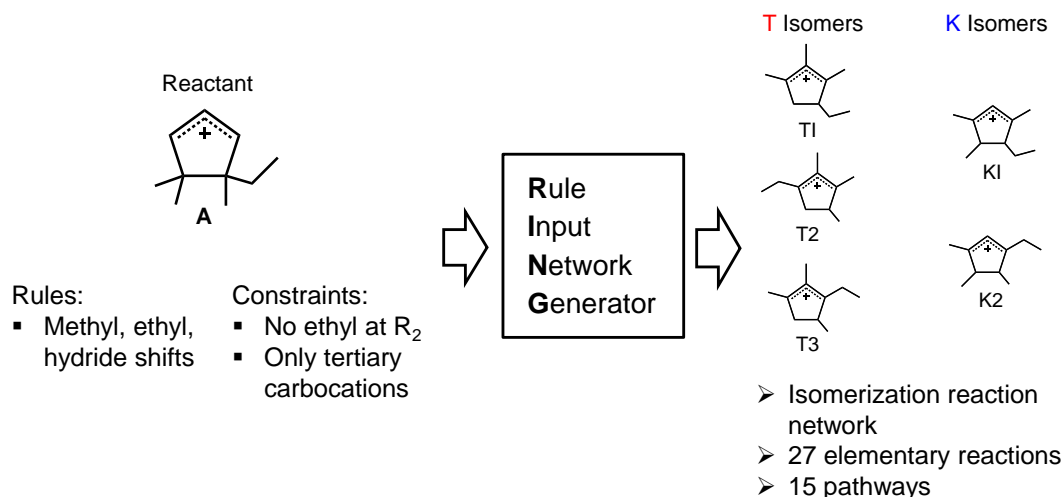


Figure 4.1 Scheme outlining the protocol used in the Rule Input Network Generator (RING) code. Input for the code included the reactant **A**, rules corresponding to methyl, ethyl, and hydride shifts, and constraints limiting high energy intermediates. The output was an isomerization reaction network made up of 15 pathways constituting 27 elementary reactions and resulting in two types of alkyl-substituted cyclopentenyl cations labeled **T** and **K**-type isomers.

Two sets of constraints were imposed on the code, the first for the formation of intermediates and the second for the formation of products. Intermediates were constrained to only be tertiary carbocations. Secondary and primary carbocations were not allowed to exist in any of the steps to avoid the formation of high energy intermediates (>50 kcal/mol) determined by preliminary geometry optimization calculations. The default constraint which disallows intramolecular reactions was removed since we are interested in ring isomerization. When imposing constraints on product formation, we took into account three types of products: (1) a fully substituted allylic system, (2) a di-substituted allylic system with a hydrogen on the center carbon, and (3) a fully substituted allylic system with an ethyl on the center carbon. The first and second constraints represent the formation of **T** and **K** type isomers, respectively. The third constraint disallows formation of a cyclopentenyl isomer with an ethyl group

substitution at the center allylic ring carbon. Previous NMR work¹ reported that isomers with bulky center allylic substitution do not form in the zeolite. The RING protocol yielded 27 elementary intramolecular isomerizations that were organized into 15 pathways yielding the **T** and **K** type isomers. We discuss the findings from RING in detail in Section 4.3.1.

4.2.2 Modeling the Zeolite

Zeolite unit cells were obtained from the Structure Commission of the International Zeolite Association.^{12,25} Previously optimized unit cell parameters for ZSM-5,²⁶ and ZSM-22²⁷ were used for all periodic DFT calculations. To avoid interaction of guest molecules in adjacent cells, the unit cell of ZSM-22 was expanded in the *c*-direction, creating a $1 \times 1 \times 3$ supercell. One acid site was introduced into each of the zeolite models by substituting one Al atom into a framework tetrahedral site, which was balanced by a proton. An Al atom was substituted into the ZSM-5 framework at T12 (at the sinusoidal and straight channel intersection) based on previous studies that indicate high accessibility to bulky hydrocarbons.^{26,28–30} The H-ZSM-5 unit cell composition was $\text{HAlSi}_{95}\text{O}_{192}$. For H-ZSM-22, a single Al atom was substituted into the super cell at T1, creating a super cell composition of $\text{HAlSi}_{71}\text{O}_{144}$. The T1 site was chosen because of its accessibility, while the literature^{31–35} is inconclusive regarding placement of aluminum in TON.

4.2.3 Electronic Structure Calculations

CP2K software was used for periodic DFT calculations of zeolite–guest systems, allowing ab initio molecular dynamics, geometry optimizations, and normal mode

analyses (NMA). We used periodic DFT within the generalized gradient approximation with the PBE exchange-correlation functional as implemented in CP2K.³⁶ The commonly used hybrid functional, B3LYP, is not available within CP2K and therefore limited us to the PBE functional. However, we have shown in our previous works that PBE functional provides adequate energy differences between cyclopentenyl cation isomers and is well-suited for this study.¹⁵ Corrections by Grimme *et al.* (DFT-D3) are used to take into account dispersion forces and obtain more accurate energetics.³⁷ For core electrons, Goedecker-Teter-Hutter norm-conserving pseudopotentials optimized for the PBE functional are used,³⁸ while the valence electron wavefunctions are expanded in terms of a triple- ζ valence polarized basis set (TZVP) comparable to 6-311G(d).³⁹ Within the CP2K scheme,³⁶ the electron density is described using an auxiliary plane-wave basis set with a 400 Ry cutoff.

4.2.4 Free Energy Calculations

This work required the computation of reaction and transition state free energies for all elementary reactions. In theory, this can be accomplished by either the correction of bare electronic energies via a harmonic approximation and normal modes, or direct calculation using an advanced sampling technique. Due to the number of elementary reactions and the generally larger computation cost of advanced sampling, we implemented a coupled advanced sampling/harmonic approximation approach for computing free energies. For each elementary reaction, we employed a protocol which included multiple steps: (1) we obtained initial geometries for the reactant and product states, using advanced sampling; (2) we computed fully optimized geometries and electronic energies associated with all critical points (reactant, product, and transition

state); (3) we computed normal modes at each critical point and confirmed the imaginary frequency in the transition state corresponding to the reaction coordinate; and (5) we corrected bare electronic energies to Helmholtz energies. The details of these steps are outlined below.

The first two steps in the scheme outlined above correspond to the computation of the zero-Kelvin minimum energy pathway. Climbing Image-Nudged Elastic Band (CINEB) was used to compute the minimum energy pathway for each elementary step. The CINEB calculations require reactant and product geometries as input, that are then connected by the computed pathway. To maximize efficiency in the CINEB calculation, these geometries should be very similar in structure with the majority of difference occurring at the point of the molecule where the reaction is taking place. For the hydride shifts, this was accomplished manually, whereas for the alkyl shifts, we used advanced sampling to help obtain the endpoint geometries. Hydride shift CINEB input were computed by first fully optimizing one endpoint (reactant or product), then manually moving the hydrogen associated with the hydride shift, and fully optimizing to yield the opposite endpoint. In the case of an alkyl shift, due to the many-body movement of the reaction, we incorporated an advanced sampling technique to obtain the initial CINEB endpoints. Specifically, we first utilized metadynamics, with a coordination number as the collective variable, to facilitate the alkyl shift giving us access to a transition region geometry. That geometry was then manually nudged along the apparent reaction coordinate, in both directions, and the geometries were fully optimized yielding, on one side the reactant, and on the other side the product. These optimized geometries were then used as input for the CINEB calculation.

After obtaining critical point geometries and energies, we computed the normal modes for each via a vibrational analysis within CP2K. All transition states were analyzed to ensure the presence of a single imaginary frequency that is associated with the reaction coordinate. Further confirmation of the transition state was conducted using visualization of the normal mode and steepest descent calculations. The frequencies of the normal modes were used to bring the bare electronic energies to Helmholtz free energies via a multi-dimensional harmonic oscillator model using Equation (4.1).

$$A = U + \sum_{N=1}^{\# \text{ of modes}} \frac{\hbar\omega_N}{2} + \sum_{N=1}^{\# \text{ of modes}} \ln \left(1 - e^{-\frac{\hbar\omega_N}{k_B T}} \right) \quad (\text{Eq 4.1})$$

4.2.5 Kinetic Model

The Helmholtz energies for all elementary reactions were used to build a microkinetic model of the isomerization of alkyl-substituted cyclopentenyl cations in H-ZSM-5 and H-ZSM-22. Energies obtained using the scheme described above were used to compute forward and backward rate constants which were then incorporated into a system of rate equations. Forward rate constants were computed using transition state theory formalism:

$$k_{TST} = \frac{k_b T}{h} \exp \left(-\frac{\Delta A^\ddagger}{k_b T} \right) \quad (\text{Eq 4.2})$$

Where k_b is the Boltzmann constant, h is the Planck constant, and ΔA^\ddagger is Helmholtz free energy of activation. Reverse rate constants were computed via detailed balanced using explicitly the Helmholtz free energies computed using Equation (4.1).

4.3 Results

4.3.1 Alkyl-substituted cyclopentenyl cation isomerization reaction network

Alkyl-substituted cyclopentenyl cations form from alkatriene precursor molecules in homogeneous and heterogeneous acid media.^{7,15,40} Such processes require several steps of cyclization and isomerization to give experimentally observed alkyl-substituted cyclopentenyl cations.^{7,15} It has been previously reported that cyclization of the alkatriene results in a high energy cyclopentenyl cation which can subsequently isomerize to give more stable alkyl-substituted cyclopentenyl cations.⁷ The mechanism by which post-cyclization isomerization occurs, however, has not been adequately studied. We used a network generator to determine a reaction network associated with isomerization of alkyl-substituted cyclopentenyl cations, we report on those results in this section.

We implemented the Rule Input Network Generator (RING) code to determine the possible pathways connecting the starting cyclopentenyl isomer, **A**, to five distinct products (**T1**, **T2**, **T3**, **K1**, **K2**). Determining the possible pathways for an isomerization of this nature presents a combinatorial problem which at the outset may yield up to nearly 1000 different mechanisms. To circumvent this issue, RING incorporates constraints and rules as initial input making the task more tractable. In our case, RING yielded a reaction network made up of 24 isomers, 27 unique elementary reactions, and 15 separate pathways connecting reactant **A** to the five products mentioned above. The pathways lead to two sets of isomers which we label as **T**-type and **K**-type. The **T**-type isomers (**T1**, **T2**, and **T3**) are cyclopentenyl cations with a methyl substitution at the center allylic carbon, which has been previously determined to be the more thermodynamically stable isomer.¹⁵ The **K**-type isomers (**K1** and **K2**) have a hydrogen substitution at the center allylic

carbon. As seen in the reaction network illustrated in Figure 4.2, the **K**-type isomers are intermediates in the reaction network, while the **T**-type isomers are products where the reaction can terminate.

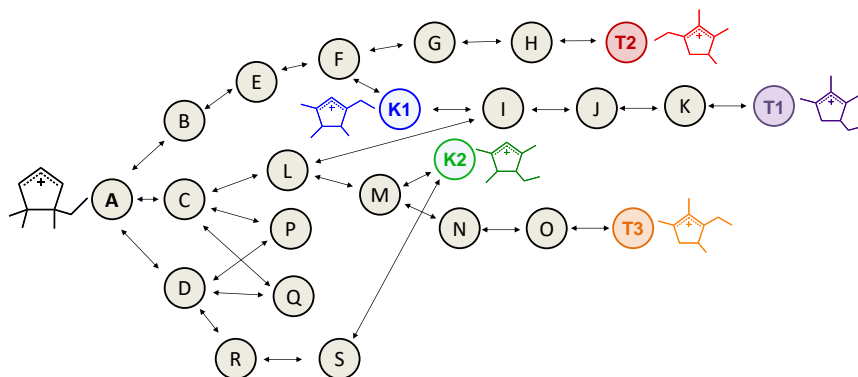


Figure 4.2 Cyclopentenyl cation isomerization reaction network obtained from RING. The network is made up of 15 pathways and 24 unique isomers. The reaction includes two K-type isomers, K1 and K2, and three T-type isomers, T1, T2, and T3.

The pathways from RING were combined to form an isomerization reaction network and are made up of four types of elementary reactions; (1) resonance breaking, (2) resonance forming, (3) alkyl shifts, and (4) hydride shifts. Figure 4.3 shows an example of an elementary reaction, an ethyl shift, obtained from RING. The reaction going forward breaks the resonance in the allylic system, forming a local carbocation, while the reverse reestablishes resonance. The former is generally an endothermic reaction whereas the latter is exothermic. Hydride shifts occurred in a similar manner.

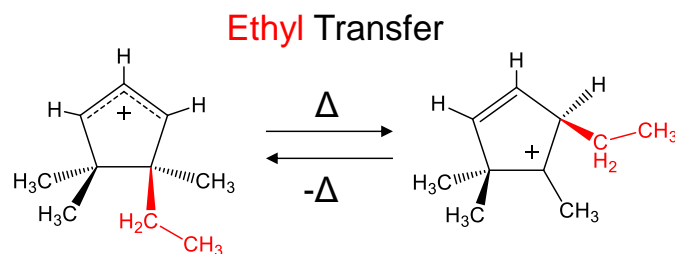


Figure 4.3 An example of an elementary step obtained from RING. An ethyl transfer which breaks the resonance and forms a local carbocation. In general, reactions in which resonance is broken are endothermic, whereas those which resonance is reestablished are exothermic.

In the following sections we will discuss first, the free energetics associated with these elementary steps and pathways (Section 4.3.2), and second, the results from solving a microkinetic model based on this reaction network and the impact of the different pore structures in H-ZSM-5 and H-ZSM-22 (Section 4.3.3).

4.3.2 Eight-step reaction pathway with a T-type isomer as a product and a K-type isomer as an intermediate.

We begin our analysis of cyclopentenyl cation isomerization in zeolites by considering a single pathway extracted from the reaction network found by RING. The pathway starts from reactant isomer **A** and ends at the **T2** isomer with **K1** as an intermediate. It consists of nine total cyclopentenyl isomers and eight barriers. We will use this pathway to illustrate: (1) the computation of a free energy barrier with the metadynamics/CINEB protocol, and (2) the free energies of isomerization elementary steps.

The eight-step pathway is a combination of resonance breaking and forming reactions as well as methyl, ethyl, and hydride shifts. We computed reaction and transition state free energies for these many-body reactions by incorporating a combined finite temperature and zero-Kelvin protocol. Specifically, Helmholtz energy barriers were

computed using a coupled metadynamics and climbing image-nudged elastic band (CINEB) scheme; metadynamics was used to obtain endpoint geometries for input in CINEB calculations which give reaction and transition state energies. To illustrate this process, consider the ethyl shift from isomer II to isomer III shown in Figure 4.4. The ethyl group begins at C4 position on the ring and then transfers to the C5 position. Using metadynamics, incorporated with a collective variable defined by the coordination numbers of the C3 and C4 carbons, we facilitated the ethyl shift via the addition of a bias potential.⁴¹ From the resulting dynamics we extracted a geometry from the transition region of the free energy surface, as shown in Figure 4.4. In this geometry, the ethyl group is nearly equidistant between C3 and C4 ring carbons (~2.0 Angstroms). Next, using this geometry, we conducted a full geometry optimization in which the molecule relaxed to isomer II. That provided us with the starting endpoint for the CINEB run. To obtain the other endpoint (isomer III), we began again with the transition region geometry and simply nudged the ethyl in the opposite direction (to the right in this case) along the apparent reaction coordinate. Once again, we conducted a geometry optimization which gave the geometry for isomer III. We used both geometries as input and conducted a CINEB calculation which yielded the reaction energy, transition state, and activation energy. The utilization of this protocol ensures that most of the molecular change occurs only at location of the ethyl shift, a requirement for an efficient CINEB calculation. This scheme was used for alkyl shifts, but not for hydrogen shifts. The endpoints for a hydrogen shift, which requires fewer atoms to move, were determined a priori without a facilitated transition using metadynamics.

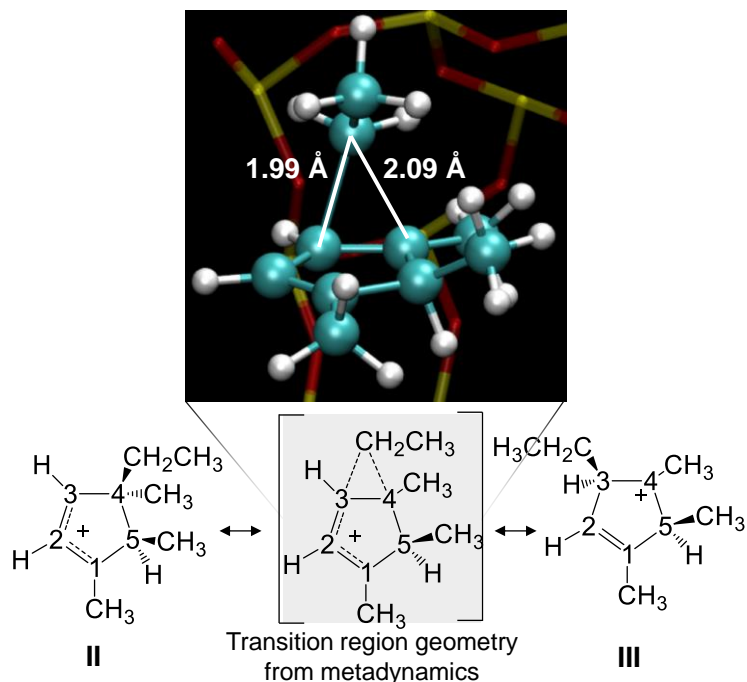


Figure 4.4 Transition state region geometry extracted from metadynamics simulation. The geometry was used to obtain initial input for CINEB calculations. Note: the structure pictured here is not geometry optimized.

Figure 4.5 shows the Helmholtz free energy surface for the eight-step pathway at 200 °C in H-ZSM-5. The free energy surface includes the **K1** isomer (shown in blue) as a low energy intermediate and the **T2** isomer (shown in red) as the final product and most stable isomer. There are four intermediates which correspond to the isomers where resonance is established (**II**, **K1**, **V**, and **T2**) and four which have a local carbocation, and are generally higher in free energy (**I**, **III**, **IV**, and **VI**). Due to our modular approach; computing elementary step reaction energies separately and combining them in the respective pathways, the zeolite-guest systems associated with the intermediates have differences in the associated energies and geometries. We address this by employing an averaging of common intermediate free energies to ensure thermodynamic consistency. The error bars associated with this averaging scheme are reported in the free energy surface. We found that on average the error was 1.0 and 1.3 kcal/mol for H-ZSM-5 and

H-ZSM-22, respectively. Overall, these reaction pathways give insight into the intricate reaction energies that make up the isomerization network in both zeolites. The essence of this work, however, is not comparing single pathways since they do not exist on their own, instead in the following section we combine all of the pathways and consider the entire reaction network and ultimately determine the extent of kinetic control.

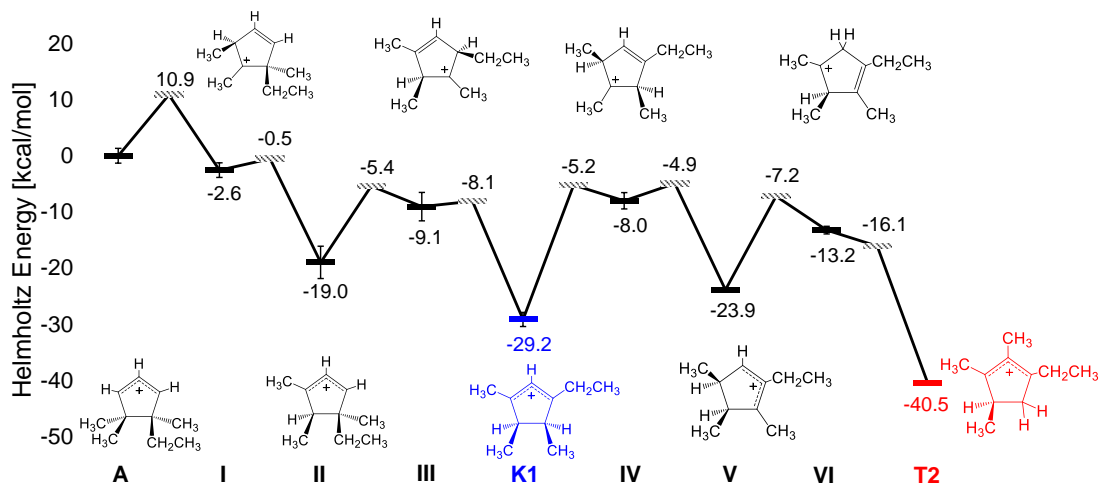


Figure 4.5 Helmholtz free energy surface for one of the 15 pathways obtained from RING in H-ZSM-5 at 200 °C. Pathway begins at reactant isomer A and terminates at the T2 isomer with K1 as an intermediate. The local minima are shown using solid bars while transition states are shown using dashed bars. Errors associated with averaging scheme outlined in the text are also shown. All energies are reported in kcal/mol.

4.3.3 Alkyl-substituted cyclopentenyl cation isomerization reaction network in H-ZSM-5 and H-ZSM-22.

We now consider the kinetics associated with the cyclopentenyl isomerization reaction network that was obtained from the RING calculations. The free energies from the protocol described in the previous section were used to compute forward and backward rate constants for each elementary step in the reaction network. These were then incorporated into a microkinetic model representing the isomerization reaction network.

Figure 4.6 shows formation plots in H-ZSM-5 and H-ZSM-22 zeolites obtained using the microkinetic model. The concentrations are plotted versus time to include the experimentally relevant time window of 10^4 - 10^5 seconds, or up to ~ 3 hours of reaction time.^{15,40} There are notable similarities and differences between the two zeolites. For instance, in both zeolites, only **T**-type isomers are formed at equilibrium. **K**-type isomers form at earlier times, but then are completely depleted before the experimental time window. A difference between the zeolites is the set of isomers that form, based on the model. In H-ZSM-5, three of the five isomers (**T1**, **T2**, and **K1**) form while in H-ZSM-22 a different set of isomers form (**T2**, **T3** and **K2**). It is important to note that isomers not appearing in the plot, form in the zeolites according to our model, but at a very small concentrations ($<10^{-4}$) and therefore do not show up in the graphs. Also, at equilibrium H-ZSM-5 has only a single isomer formed (**T2**) whereas in H-ZSM-22, there are two equilibrium isomers (**T2** and **T3**).

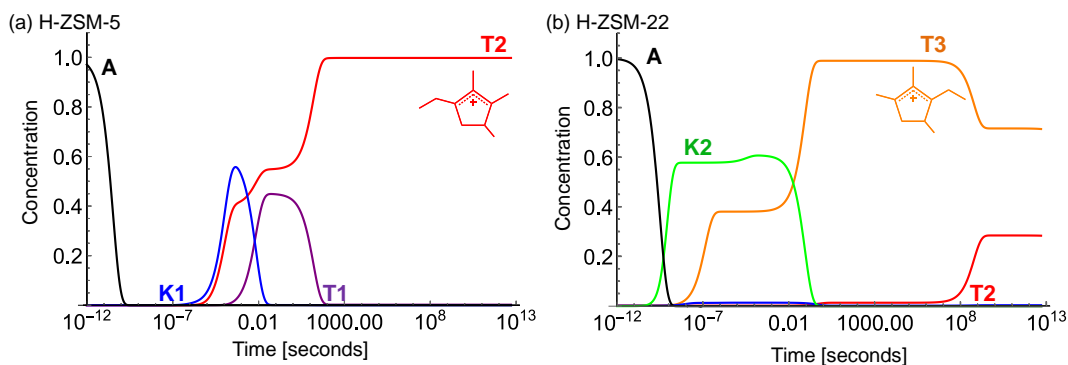


Figure 4.6 Concentration plots for T and K-type isomers obtained by constructing microkinetic model for cyclopentenyl isomerization in (a) H-ZSM-5 and (b) H-ZSM-22.

Recall from the table (Table 4.1) presented in the Introduction of this chapter that the relative stabilities of the isomers differ in the two zeolites. In H-ZSM-5, **T2** is the most thermodynamically stable (-40.5 kcal/mol) and the second most stable isomer, **T1** (-

34.8 kcal/mol), is higher in energy by $\Delta A = 5.7$ kcal/mol. The kinetics shows that **T1** forms during earlier stages of the reaction, but fully disappears at $t \sim 1000$ s giving rise to full population of **T2**. For H-ZSM-22, consider that the most stable isomer is **T3** (-52.2 kcal/mol), however **T2** (-51.3 kcal/mol) is higher in energy by only $\Delta A = 0.9$ kcal/mol. This difference in energy estimates an equilibrium distribution (via Boltzmann factor) for **T2:T3** of 0.40. When we consider the kinetic results in Figure 4.6B we find that at very long times the distribution ratio of **T2:T3** is 0.29/0.71 or simply 0.41, in very close agreement with the prediction from the thermodynamics. More interestingly, this equilibrium distribution is only achieved in H-ZSM-22 after an astonishing $\sim 10^8$ seconds of reaction time, or 3 years! This would suggest that the isomerization in H-ZSM-22 is under kinetic control, and only after very long time is thermodynamic control achieved. This begs the question: *What is the rate-limiting process responsible for kinetic control during isomerization in H-ZSM-22?*

The elementary steps, and corresponding pathways, that make up the isomerization reaction network provide insight on the question above. Specifically, we considered two pathways by which the **T3** isomer could back-react to give rise to **T2** during the later stages of the reaction. Interestingly, we found that these two pathways need to be simultaneously active for the formation of **T2** to occur. If one of them is turned off, **T2** formation does not occur, even after very long reaction time. Moreover, these two pathways share a common intermediate after which there is a branch point (See Figure 4.7). At that point, the reaction can either go through elementary step 9, an ethyl shift, or backward through elementary step 8, a hydride shift. The impact on the overall product formation was tested by considering artificial changes to the transition state

energy for both steps. In the case of step 8, reducing the energy of the transition state, or lowering the backward barrier, by 30% did not result in any change in the product formation. In contrast, when we applied the same 30% reduction to the transition state for step 9, we found changes occurring in product formation. Namely, the time it takes for thermodynamic equilibrium to take over was decreased from 10^8 seconds to 10^6 seconds. This suggests that elementary step 9 is a rate-limiting step in the isomerization network and its barrier can be used to tune the thermodynamic and kinetic control of product formation.

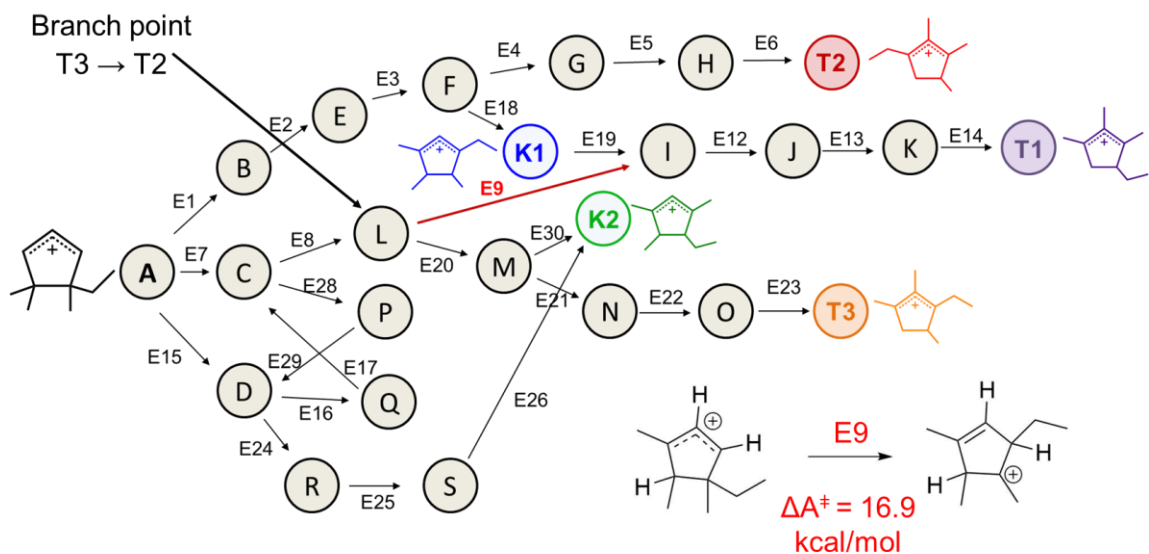


Figure 4.7 Isomerization reaction network with highlighted branch point during the back reaction from **T3** to **T2**. The forward E9 reaction, shown in red, was determined to be rate-limiting in H-ZSM-22. Also reported is the activation free energy for the reaction in H-ZSM-22 of 16.9 kcal/mol.

It is also worth noting that the barrier of this alkyl shift is 16.9 kcal/mol (Figure 4.7) which is similar to many other alkyl (and hydride) shifts in the network. In other words, there is no significance in the barrier height for this elementary step even though it proves to be rate limiting and responsible for holding the reaction under kinetic control. These findings then indicate that simply comparing the free energies would not be

sufficient in determine the rate-limiting step, as is done in previous studies addressing similar questions of kinetic and thermodynamic control. Rather, the microkinetic model is needed to be able to identify which specific steps in the reaction network, or pathway, are controlling the product formation.

4.4 Conclusions

We performed periodic density functional theory (DFT) calculations to study the isomerization of alkyl-substituted cyclopentenyl cations in medium pore acid zeolites, H-ZSM-5 and H-ZSM-22. In particular, we considered the isomerization of a 4-ethyl-4,5,5-trimethylcyclopentenyl cation (**A**), a hypothesized product of cyclization from protonated acyclic trienes. Our previous computational work, in collaboration with experiment, found that cyclization of protonated acyclic trienes leads to cyclopentenyl cation product distributions that are controlled by the pore structure and contrary to DFT-predicted thermodynamics. For this reason, this current work focused on the post-cyclization isomerization to determine the impact of confinement on the formation of the thermodynamically favored products. We considered isomerization from **A** to two types of isomers labeled as **T** and **K** isomers, which differ in the allylic substitution pattern on the ring. **T** isomers have a methyl as the center allylic substituent while **K** isomers, have a hydrogen. The reaction network by which this isomerization occurs was determined by using a Rule Input Network Generator (RING). The RING software uses organic chemistry concepts coupled with user-defined rules and constraints to provide pathways from a reactant molecule to desired products. We incorporated this software with a set of constraints to avoid high-energy intermediates and yielded a total of 15 pathways leading to five distinct isomers; three **T**-type and two **K**-type isomers. We found that the

pathways were made up of 27 unique alkyl and hydride elementary steps. The 15 pathways were combined to produce a single reaction network starting from reactant **A** and leading to **K**-type isomers as intermediates and **T**-type isomers as products where the reaction network terminates.

We used a combined finite temperature and zero-Kelvin protocol to compute elementary step barriers; finite temperature metadynamics was used to obtain endpoints which were used as initial input for Climbing Image-Nudged Elastic Band (CINEB) calculations for the computation of reaction and transition state energies. For a given elementary step, we first used metadynamics to facilitate the reaction, then extracted a transition region geometry, and finally optimized to yield the corresponding endpoints. The reaction barrier between the two endpoints was then computed using CINEB. The protocol captured the subtle changes in the molecule and zeolite away from the main reaction. The corrected Helmholtz free energies for all elementary steps were incorporated into the 15 pathways in H-ZSM-5 and H-ZSM-22.

We built a microkinetic model to study the equilibrium product distribution for isomerization. The free energy barriers for each elementary step were used to compute forward rate constants via the transition state theory formalism. Backward rate constants were computed by incorporating detailed balance. We constructed a system of 24 rate equations corresponding to all species in the isomerization reaction network. The resulting concentrations as a function of time were plotted to include the experimental time window of $10^4 - 10^5$ seconds. We found that at equilibrium the major products in the two zeolites consisted of only **T**-type products but differed in the specific isomers that were present. In H-ZSM-5, our model predicts the formation of only the **T2** isomer. In

contrast, in H-ZSM-22, a mixture of **T2** and **T3** isomers forms at equilibrium with a ratio that is in very good agreement with what was predicted by the thermodynamics. The equilibrium mixture of the two isomers was only achieved after very long reaction time ($\sim 10^8$ seconds) suggesting that the isomerization in H-ZSM-22 may be under kinetic control at shorter reaction times which include the experimental time window. More notably, our model was able to pinpoint the specific ethyl shift elementary reaction in H-ZSM-22 that is rate-limiting and responsible for holding the system under kinetic control.

4.5 References

- (1) Haw, J. F.; Nicholas, J. B.; Song, W.; Deng, F.; Wang, Z.; Xu, T.; Heneghan, C. S. Roles for Cyclopentenyl Cations in the Synthesis of Hydrocarbons from Methanol on Zeolite Catalyst HZSM-5. **2000**, No. 20, 4763–4775. <https://doi.org/10.1021/ja994103x>.
- (2) Wang, S.; Chen, Y.; Qin, Z.; Zhao, T.-S.; Fan, S.; Dong, M.; Li, J.; Fan, W.; Wang, J. Origin and Evolution of the Initial Hydrocarbon Pool Intermediates in the Transition Period for the Conversion of Methanol to Olefins over H-ZSM-5 Zeolite. *J. Catal.* **2019**, *369*, 382–395. <https://doi.org/10.1016/j.jcat.2018.11.018>.
- (3) Wulfers, M. J.; Jentoft, F. C. The Role of Cyclopentadienium Ions in Methanol-to-Hydrocarbons Chemistry. *ACS Catal.* **2014**, *4* (10), 3521–3532. <https://doi.org/10.1021/cs500722m>.
- (4) Haw, J. F.; Song, W.; Marcus, D. M.; Nicholas, J. B. The Mechanism of Methanol to Hydrocarbon Catalysis. *Acc. Chem. Res.* **2003**, *36* (5), 317–326. <https://doi.org/10.1021/ar020006o>.
- (5) Zhang, W.; Zhi, Y.; Huang, J.; Wu, X.; Zeng, S.; Xu, S.; Zheng, A.; Wei, Y.; Liu, Z. Methanol to Olefins Reaction Route Based on Methylcyclopentadienes as Critical Intermediates. *ACS Catal.* **2019**, *9* (8), 7373–7379. <https://doi.org/10.1021/acscatal.9b02487>.
- (6) Zhang, W.; Zhang, M.; Xu, S.; Gao, S.; Wei, Y.; Liu, Z. Methylcyclopentenyl Cations Linking Initial Stage and Highly Efficient Stage in Methanol-to-Hydrocarbon Process. *ACS Catal.* **2020**, *10* (8), 4510–4516. <https://doi.org/10.1021/acscatal.0c00799>.
- (7) Sorensen, T. S. The Synthesis and Reactions of Divinyl Carbonium Ions. *Can. J. Chem.* **1964**, *42* (12), 2768–2780. <https://doi.org/10.1139/v64-410>.
- (8) Sorensen, T. S. Directly Observable Carbonium Ion-Carbonium Ion Rearrangements. I. Kinetics and Equilibria in the Interconversion of Trialkylcyclopentenyl Cations. *J. Am. Chem. Soc.* **1967**, *89* (15), 3782–3794. <https://doi.org/10.1021/ja00991a019>.
- (9) Deno, N. C.; Richey, H. G.; Friedman, N.; Hodge, J. D.; Houser, J. J.; Pittman, C. U. Carbonium Ions. XI. Nuclear Magnetic Resonance Spectra of the Aliphatic Alkenyl Cations. *J. Am. Chem. Soc.* **1963**, *85* (19), 2991–2995.
- (10) Deno, N. C.; Friedman, N.; Hodge, J. D.; Houser, J. J. Carbonium Ions. XII. The Direct Observation of Rearrangement and Hydrogen-Deuterium Exchange in Cycloalkenyl Cations. *J. Am. Chem. Soc.* **1963**, *85* (19), 2995–2997.
- (11) Baerlocher, C.; McCusker, L. B. International Zeolite Association: Database of Zeolite Structures.
- (12) Baerlocher, C.; McCusker, L. B.; Olson, D. H. *Atlas of Zeolite Framework Types*, Sixth Edit.; Elsevier Science B.V.: Amsterdam, 2007.
- (13) Unni, O.; Stian, S.; Morten, B.; Pablo, B.; W., J. T. V.; Finn, J.; Silvia, B.; Petter, L. K. Conversion

- of Methanol to Hydrocarbons: How Zeolite Cavity and Pore Size Controls Product Selectivity. *Angew. Chemie Int. Ed.* **2012**, *51* (24), 5810–5831. <https://doi.org/10.1002/anie.201103657>.
- (14) Teketel, S.; Svelle, S.; Lillerud, K.-P.; Olsbye, U. Shape-Selective Conversion of Methanol to Hydrocarbons Over 10-Ring Unidirectional-Channel Acidic H-ZSM-22. *ChemCatChem* **2009**, *1* (1), 78–81. <https://doi.org/https://doi.org/10.1002/cctc.200900057>.
 - (15) Hernandez, E. D.; Manookian, B.; Auerbach, S. M.; Jentoft, F. C. Shape-Selective Synthesis of Alkylcyclopentenyl Cations in Zeolites and Spectroscopic Distinction of Constitutional Isomers. *ACS Catal.* **2021**, *11* (21), 12893–12914. <https://doi.org/10.1021/acscatal.1c03039>.
 - (16) Kumar, R.; Ratnasamy, P. Isomerization and Formation of Xylenes over ZSM-22 and ZSM-23 Zeolites. *J. Catal.* **1989**, *116* (2), 440–448. [https://doi.org/https://doi.org/10.1016/0021-9517\(89\)90110-3](https://doi.org/https://doi.org/10.1016/0021-9517(89)90110-3).
 - (17) Sugi, Y.; Vinu, A. Alkylation of Biphenyl over Zeolites: Shape-Selective Catalysis in Zeolite Channels. *Catal. Surv. from Asia* **2015**, *19* (3), 188–200. <https://doi.org/10.1007/s10563-015-9193-3>.
 - (18) Poursaeidesfahani, A.; de Lange, M. F.; Khodadadian, F.; Dubbeldam, D.; Rigutto, M.; Nair, N.; Vlucht, T. J. H. Product Shape Selectivity of MFI-Type, MEL-Type, and BEA-Type Zeolites in the Catalytic Hydroconversion of Heptane. *J. Catal.* **2017**, *353*, 54–62. <https://doi.org/https://doi.org/10.1016/j.jcat.2017.07.005>.
 - (19) Smit, B.; Maesen, T. L. M. Towards a Molecular Understanding of Shape Selectivity. *Nature* **2008**, *451* (7179), 671–678. <https://doi.org/10.1038/nature06552>.
 - (20) Chen, Y.-Y.; Wei, Z.; Wang, S.; Li, J.; Dong, M.; Qin, Z.; Wang, J.; Jiao, H.; Fan, W. Kinetics and Thermodynamics of Polymethylbenzene Formation over Zeolites with Different Pore Sizes for Understanding the Mechanisms of Methanol to Olefin Conversion – a Computational Study. *Catal. Sci. Technol.* **2016**, *6* (14), 5326–5335. <https://doi.org/10.1039/C6CY00465B>.
 - (21) Reyniers, M.-F.; Marin, G. B. Experimental and Theoretical Methods in Kinetic Studies of Heterogeneously Catalyzed Reactions. *Annu. Rev. Chem. Biomol. Eng.* **2014**, *5* (1), 563–594. <https://doi.org/10.1146/annurev-chembioeng-060713-040032>.
 - (22) Alexopoulos, K.; John, M.; Van der Borgh, K.; Galvita, V.; Reyniers, M.-F.; Marin, G. B. DFT-Based Microkinetic Modeling of Ethanol Dehydration in H-ZSM-5. *J. Catal.* **2016**, *339*, 173–185. <https://doi.org/https://doi.org/10.1016/j.jcat.2016.04.020>.
 - (23) Motagamwala, A. H.; Dumesic, J. A. Microkinetic Modeling: A Tool for Rational Catalyst Design. *Chem. Rev.* **2021**, *121* (2), 1049–1076. <https://doi.org/10.1021/acs.chemrev.0c00394>.
 - (24) Chen, C.-J.; Rangarajan, S.; Hill, I. M.; Bhan, A. Kinetics and Thermochemistry of C4–C6 Olefin Cracking on H-ZSM-5. *ACS Catal.* **2014**, *4* (7), 2319–2327. <https://doi.org/10.1021/cs500119n>.
 - (25) Baerlocher, C.; McCusker, L. B. International Zeolite Association: Database of Zeolite Structures.
 - (26) Alexopoulos, K.; Lee, M. S.; Liu, Y.; Zhi, Y.; Liu, Y.; Reyniers, M. F.; Marin, G. B.; Glezakou, V. A.; Rousseau, R.; Lercher, J. A. Anharmonicity and Confinement in Zeolites: Structure, Spectroscopy, and Adsorption Free Energy of Ethanol in H-ZSM-5. *J. Phys. Chem. C* **2016**, *120* (13), 7172–7182. <https://doi.org/10.1021/acs.jpcc.6b00923>.
 - (27) Moses, P. G.; Nørskov, J. K. Methanol to Dimethyl Ether over ZSM-22: A Periodic Density Functional Theory Study. *ACS Catal.* **2013**, *3* (4), 735–745. <https://doi.org/10.1021/cs300722w>.
 - (28) Brändle, M.; Sauer, J. Acidity Differences between Inorganic Solids Induced by Their Framework Structure. A Combined Quantum Mechanics/Molecular Mechanics Ab Initio Study on Zeolites. *J. Am. Chem. Soc.* **1998**, *120* (7), 1556–1570. <https://doi.org/10.1021/ja9729037>.
 - (29) De Moor, B. A.; Reyniers, M.-F.; Gobin, O. C.; Lercher, J. A.; Marin, G. B. Adsorption of C2–C8 N-Alkanes in Zeolites. *J. Phys. Chem. C* **2011**, *115* (4), 1204–1219. <https://doi.org/10.1021/jp106536m>.
 - (30) Nguyen, C. M.; Reyniers, M. F.; Marin, G. B. Theoretical Study of the Adsorption of the Butanol Isomers in H-ZSM-5. *J. Phys. Chem. C* **2011**, *115* (17), 8658–8669. <https://doi.org/10.1021/jp111698b>.
 - (31) Sklenak, S.; Dědecěk, J.; Li, C.; Gao, F.; Jansang, B.; Boekfa, B.; Wichterlova, B.; Sauer, J. Aluminum Siting in the ZSM-22 and Theta-1 Zeolites Revisited: A QM/MM Study. *Collect. Czechoslov. Chem. Commun.* **2008**, *73* (6–7), 909–920. <https://doi.org/10.1135/cccc20080909>.
 - (32) Chen, Z.; Liu, S.; Wang, H.; Ning, Q.; Zhang, H.; Yun, Y.; Ren, J.; Li, Y. W. Synthesis and Characterization of Bundle-Shaped ZSM-22 Zeolite via the Oriented Fusion of Nanorods and Its Enhanced Isomerization Performance. *J. Catal.* **2018**, *361*, 177–185.

- <https://doi.org/10.1016/j.jcat.2018.02.019>.
- (33) Derewinski, M.; Sarv, P.; Mifsud, A. Thermal Stability and Siting of Aluminum in Isostructural ZSM-22 and Theta-1 Zeolites. *Catal. Today* **2006**, *114* (2–3), 197–204. <https://doi.org/10.1016/j.cattod.2006.01.008>.
- (34) Nguyen, C. M.; Reyniers, M.-F.; Marin, G. B. Adsorption Thermodynamics of C1–C4 Alcohols in H-FAU, H-MOR, H-ZSM-5, and H-ZSM-22. *J. Catal.* **2015**, *322*, 91–103. <https://doi.org/10.1016/j.jcat.2014.11.013>.
- (35) Dědeček, J.; Sobalík, Z.; Wichterlová, B. Siting and Distribution of Framework Aluminium Atoms in Silicon-Rich Zeolites and Impact on Catalysis. *Catal. Rev. - Sci. Eng.* **2012**, *54* (2), 135–223. <https://doi.org/10.1080/01614940.2012.632662>.
- (36) VandeVondele, J.; Krack, M.; Mohamed, F.; Parrinello, M.; Chassaing, T.; Hutter, J. QUICKSTEP: Fast and Accurate Density Functional Calculations Using a Mixed Gaussian and Plane Waves Approach. *Comput. Phys. Commun.* **2005**, *167* (2), 103–128.
- (37) Grimme, S.; Antony, J.; Ehrlich, S.; Krieg, H. A Consistent and Accurate Ab Initio Parametrization of Density Functional Dispersion Correction (DFT-D) for the 94 Elements H-Pu. *J. Chem. Phys.* **2010**, *132* (15), 154104. <https://doi.org/10.1063/1.3382344>.
- (38) Goedecker, S.; Teter, M.; Hutter, J. Separable Dual-Space Gaussian Pseudopotentials. *Phys. Rev. B* **1996**, *54* (3), 1703–1710. <https://doi.org/10.1103/PhysRevB.54.1703>.
- (39) VandeVondele, J.; Hutter, J. Gaussian Basis Sets for Accurate Calculations on Molecular Systems in Gas and Condensed Phases. *J. Chem. Phys.* **2007**, *127* (11), 114105. <https://doi.org/10.1063/1.2770708>.
- (40) Hernandez, E. D.; Jentoft, F. C. Spectroscopic Signatures Reveal Cyclopentenyl Cation Contributions in Methanol-to-Olefins Catalysis. *ACS Catal.* **2020**, *10* (10), 5764–5782. <https://doi.org/10.1021/acscatal.0c00721>.
- (41) Ensing, B.; De Vivo, M.; Liu, Z.; Moore, P.; Klein, M. L. Metadynamics as a Tool for Exploring Free Energy Landscapes of Chemical Reactions. *Acc. Chem. Res.* **2006**, *39* (2), 73–81. <https://doi.org/10.1021/ar040198i>.

CHAPTER 5

CONCLUSIONS AND FUTURE WORK

In this chapter we will first provide concise summaries for all of the work described in detail above. Then, in section 5.2 we will provide our suggestions for future work.

5.1 Summaries of Conclusions

5.1.1 Molecular vibrations of acyclic olefins in zeolites and the magnitude of host-guest interactions

We performed experimental and periodic density functional theory (DFT) IR spectroscopy to investigate the adsorption of acyclic olefins over both acidic and non-acidic zeolites. Two conjugated polyenes, 2,4-dimethyl-1,3-pentadiene (**I**) and 2,6-dimethyl-2,4,6-octatriene (**II**) were studied to probe organic intermediates that can form during methanol conversion, and that can lead to deactivating species known collectively as “coke.” We computed vibrational spectra using zeolite-adsorbed and gas-phase models for both neutral and protonated forms of **I** and **II**, and compared these DFT results to diffuse reflectance IR Fourier transform (DRIFT) spectra of zeolite-guest systems obtained by our collaborators at UMass. Our computational results are precise enough to pinpoint that the gauche *s*-cis conformation of species **I** predominates during adsorption over de-aluminated zeolite beta. Computed zeolite-adsorbed spectra of the protonated species **I** and **II** best represent the DRIFT spectra obtained after the adsorption of the olefins on HMOR at 20 °C, with computed bands at 1543 and 1562 cm^{-1} for molecules **I**⁺ and **II**⁺, respectively, attributed to the allylic stretching mode, $\nu(\text{C}=\text{C}-\text{C}^+)$. These computed band frequencies are within 6 cm^{-1} of experimental data and confirm that the

interaction between neutral acyclic olefins and acidic zeolites leads to protonation of the olefin. Comparison of computed spectra of the protonated species in the gas phase to those in the zeolite indicates that the electrostatic interaction between alkenyl and alkadienyl cations and negative zeolite framework does not significantly impact the position of the allylic stretching bands. These results highlight that computed spectroscopy and thermodynamics coupled with experimental spectra can be used for elucidating complex mixtures in zeolites, and certain spectral features of adsorbed olefins can be accurately modeled by gas-phase calculations.

5.1.2 Shape-selectivity in medium pore zeolites during formation of cyclopentenyl cations

In collaboration with experimental researchers at UMass Amherst Chemical Engineering – E. Hernandez and F. Jentoft – we utilized periodic DFT models to investigate the formation of alkylcyclopentenyl cations in medium and large pore zeolites and the extent of shape-selectivity. During catalytic conversion of methanol on acidic zeolites, alkylcyclopentenyl cations are reported as active co-catalysts as a part of the “hydrocarbon pool” and more recently studies show they can act as precursors to larger polyaromatic species. We considered two types of alkylcyclopentenyl cations distinguished by the substituent at the central carbon (C-2) of the allylic system: a less thermodynamically stable type with a hydrogen at the C-2, and a more stable type with a methyl group at the C-2. We set out to achieve three main objectives: (1) distinguish the IR spectroscopic fingerprints associated with these two types of alkylcyclopentenyl cations; (2) determine the role of the zeolite pore structure on the formation of alkylcyclopentenyl cations from acyclic precursors; and (3) determine the

thermodynamics of cyclization in the zeolite and the gas-phase. Our experimental collaborators used UV–vis and IR spectroscopy in situ to characterize alkylcyclopentenyl cation formation from the acyclic precursor 2,6-dimethyl-2,4,6-octatriene in large (HMOR) and medium pore (HZSM-5 & HZSM-22) zeolites.

In combination with DFT-computed IR spectra, we found a characteristic red-shift of the asymmetric allylic stretching vibration of about -20 cm^{-1} when the C-2 carbon was substituted with a methyl group instead of a hydrogen. Using this knowledge, we investigated zeolite pore structure control on the allylic substitution pattern on the alkylcyclopentenyl cation during cyclization. We found that in the larger pore zeolite HMOR, cyclization led to a methyl-substituted C-2 whereas in the medium pore zeolites HZSM-5 and HZSM-22, cyclization gave rise to the hydrogen-substituted molecule, suggesting the presence of shape-selectivity. We used DFT-computed thermodynamics to further investigate the energetics of cyclization to alkylcyclopentenyl cations. In HMOR, we found that the methyl-substituted type was the more stable of the two, following what we expected based on the larger pore environment. In the medium pore zeolite cases, we found somewhat to our surprise that the thermodynamic favorability towards the methyl-substituted cyclopentenyl cations remained even though they were not forming in those zeolites. Interestingly we also found that in the mostly confined space of HZSM-5 straight channels, the favorability became nearly null suggesting that the hydrogen-substituted cyclopentenyls were forming in these regions of the pores. We concluded that the formation of alkylcyclopentenyls in medium pore zeolites may not be thermodynamically controlled and rather under kinetic control.

5.1.3 Extent of kinetic control of the isomerization of alkyl-substituted cyclopentenyl cations in H-ZSM-5 and H-ZSM-22

We performed periodic density functional theory (DFT) calculations to study the isomerization of alkyl-substituted cyclopentenyl cations in medium pore acid zeolites, H-ZSM-5 and H-ZSM-22. We considered the isomerization of a 4-ethyl-4,5,5-trimethylcyclopentenyl cation (**A**), a product of cyclization of protonated acyclic trienes which has been shown leads to product distributions that are controlled by the pore structure, contrary to DFT-predicted thermodynamics. This contribution focused on the post-cyclization isomerization to determine the impact of confinement on the formation of the thermodynamically favored isomers. We used the Rule Input Network Generator code to obtain the isomerization reaction network from **A** to **T** and **K**-type isomers, which differ in the ring allylic substitution pattern. The reaction network is made up of 15 multi-step pathways, consisting of alkyl and hydride shifts, leading to five distinct isomers; three **T**-type and two **K**-type, where **K**-type isomers are intermediates and **T**-type isomers are products where the reaction can terminate. We used a combined finite temperature and zero-Kelvin protocol to compute elementary step barriers; finite temperature metadynamics was used to obtain endpoints which were used as initial input for Climbing Image-Nudged Elastic Band (CINEB) calculations for the computation of reaction and transition state energies. We found the barriers for elementary isomerization reactions are mostly controlled by the breaking and forming of resonance and do not differ significantly in the two zeolites. We built a microkinetic model to study the equilibrium product distribution for isomerization. Rate constants were computed from free energy data and incorporated into a system of 24 rate equations corresponding to the 24 isomers in the reaction network. We found that at equilibrium ($t > 10^4$ sec) the major

products corresponded to the more thermodynamically stable isomers (**T**-type), but differed in the two zeolites, namely **T2** in H-ZSM-5 and **T3** in H-ZSM-22. In addition, we found that in the more confined pore of H-ZSM-22, the **K2** isomer formed in higher concentrations as compared to H-ZSM-5. We also found that only after very long times ($>10^7$ seconds) did the product distribution in H-ZSM-22 fall under thermodynamic control. These findings suggest that for alkylcyclopentenyl isomerizations, different levels of confinement in medium pores can lead to different product distributions and kinetic control can occur at earlier stages of the reaction.

5.2 Suggestions for Future Work

In Chapter 1 we discussed the difference between zero-Kelvin and finite temperature sampling techniques in computational chemistry and its applications in zeolite science. In the earlier years of this work, we investigated how the implementation of finite temperature techniques may provide new insights on an already established mechanism. Specifically, we considered the keto/enol tautomerization reaction in HZSM-5, a well-studied elementary step in biofuel synthesis processes. We found that in the finite temperature regime, the reaction occurs through a different mechanism. Figure 5.1 shows that the mechanism obtained from our finite temperature sampling (bottom) goes through a stable intermediate whereas the previously determined mechanism (top) is concerted and occurs via a single transition state. We believe that a similar analysis can be applied to systems described in the chapters above, namely acyclic cyclization.

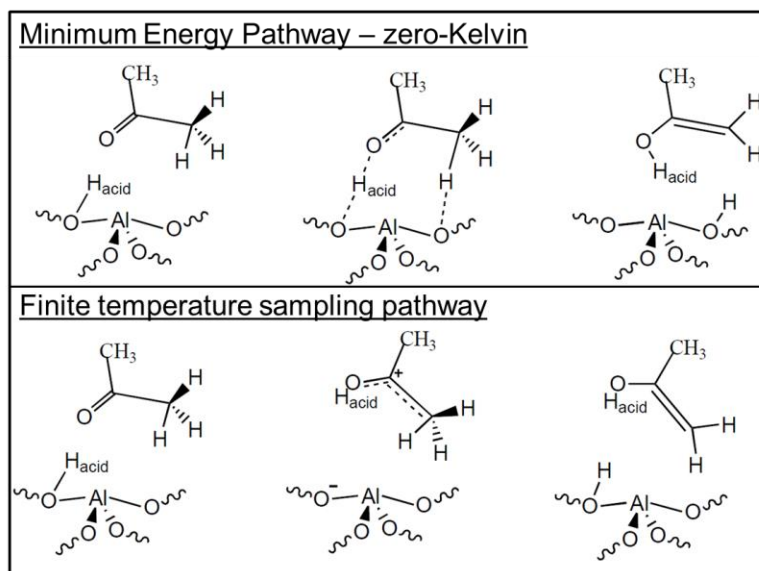


Figure 5.1 Comparison of keto/enol tautomerization reaction mechanisms over acidic zeolite active site. The top shows the mechanism obtained using a zero-Kelvin approach which yields a concerted process. In the bottom panel the mechanism from finite temperature sampling is shown which is a stepwise process and includes an intermediate.

The previous chapter of this dissertation (Ch. 4) discussed the results from studying the isomerization of alkylcyclopentenyl cations in medium pore zeolites. We hypothesized that the initial reactant for the isomerization would form from an acyclic protonated octatriene precursor, utilized in the works showcased in Chapters 2 and 3. The question still remains however; *What is the mechanism by which cyclization occurs?* We believe that the next step in understanding the formation of alkylcyclopentenyl cations from acyclic precursors requires answering this question. Figure 5.2 shows a hypothesized reaction that would precede the cyclization, and subsequent isomerization, studied in this dissertation. Namely, we propose that the acyclic precursor, a protonated octatriene in this case, would have to undergo conformational changes through rotations of the center dihedral bonds (shown in red in Figure 5.2) and form a cis/cis configuration before ultimately forming the ring and undergoing isomerization. In fact, in earlier years we conducted preliminary calculations that showed the cyclic molecule can form from

this cis/cis precursor. Investigating this step in the mechanism of forming alkylcyclopentenyl cations in zeolites would provide a more complete picture of the formation of cyclic species from acyclic precursors.

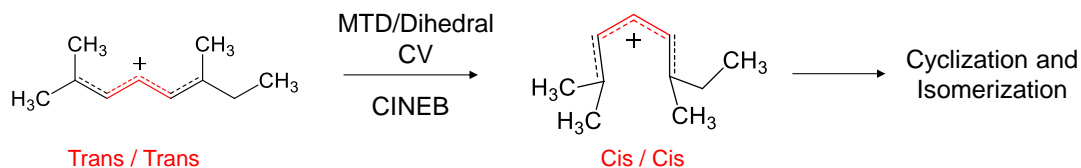


Figure 5.2 Proposed reaction of dihedral configurational changes preceding cyclization and isomerization. The octatriene molecule on the left is in a trans/trans form and converts to a cis/cis form through rotation of the center dihedral angles shown in red. This process is studied using Climbing Image Nudged Elastic Band (CINEB) and Metadynamics (MTD) via a dihedral collective variable (CV).

The way by which to study the reaction mentioned above provides an opportunity for an extension of the work shown in Figure 5.1; comparison of zero-Kelvin and finite temperature pathways. The configurational mechanism shown in Figure 5.2 involves the rotation of two C-C dihedral bonds transforming the molecule from a trans/trans configuration to a cis/cis configuration. The mechanism, and underlying free energy landscape, for this reaction can be studied using both zero-Kelvin and finite temperature techniques followed by a comparison of the results. Climbing Image Nudged Elastic Band (CINEB) would be used as the zero Kelvin approach and metadynamics would be used for finite temperature sampling. Specifically, the metadynamics scheme can be implemented such that the dihedral angles highlighted in red in Figure 5.2 would be incorporated as the reaction coordinates, or collective variables. Ultimately, implementation of both approaches would provide mechanisms and free energy landscapes for the reaction which would serve two purposes: (1) complete the alkylcyclopentenyl cation formation from acyclic precursor mechanism, and (2) allow for direct comparison of zero-Kelvin and finite temperature pathways.

In Chapter 4, we highlighted the presence of kinetic control during the isomerization of cyclopentenyl cations in H-ZSM-22. We considered alkyl and hydride shifts for the interconversion between different isomers of alkyl-substituted cyclopentenyl cations. Although these elementary reactions were enough to give rise to the 15-pathway reaction network, we left the possibility of concerted conversions without much consideration. With that, we believe that the continuation of the isomerization work would involve considering how the inclusion of concerted conversions between isomers might impact the extent of kinetic control. Specifically, one can consider the case of the conversion from T2 to T3, which as discussed can occur through two different multi-step pathways. In theory this conversion can also occur through a single concerted process as shown in Figure 5.3. We propose that one could use CINEB to compute the barrier associated with this conversion and include it in the microkinetic model. This would extend the breadth of the isomerization reaction and also allow one to determine if the inclusion of this transformation has an impact on the formation of the isomers in H- ZSM-22, and more importantly, the extent of kinetic control. Furthermore, one could also use metadynamics via a coordination number collective variable, similar to what was used in Chapter 4, to study the reaction in the finite temperature regime. This would provide another reaction for the comparison of zero-Kelvin and finite temperature results as discussed above.

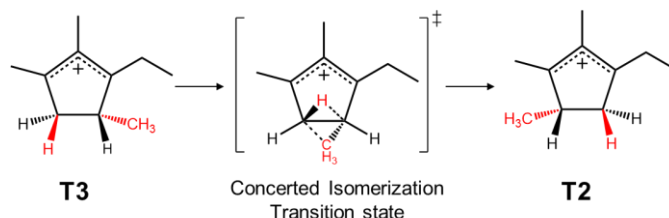


Figure 5.3 Concerted conversion between **T3** and **T2** cyclopentenyl cation isomers. The hypothesized transition state is shown and has a simultaneous transfer of hydrogen and methyl group, highlighted in red.

A final suggestion for future work involves the application of the microkinetic model scheme outlined in Chapter 4 to investigate the formation of coke species from alkylcyclopentenyl cation precursors (Figure 5.4). In Chapter 3 we investigated the formation of hydrogen and methyl C-2 substituted alkylcyclopentenyl cations in large and medium pore zeolites and found that the pore structure exhibits shape-selectivity. Then, in Chapter 4 we constructed a microkinetic model to better understand the thermodynamics and kinetics of the reaction. The next question in this context is: *How do the mechanisms by which coke molecules form from alkylcyclopentenyl cations differ based on initial allylic substitution patterns?* The protocol outlined in Chapter 4; using a network generator to determine reaction pathways, then building a microkinetic model based on computed reaction and transition state free energies, can be applied to answer the question above. Starting at the two reactants shown in Figure 5.4 on the left, one can use the network generator to extract pathways by which alkylcyclopentenyl cations form coke molecules, for instance through ring contraction and expansion reactions. Then, the reaction and transition state free energies can be computed using CINEB and incorporated into a microkinetic model which can predict concentrations of coke molecules at equilibrium. The results from this study, along with those mentioned above, have the capability to provide a more complete picture of how acyclic precursors, forming in the initial stages of zeolite catalysis, ultimately transform into coke molecules that form during later stages and deactivate the catalyst.

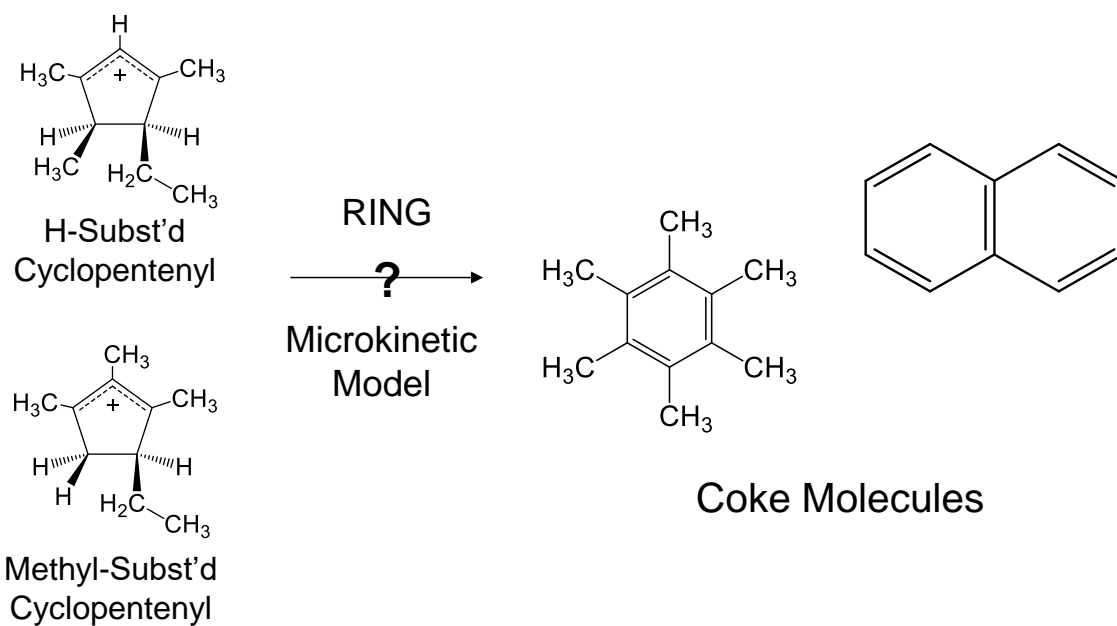


Figure 5.4 Formation of coke molecules from alkylcyclopentenyl cations. The reaction network is determined using the Rule Input Network Generator (RING) code and reaction and transition state energies are incorporated in a microkinetic model over zeolite catalysts. Differences may be attributed to the different initial alkylcyclopentenyl cation.

BIBLIOGRAPHY

- Adam, Waldemar et al. 2000. "UV-vis and IR Spectral Characterization of Persistent Carbenium Ions, Generated upon Incorporation of Cinnamyl Alcohols in the Acid Zeolites HZSM-5 and HMor." *The Journal of Organic Chemistry* 65(13): 3947–51. <https://doi.org/10.1021/jo991801r>.
- Agarwal, Vishal, George W Huber, W Curtis Conner, and Scott M Auerbach. 2011. "Simulating Infrared Spectra and Hydrogen Bonding in Cellulose I β at Elevated Temperatures." *The Journal of Chemical Physics* 135(13): 134506. <https://doi.org/10.1063/1.3646306>.
- Alberti, A, P Davoli, and G. Vezzalini. 1986. "The Crystal Structure Refinement of a Natural Mordenite." *Zeitschrift für Kristallographie* 175: 249–56.
- Alexopoulos, Konstantinos, Mal Soon Lee, et al. 2016. "Anharmonicity and Confinement in Zeolites: Structure, Spectroscopy, and Adsorption Free Energy of Ethanol in H-ZSM-5." *Journal of Physical Chemistry C* 120(13): 7172–82. <https://doi.org/10.1021/acs.jpcc.6b00923>.
- Alexopoulos, Konstantinos, Mathew John, et al. 2016. "DFT-Based Microkinetic Modeling of Ethanol Dehydration in H-ZSM-5." *Journal of Catalysis* 339: 173–85. <https://www.sciencedirect.com/science/article/pii/S0021951716300318>.
- Baerlocher, C., and L. B. McCusker. "International Zeolite Association: Database of Zeolite Structures."
- Baerlocher, Christian, and Lynne B. McCusker. "International Zeolite Association: Database of Zeolite Structures."
- Baerlocher, Christian, Lynne B. McCusker, and David H. Olson. 2007. *Atlas of Zeolite Framework Types*. Sixth Edit. Amsterdam: Elsevier Science B.V.
- Borodina, E et al. 2017. "Influence of the Reaction Temperature on the Nature of the Active and Deactivating Species During Methanol-to-Olefins Conversion over H-SAPO-34." *ACS Catalysis* 7(8): 5268–81. <https://doi.org/10.1021/acscatal.7b01497>.
- Brändle, Martin, and Joachim Sauer. 1998. "Acidity Differences between Inorganic Solids Induced by Their Framework Structure. A Combined Quantum Mechanics/Molecular Mechanics Ab Initio Study on Zeolites." *Journal of the American Chemical Society* 120(7): 1556–70. <https://doi.org/10.1021/ja9729037>.
- Buczek, Aneta, Teobald Kupka, Małgorzata A Broda, and Adriana Żyła. 2016. "Predicting the Structure and Vibrational Frequencies of Ethylene Using Harmonic and Anharmonic Approaches at the Kohn-Sham Complete Basis Set Limit." *Journal of molecular modeling* 22(1): 42. <https://www.ncbi.nlm.nih.gov/pubmed/26800989>.
- Cano, María L et al. 1995. "Characterization of Persistent α,ω -Diphenyl Substituted Allyl Cations within Monodirectional Acid Zeolites." *Journal of the Chemical Society, Chemical Communications* (24): 2477–78. <http://dx.doi.org/10.1039/C39950002477>.
- Chen, Zhiqiang et al. 2018. "Synthesis and Characterization of Bundle-Shaped ZSM-22 Zeolite via the Oriented Fusion of Nanorods and Its Enhanced Isomerization Performance." *Journal of Catalysis* 361: 177–85.
- Dahl, Ivar M, and Stein Kolboe. 1993. "On the Reaction Mechanism for Propene Formation in the MTO Reaction over SAPO-34." *Catalysis Letters* 20(3): 329–36. <https://doi.org/10.1007/BF00769305>.
- Daniel, Däumer, Rächle Konstantin, and Reschetilowski Wladimir. 2012. "Experimental and Computational Investigations of the Deactivation of H-ZSM-5 Zeolite by Coking in the Conversion of Ethanol into Hydrocarbons." *ChemCatChem* 4(6): 802–14. <https://doi.org/10.1002/cctc.201200015>.
- Dědeček, J., Z. Sobalík, and B. Wichterlová. 2012. "Siting and Distribution of Framework Aluminium Atoms in Silicon-Rich Zeolites and Impact on Catalysis." *Catalysis Reviews - Science and Engineering* 54(2): 135–223.
- Demuth, T, J Hafner, L Benco, and H Toulhoat. 2000. "Structural and Acidic Properties of Mordenite. An Ab Initio Density-Functional Study." *The Journal of Physical Chemistry B* 104(19): 4593–4607. <https://doi.org/10.1021/jp993843p>.
- Deno, N. C. et al. 1964. "Aliphatic Dienyl Cations." *Journal of the American Chemical Society* 86(9): 1871–72.
- Deno, N C, Herman G Richey, et al. 1963. "Carbonium Ions. XI. Nuclear Magnetic Resonance Spectra of the Aliphatic Alkenyl Cations." *Journal of the American Chemical Society* 85(19): 2991–95.
- Deno, N C, Norman Friedman, James D Hodge, and John J Houser. 1963. "Carbonium Ions. XII. The

- Direct Observation of Rearrangement and Hydrogen-Deuterium Exchange in Cycloalkenyl Cations.” *Journal of the American Chemical Society* 85(19): 2995–97.
- Derewinski, Mirosław, Priit Sarv, and Amparo Mifsud. 2006. “Thermal Stability and Siting of Aluminum in Isostructural ZSM-22 and Theta-1 Zeolites.” *Catalysis Today* 114(2–3): 197–204.
- Ensing, Bernd et al. 2006. “Metadynamics as a Tool for Exploring Free Energy Landscapes of Chemical Reactions.” *Accounts of Chemical Research* 39(2): 73–81. <http://dx.doi.org/10.1021/ar040198i>.
- Fang, Hanjun et al. 2011. “Theoretical Investigation of the Effects of the Zeolite Framework on the Stability of Carbenium Ions.” *The Journal of Physical Chemistry C* 115(15): 7429–39. <https://doi.org/10.1021/jp1097316>.
- Frisch, M J et al. 2009. “Gaussian 09, Revision B.01;”
- Goedecker, S, M Teter, and J Hutter. 1996. “Separable Dual-Space Gaussian Pseudopotentials.” *Physical Review B* 54(3): 1703–10. <https://link.aps.org/doi/10.1103/PhysRevB.54.1703>.
- Goetze, Joris, and Bert M Weckhuysen. 2018. “Spatiotemporal Coke Formation over Zeolite ZSM-5 during the Methanol-to-Olefins Process as Studied with Operando UV-Vis Spectroscopy: A Comparison between H-ZSM-5 and Mg-ZSM-5.” *Catalysis Science & Technology* 8(6): 1632–44. <http://dx.doi.org/10.1039/C7CY02459B>.
- Grimme, Stefan, Jens Antony, Stephan Ehrlich, and Helge Krieg. 2010. “A Consistent and Accurate Ab Initio Parametrization of Density Functional Dispersion Correction (DFT-D) for the 94 Elements H–Pu.” *The Journal of Chemical Physics* 132(15): 154104. <https://doi.org/10.1063/1.3382344>.
- Guo, Hai-yan et al. 2014. “Distribution of Al and Adsorption of NH₃ in Mordenite: A Computational Study.” *Journal of Fuel Chemistry and Technology* 42(5): 582–90. <http://www.sciencedirect.com/science/article/pii/S1872581314600281>.
- Haw, James F et al. 2000. “Roles for Cyclopentenyl Cations in the Synthesis of Hydrocarbons from Methanol on Zeolite Catalyst HZSM-5.” (20): 4763–75.
- Haw, James F, Weiguo Song, David M Marcus, and John B Nicholas. 2003. “The Mechanism of Methanol to Hydrocarbon Catalysis.” *Accounts of Chemical Research* 36(5): 317–26. <https://doi.org/10.1021/ar020006o>.
- Hemselsoet, Karen et al. 2011. “Experimental and Theoretical IR Study of Methanol and Ethanol Conversion over H-SAPO-34.” *Catalysis Today* 177(1): 12–24. <http://www.sciencedirect.com/science/article/pii/S0920586111004767>.
- Henkelman, Graeme, Blas P Uberuaga, and Hannes Jónsson. 2000. “A Climbing Image Nudged Elastic Band Method for Finding Saddle Points and Minimum Energy Paths.” *The Journal of Chemical Physics* 113(22): 9901–4. <https://doi.org/10.1063/1.1329672>.
- Hernandez, Eric D, and Friederike C Jentoft. 2020. “Spectroscopic Signatures Reveal Cyclopentenyl Cation Contributions in Methanol-to-Olefins Catalysis.” *ACS Catalysis* 10(10): 5764–82. <https://doi.org/10.1021/acscatal.0c00721>.
- Hernandez, Eric D, Babgen Manookian, Scott M Auerbach, and Friederike C Jentoft. 2021. “Shape-Selective Synthesis of Alkylcyclopentenyl Cations in Zeolites and Spectroscopic Distinction of Constitutional Isomers.” *ACS Catalysis* 11(21): 12893–914. <https://doi.org/10.1021/acscatal.1c03039>.
- Humphrey, William, Andrew Dalke, and Klaus Schulten. 1996. “VMD: Visual Molecular Dynamics.” *Journal of Molecular Graphics* 14(1): 33–38. <http://www.sciencedirect.com/science/article/pii/S0263785596000185>.
- Johnson III, Russell D., ed. 2019. NIST Standard Reference Database Number 101 *NIST Computational Chemistry Comparison and Benchmark Database*. Release 20. <http://cccbdb.nist.gov/>.
- Johnson, Russell D., ed. 2019. “NIST Computational Chemistry Comparison and Benchmark Database, NIST Standard Reference Database Number 101.”
- Joshi, Yogesh V, and Kendall T Thomson. 2005. “Embedded Cluster (QM/MM) Investigation of C₆ Diene Cyclization in HZSM-5.” *Journal of Catalysis* 230(2): 440–63. <http://www.sciencedirect.com/science/article/pii/S0021951704006050>.
- Lesthaeghe, David, Veronique Van Speybroeck, Guy B Marin, and Michel Waroquier. 2007. “The Rise and Fall of Direct Mechanisms in Methanol-to-Olefin Catalysis : An Overview of Theoretical Contributions.” : 8832–38.
- Lin-Vien, Daimay, Norman B Colthup, William G Fateley, and Jeanette G Grasselli. 1991. “The Handbook of Infrared and Raman Characteristic Frequencies of Organic Molecules: Chapter 2 - Alkanes.” In eds. Daimay Lin-Vien, Norman B Colthup, William G Fateley, and Jeanette G B T - *The Handbook of Infrared and Raman Characteristic Frequencies of Organic Molecules* Grasselli. San Diego:

- Academic Press, 9–28. <http://www.sciencedirect.com/science/article/pii/B9780080571164500080>.
- Liu, B et al. 2016. “Advances in the Study of Coke Formation over Zeolite Catalysts in the Methanol-to-Hydrocarbon Process.” *Applied Petrochemical Research*: 1–7. <http://dx.doi.org/10.1007/s13203-016-0156-z>.
- Manookian, Babgen et al. 2020. “Experimental and DFT Calculated IR Spectra of Guests in Zeolites: Acyclic Olefins and Host–Guest Interactions.” *The Journal of Physical Chemistry C* 124(19): 10561–72. <https://doi.org/10.1021/acs.jpcc.0c01225>.
- Mathias, Gerald, and Marcel D Baer. 2011. “Generalized Normal Coordinates for the Vibrational Analysis of Molecular Dynamics Simulations.” *Journal of Chemical Theory and Computation* 7(7): 2028–39. <https://doi.org/10.1021/ct2001304>.
- Meier, W. M. 1961. “The Crystal Structure of Mordenite (Ptilolite)*.” *Zeitschrift für Kristallographie* 115(5–6): 439–50. <https://www.degruyter.com/view/j/zkri.1961.115.issue-5-6/zkri.1961.115.5-6.439/zkri.1961.115.5-6.439.xml>.
- Migues, Angela N et al. 2018. “On the Rational Design of Zeolite Clusters for Converging Reaction Barriers: Quantum Study of Aldol Kinetics Confined in HZSM-5.” *The Journal of Physical Chemistry C* 122(40): 23230–41. <https://doi.org/10.1021/acs.jpcc.8b08684>.
- Migues, Angela N, S Vaitheeswaran, and Scott M Auerbach. 2014. “Density Functional Theory Study of Mixed Aldol Condensation Catalyzed by Acidic Zeolites HZSM-5 and HY.” *The Journal of Physical Chemistry C* 118(35): 20283–90. <https://doi.org/10.1021/jp504131y>.
- De Moor, Bart A., Marie-Françoise Reyniers, et al. 2011. “Adsorption of C2–C8 N-Alkanes in Zeolites.” *The Journal of Physical Chemistry C* 115(4): 1204–19.
- De Moor, Bart A, An Ghysels, et al. 2011. “Normal Mode Analysis in Zeolites: Toward an Efficient Calculation of Adsorption Entropies.” *Journal of Chemical Theory and Computation* 7(4): 1090–1101. <https://doi.org/10.1021/ct1005505>.
- Moses, Poul Georg, and Jens K Nørskov. 2013. “Methanol to Dimethyl Ether over ZSM-22: A Periodic Density Functional Theory Study.” *ACS Catalysis* 3(4): 735–45. <https://doi.org/10.1021/cs300722w>.
- Mosley, Jonathan D et al. 2014. “Structural Isomerization of the Gas-Phase 2-Norbornyl Cation Revealed with Infrared Spectroscopy and Computational Chemistry.” *Angewandte Chemie International Edition* 53(23): 5888–91. <https://doi.org/10.1002/anie.201311326>.
- Nguyen, Cuong M., Marie Françoise Reyniers, and Guy B. Marin. 2011. “Theoretical Study of the Adsorption of the Butanol Isomers in H-ZSM-5.” *Journal of Physical Chemistry C* 115(17): 8658–69.
- Nguyen, Cuong M, Marie-Françoise Reyniers, and Guy B Marin. 2015. “Adsorption Thermodynamics of C1–C4 Alcohols in H-FAU, H-MOR, H-ZSM-5, and H-ZSM-22.” *Journal of Catalysis* 322: 91–103. <https://www.sciencedirect.com/science/article/pii/S002195171400325X>.
- Olah, George A., Paul R. Clifford, Yuval Halpern, and Robert G. Johanson. 1971. “Stable Carbocations. CXIX. Carbon-13 Nuclear Magnetic Resonance Spectroscopy Study of the Structure of Allyl Cations.” *Journal of the American Chemical Society* 93(17): 4219–22.
- Olah, George A., C. U. Pittman, and Theodore S. Sorensen. 1966. “Pentadienyl Cations and Their Rearrangements in FSO₃H-SbF₅ Solution.” *Journal of the American Chemical Society* 88(10): 2331–32.
- Olah, George A., Charles U. Pittman, and Martyn C.R. Symons. 1968. “Electronic Spectra.” In *Carbonium Ions*, eds. George A. Olah and Paul von R. Schleyer. New York: Interscience Publishers, 153–222.
- Olsbye, U et al. 2015. “The Formation and Degradation of Active Species during Methanol Conversion over Protonated Zeotype Catalysts.” *Chemical Society Reviews* 44(20): 7155–76. <http://dx.doi.org/10.1039/C5CS00304K>.
- Osuga, Ryota, Toshiyuki Yokoi, and Junko N Kondo. 2019. “IR Observation of Activated Ether Species on Acidic OH Groups on H-ZSM-5 Zeolites.” *Molecular Catalysis* 477: 110535. <http://www.sciencedirect.com/science/article/pii/S2468823119303785>.
- Premadasa, Uvinduni I et al. 2018. “Solvent Isotopic Effects on a Surfactant Headgroup at the Air–Liquid Interface.” *The Journal of Physical Chemistry C* 122(28): 16079–85. <https://doi.org/10.1021/acs.jpcc.8b03680>.
- Rasmussen, D B et al. 2017. “Reaction Mechanism of Dimethyl Ether Carbonylation to Methyl Acetate over Mordenite – a Combined DFT/Experimental Study.” *Catalysis Science & Technology* 7(5): 1141–52. <http://dx.doi.org/10.1039/C6CY01904H>.
- Rauhut, Guntram, and Peter Pulay. 1995. “Transferable Scaling Factors for Density Functional Derived

- Vibrational Force Fields." *The Journal of Physical Chemistry* 99(10): 3093–3100. <https://doi.org/10.1021/j100010a019>.
- Reyniers, Marie-Françoise, and Guy B Marin. 2014. "Experimental and Theoretical Methods in Kinetic Studies of Heterogeneously Catalyzed Reactions." *Annual Review of Chemical and Biomolecular Engineering* 5(1): 563–94. <https://doi.org/10.1146/annurev-chembioeng-060713-040032>.
- Sklenak, Stepan et al. 2008. "Aluminum Siting in the ZSM-22 and Theta-1 Zeolites Revisited: A QM/MM Study." *Collection of Czechoslovak Chemical Communications* 73(6–7): 909–20.
- Sorensen, T S. 1964. "The Synthesis and Reactions of Divinyl Carbonium Ions." *Canadian Journal of Chemistry* 42(12): 2768–80. <https://doi.org/10.1139/v64-410>.
- Sorensen, Theodore S. 1964. "The Synthesis and Reactions of Divinyl Carbonium Ions." *Canadian Journal of Chemistry* 42(12): 2768–80.
- Sorensen, Theodore S. 1967. "Directly Observable Carbonium Ion-Carbonium Ion Rearrangements. I. Kinetics and Equilibria in the Interconversion of Trialkylcyclopentenyl Cations." *Journal of the American Chemical Society* 89(15): 3782–94. <https://doi.org/10.1021/ja00991a019>.
- Squillacote, Michael E, and Fengting Liang. 2005. "Conformational Thermodynamic and Kinetic Parameters of Methyl-Substituted 1,3-Butadienes." *The Journal of Organic Chemistry* 70(17): 6564–73. <https://doi.org/10.1021/jo0500277>.
- Sun, Yanjin, Chong-Wen Zhou, Kieran P Somers, and Henry J Curran. 2019. "Ab Initio/Transition-State Theory Study of the Reactions of C₅H₉ Species of Relevance to 1,3-Pentadiene, Part I: Potential Energy Surfaces, Thermochemistry, and High-Pressure Limiting Rate Constants." *The Journal of Physical Chemistry A* 123(42): 9019–52. <https://doi.org/10.1021/acs.jpca.9b06628>.
- Teketel, Shewangizaw, Stian Svelle, Karl-Petter Lillerud, and Unni Olsbye. 2009. "Shape-Selective Conversion of Methanol to Hydrocarbons Over 10-Ring Unidirectional-Channel Acidic H-ZSM-22." *ChemCatChem* 1(1): 78–81. <https://doi.org/10.1002/cctc.200900057>.
- Tyrode, Eric, Mark W Rutland, and Colin D Bain. 2008. "Adsorption of CTAB on Hydrophilic Silica Studied by Linear and Nonlinear Optical Spectroscopy." *Journal of the American Chemical Society* 130(51): 17434–45. <https://doi.org/10.1021/ja805169z>.
- Unni, Olsbye et al. 2012. "Conversion of Methanol to Hydrocarbons: How Zeolite Cavity and Pore Size Controls Product Selectivity." *Angewandte Chemie International Edition* 51(24): 5810–31. <https://doi.org/10.1002/anie.201103657>.
- VandeVondele, J et al. 2005. "QUICKSTEP: Fast and Accurate Density Functional Calculations Using a Mixed Gaussian and Plane Waves Approach." *Computer Physics Communications* 167(2): 103–28. <http://dx.doi.org/10.5167/uzh-3175>.
- Vandevondele, Joost et al. 2005. "Quickstep: Fast and Accurate Density Functional Calculations Using a Mixed Gaussian and Plane Waves Approach." *Computer Physics Communications* 167(2): 103–28.
- VandeVondele, Joost, and Jürg Hutter. 2007. "Gaussian Basis Sets for Accurate Calculations on Molecular Systems in Gas and Condensed Phases." *The Journal of Chemical Physics* 127(11): 114105. <https://doi.org/10.1063/1.2770708>.
- Wang, Sen et al. 2019. "Origin and Evolution of the Initial Hydrocarbon Pool Intermediates in the Transition Period for the Conversion of Methanol to Olefins over H-ZSM-5 Zeolite." *Journal of Catalysis* 369: 382–95. <http://www.sciencedirect.com/science/article/pii/S0021951718304597>.
- Wang, Tongkun et al. 2019. "Critical Role of Tricyclic Bridges Including Neighboring Rings for Understanding Raman Spectra of Zeolites." *Journal of the American Chemical Society* 141(51): 20318–24. <https://doi.org/10.1021/jacs.9b10346>.
- Wulfers, Matthew J, and Friederike C Jentoft. 2014. "The Role of Cyclopentadienium Ions in Methanol-to-Hydrocarbons Chemistry." *ACS Catalysis* 4(10): 3521–32. <http://dx.doi.org/10.1021/cs500722m>.
- Yarulina, Irina et al. 2018. "Recent Trends and Fundamental Insights in the Methanol-to-Hydrocarbons Process." *Nature Catalysis* 1(6): 398–411. <https://doi.org/10.1038/s41929-018-0078-5>.
- Zhang, Mozhi et al. 2016. "Methanol Conversion on ZSM-22, ZSM-35 and ZSM-5 Zeolites: Effects of 10-Membered Ring Zeolite Structures on Methylcyclopentenyl Cations and Dual Cycle Mechanism." *RSC Advances* 6(98): 95855–64. <http://dx.doi.org/10.1039/C6RA08884H>.
- Zhang, Wenna et al. 2018. "Methanol to Olefins Reaction over Cavity-Type Zeolite: Cavity Controls the Critical Intermediates and Product Selectivity." *ACS Catalysis* 8(12): 10950–63. <https://doi.org/10.1021/acscatal.8b02164>.